

THE DEFECT STRUCTURE AND PERFORMANCE OF METHYLAMMONIUM
LEAD TRIHALIDE THIN-FILM BASED PHOTOVOLTAICS

by

D. WESTLEY MILLER

A DISSERTATION

Presented to the Department of Physics
and the Graduate School of the University of Oregon
in partial fulfillment of the requirements
for the degree of
Doctor of Philosophy

June 2017

DISSERTATION APPROVAL PAGE

Student: D. Westley Miller

Title: The Defect Structure and Performance of Methylammonium Lead Trihalide Thin-film Based Photovoltaics

This dissertation has been accepted and approved in partial fulfillment of the requirements for the Doctor of Philosophy degree in the Department of Physics by:

Hailin Wang	Chair
Mark C. Lonergan	Advisor
Benjamín Alemán	Core Member
Eric Corwin	Core Member
Michael Kellman	Institutional Representative

and

Scott L. Pratt	Dean of the Graduate School
----------------	-----------------------------

Original approval signatures are on file with the University of Oregon Graduate School.

Degree awarded June 2017

© 2017 D. Westley Miller

DISSERTATION ABSTRACT

D. Westley Miller

Doctor of Philosophy

Department of Physics

June 2017

Title: The Defect Structure and Performance of Methylammonium Lead Trihalide Thin-film Based Photovoltaics

In order to limit global warming to 1.5-2° C deployed solar photovoltaic (PV) power must increase from today's 0.228 TW to 2–10 TW installed by 2030, depending on demand. These goals require increasing manufacturing capacity, which, in turn, requires lowering the cost of electricity produced by PV. However, high demand scenarios will require greater cost reductions in order to make PV generated electricity *as competitive* as it needs to be to enable this growth. It is unclear whether established PV technologies —silicon, CdTe, GaAs, or $\text{CuIn}_x\text{Ga}_{1-x}\text{Se}_2$ —can achieve the necessary breakthroughs in efficiency and price. A newer technology known as the ‘perovskite solar cell’ (PSC) has recently emerged as promising contender.

In the last seven years the efficiency of PSCs increased by the same amount covered by established technologies in the last thirty. However, PSCs suffer from chemical instability under operating conditions and hysteresis in current-voltage measurements used to characterize power output. Characterizing the defect structures formed by this material and how they interact with device performance and degradation may allow stabilization of PSCs. To that end, this work investigates defects in perovskite solar cells, the impact of these defects on performance, and the effect of alloying and degradation on the electronically active defect structure.

Chapter I gives a brief introduction, motivating research in solar cells generally and perovskites in particular as well as introducing some challenges the technology faces. Chapter II gives some background in semiconductors and the device physics of solar cells. Chapter III introduces the performance and defect characterization methods employed. Chapter IV discusses results of these measurements on methylammonium lead triiodide cells correlating defects with device performance. Chapter V applies the some of the same techniques to a series of $\text{CH}_3\text{NH}_3\text{Pb}(\text{I}_{1-x}\text{Br}_x)_3$ based perovskites aged for up to 2400 hours to explore the impact of alloying and aging on the defect structure. Chapter VI discusses implications for perovskite development and directions for future research.

This dissertation includes previously published co-authored material.

CURRICULUM VITAE

NAME OF AUTHOR: D. Westley Miller

GRADUATE AND UNDERGRADUATE SCHOOLS ATTENDED:

University of Oregon, Eugene
University of Louisville, Louisville

DEGREES AWARDED:

Doctor of Philosophy, Physics, 2017, University of Oregon
Bachelor of Science, Physics, 2008, University of Louisville

AREAS OF SPECIAL INTEREST:

Semiconductor Device Physics
Defect Characterization
Photovoltaics

PROFESSIONAL EXPERIENCE:

Graduate Research and Teaching Assistant, University of Oregon, 2009-2017
Research Fellow, National Renewable Energy Laboratory, Fall 2013 & Winter 2014

GRANTS, AWARDS AND HONORS:

Magna cum Laude, University of Louisville, 2008
MSI Special Entrance Award, University of Oregon, Materials Science Institute, 2009
Fulbright Research Grantee, Fulbright Commission and the Hungarian Academy of Sciences, 2008

PUBLICATIONS:

C.W. Warren, E.T. Roe, D.W. Miller, W.N. Shafarman, M.C. Lonergan, "An improved method for determining carrier densities via drive level capacitance profiling", *App.Phys.Lett.*, vol. 110, no. 20, p. 203901, 2017.

- C.M. Sutter-Fella¹, D.W. Miller¹, Quynh P. Ngo, Ellis T. Roe, Francesca M. Toma, Ian D. Sharp, Mark C. Lonergan, and Ali Javey, “Band Tailing and Deep Defect States in $\text{CH}_3\text{NH}_3\text{Pb}(\text{I}_{1-x}\text{Br}_x)_3$ Perovskites as Revealed by Sub-Bandgap Photocurrent”, *ACS Energy Lett.*, vol. 2, no. 3, pp. 709–715, 2017.
- D.W. Miller, G.E. Eperon, E.T. Roe, C.W. Warren, H.J. Snaith, M.C. Lonergan, “Defect states in Perovskite solar cells associated with hysteresis and performance”, *App.Phys.Lett.*, vol. 109, no. 15, p. 153902, 2016.
- H. Wang, C. Sutter-Fella, P. Lobacarro, M. Hettick, M. Zheng, D. Lien, D.W. Miller, C.W. Warren, E.T. Roe, M.C. Lonergan, H. Guthrey, N. Haegel, J. Ager, C. Carraro, R. Maboudian, J. He, A. Javey, “Increased Optoelectronic Quality and Uniformity of Hydrogenated p-InP Thin Films”, *Chemistry of Materials*, vol. 28, no. 13, pp. 4602–4607, 2016.
- C.W. Warren, J. Li, C.A. Wolden, D.M. Meysing, T.M. Barnes, D.W. Miller, J.T. Heath, “The effect of Copper on the sub-bandgap density of states in CdTe solar cells”, *App. Phys. Lett.*, vol. 106, no. 20, p. 203903, 2015.
- J.W. Boucher, D.W. Miller, C.W. Warren, J.D. Cohen, B.E. McCandless, J.T. Heath, M.C. Lonergan, S.W. Boettcher, “Optical response of deep defects as revealed by transient photocapacitance and photocurrent spectroscopy in CdTe/CdS solar cells,” *Sol. Energ. Mat. Sol. C.*, vol. 129, pp. 57–63, 2014.
- C.W. Warren, D.W. Miller, F. Yasin, and J.T. Heath, “Characterization of bulk defect response in $\text{Cu}(\text{In}, \text{Ga})\text{Se}_2$ thin-film solar cell using DLTS,” *Proceedings of the 39th IEEE Photovoltaic Specialists Conference*, pp. 0170–0173, 2013.
- D.W. Miller, Peter Hugger, Jet Meitzner, Charles W Warren, A Rockett, Steve Kevan, J David Cohen, “A contactless photoconductance technique for the identification of impact ionization,” *Proceedings of the 39th IEEE Photovoltaic Specialists Conference*, pp. 0195–0197, Jun. 2013.
- D.W. Miller, C.W. Warren, O. Gunawan, T. Gokmen, D.B. Mitzi, J.D. Cohen, “Electronically active defects in the $\text{Cu}_2\text{ZnSn}(\text{Se}, \text{S})_4$ alloys as revealed by transient photocapacitance spectroscopy”, *Appl.Phys.Lett.*, vol. 101, p. 142106, 2012.
- A.A. Rockett, D.W. Miller, J.D. Cohen “Analysis of $\text{Cu}(\text{In}, \text{Ga})\text{Se}_2$ solar cells using admittance spectroscopy under light bias,” *Proceedings of the 38th IEEE Photovoltaic Specialists Conference*, pp. 001727–001731, 2012.

¹These authors contributed equally.

D.W. Miller, G. Williger, C. Grady “Reconstructing the Mass-loss History of Parsamian 21,” *Bulletin of the American Astronomical Society*, vol. 40, p. 529, 2008.

Á. Kóspál, P. Ábrahám, D. Apai, D.R. Ardila, C.A. Grady, Th. Henning, A. Juhász, D.W. Miller, A Moór “High-resolution polarimetry of Parsamian 21: revealing the structure of an edge-on FU Ori disc,” *Monthly Notices of the Royal Astronomical Society*, vol. 383, pp. 1015–1028, 2008.

ACKNOWLEDGEMENTS

My time in graduate school at the University of Oregon is among the happiest and most fulfilling chapters of my life. I owe this to my colleagues, my friends, my mentors, and the City of Eugene. Eugene is my home. Accordingly, I have some thanks for the people who made my time here what it was.

I thank my mother for encouraging my interest in science, mathematics and technology from an early age and my father for encouraging a sense of adventure that initially drew me toward the west coast from our old Kentucky home. I thank my wife, Laura Barton, for lighting up my life in Eugene and being an excellent companion throughout graduate school.

I thank DuPont Manual Magnet High School, the University of Louisville, the Fulbright Scholar Program, the Hungarian Academy of Sciences, the University of Oregon and the teachers, professors and researchers of those institutions for the education and research opportunities they offered me; I would never have made it this far without them. I thank the students of those institutions and the denizens of Kentucky, Oregon, Hungary, and the United States of America for their contributions to my education and our research.

I thank my late advisor, J. David Cohen, for introducing me to research on solar cell materials as an undergraduate and inviting me back for graduate school. I will never forget his devotion to his students and his field of study. He changed the course of my life and helped me to find purpose. I thank Jian V. Li for his crucial support immediately following Dr. Cohen's death and for guiding my research at the National Renewable Energy Laboratory. I thank my peers and mentors over the years: Charles W. Warren, Peter Hugger, Peter Erslev, Adam Halverson, Jason Boucher, Ellis Roe,

Giles Eperon, and Carolin Sutter-Fella. They taught me, guided me, and enabled our work.

Most of all, I thank my advisor, Dr. Mark Lonergan. I could not have made it through graduate school without his good faith in my efforts, honest criticism, and guidance. Dr. Lonergan's earnest approach to scientific and academic integrity, his humility and curiosity, and his commitment to public service are a rare inspiration. It has been an honor to work with him.

This research was made possible by funding from the Office of Basic Energy Sciences of the U.S. Department of Energy through DE-SC0012363.

TABLE OF CONTENTS

Chapter	Page
I. INTRODUCTION AND BACKGROUND	1
Overview	1
Motivation	2
Emergence of Perovskite Solar Cells	5
II. BACKGROUND	10
Semiconductors	11
Photovoltaic Devices	22
III. DEFECT CHARACTERIZATION METHODS	31
Optical Absorption in Semiconductors	32
Comparing EQE, TPC, and TPI	41
IV. DEFECTS IN $\text{CH}_3\text{NH}_3\text{PbI}_3$ AND HYSTERESIS	43
Introduction	43
Sample Fabrication	45
Current-Voltage Hysteresis	48

Chapter	Page
Sub-Bandgap External Quantum Efficiency	50
Transient Photocapacitance Spectroscopy	53
Correlations with Device Performance	55
Summary	59
V. DEFECTS AND DISORDER IN $\text{CH}_3\text{NH}_3\text{Pb}(\text{I}_{1-x}\text{Br}_x)_3$	61
Introduction	61
Sample Fabrication	64
Effects of Bromine Alloying on Sub-Bandgap EQE	68
Evaluating Non-Radiative Recombination	78
Effects of Degradation	80
Summary	88
VI. CONCLUSION AND FUTURE DIRECTIONS	91
VII. APPENDICES	94
A. Rate-Dependent Current-Voltage Data	94
B. Band-Gap Determination from EQE and TPC	94
C. Fitting Defect Spectra	95
D. Minority Carrier Collection in $\text{CH}_3\text{NH}_3\text{PbI}_3$	96
REFERENCES CITED	114

LIST OF FIGURES

Figure	Page
1. Schematic of a Solar Cell	10
2. Diagram of Band-Filling in Various Types of Materials	13
3. Diagram of Point Defects and Associated States	16
4. Minority Carrier Lifetime vs $E_D - E_V$ for Various N_A	21
5. Minority Carrier Lifetime vs $E_D - E_V$ for Various E_g	22
6. Diagram of a $n^+;p$ Junction	23
7. $J-V$ and $P-V$ of an Ideal Solar Cell	24
8. Equivalent Circuit Model of an Ideal Solar Cell	25
9. Illustration of $J-V$ Hysteresis	29
10. Transitions Contributing to Sub-Bandgap Absorption	34
11. Urbach Energy vs x in $\text{Cu}_2\text{ZnSn}(\text{Se}_{1-x}\text{S}_x)_4$	36
12. Voltage Deficit Versus Urbach Energy in $\text{Cu}_2\text{ZnSn}(\text{Se}_{1-x}\text{S}_x)_4$	37
13. Transient Photocurrent Spectra of InP Based Solar Cells	39
14. V_{oc} vs 1.1 eV Defect Density in InP Solar Cells	40
15. Rate Dependent Current-Voltage Curve for Vapor 1	50
16. Sub-Bandgap EQE Spectra of $\text{CH}_3\text{NH}_3\text{PbI}_3$ PSCs	51
17. TPC Spectra for $\text{CH}_3\text{NH}_3\text{PbI}_3$ PSCs	54
18. Performance vs Defect EQE	56
19. SEM Image of Mixed-Halide Perovskite Solar Cell	66
20. Lattice Spacing vs x in $\text{CH}_3\text{NH}_3\text{Pb}(\text{I}_{1-x}\text{Br}_x)_3$	67
21. Sub-Bandgap EQE Spectra of $\text{CH}_3\text{NH}_3\text{Pb}(\text{I}_{1-x}\text{Br}_x)_3$ PSCs	70
22. Urbach Energies of $\text{CH}_3\text{NH}_3\text{Pb}(\text{I}_{1-x}\text{Br}_x)_3$ Thin Films	71

Figure	Page
23. Urbach Energy vs E_g for Technologically Utile Semiconductors	73
24. EQE of FTO/Spiro/Au Photoconductor	76
25. Internal PLQY of $\text{CH}_3\text{NH}_3\text{Pb}(\text{I}_{1-x}\text{Br}_x)_3$ Thin Films	79
26. XRD Pattern of $\text{CH}_3\text{NH}_3\text{Pb}(\text{I}_{0.6}\text{Br}_{0.4})_3$ Thin Film	81
27. Evolution of PbI_2 Precipitation and the Urbach Energy	83
28. Evolution of $\text{CH}_3\text{NH}_3\text{PbI}_3$ EQE with Air Exposure	84
29. Evolution of $\text{CH}_3\text{NH}_3\text{PbBr}_3$ EQE with Air Exposure	86
30. Evolution of $\text{CH}_3\text{NH}_3\text{Pb}(\text{I}_{0.1}\text{Br}_{0.9})_3$ EQE with Air Exposure	87
31. Evolution of $\text{CH}_3\text{NH}_3\text{Pb}(\text{I}_{0.6}\text{Br}_{0.4})_3$ EQE with Air Exposure	88
32. Photograph of Degraded $\text{CH}_3\text{NH}_3\text{Pb}(\text{I}_{0.6}\text{Br}_{0.4})_3$ Solar Cells	89
33. Rate Dependent Current-Voltage Curve for Vapor 2	94
34. Rate Dependent Current-Voltage Curve for Vapor 3	95
35. Rate Dependent Current-Voltage Curve for Dip 1	96
36. Rate Dependent Current-Voltage Curve for Dip 2	97
37. Tauc Plot for Dip 1 from EQE	98
38. Tauc Plot for Dip 2 from EQE	99
39. Tauc Plot for Vapor 1 from EQE	100
40. Tauc Plot for Vapor 2 from EQE	101
41. Tauc Plot for Vapor 3 from EQE	102
42. Tauc Plot for Dip 1 from TPC	103
43. Tauc Plot for Dip 2 from TPC	104
44. Tauc Plot for Vapor 1 from TPC	105
45. Tauc Plot for Vapor 2 from TPC	106
46. Fit to EQE Spectrum for Dip 1	107
47. Fit to EQE Spectrum for Dip 2	108

Figure	Page
48. Fit to EQE Spectrum for Vapor 1	109
49. Fit to EQE Spectrum for Vapor 2	110
50. Fit to EQE Spectrum for Vapor 3	111
51. TPC and TPI for Vapor 1	112
52. TPC and TPI for Dip 1	113

LIST OF TABLES

Table	Page
1. Performance Parameters at -2 mV/s	49
2. Defect Energies in $\text{CH}_3\text{NH}_3\text{Pb}(\text{I}_{1-x}\text{Br}_x)_3$	75

CHAPTER I

INTRODUCTION AND BACKGROUND

Overview

This work describes the characterization of the sub-bandgap density of states, including point defects in perovskite solar cells utilizing absorbers with the chemical composition $\text{CH}_3\text{NH}_3\text{Pb}(\text{I}_{1-x}\text{Br}_x)_3$. Similar measurements performed on InP, GaAs, $\text{CuIn}_{1-x}\text{Ga}_x\text{Se}_2$ and $\text{Cu}_2\text{ZnSn}(\text{Se}_{1-y}\text{S}_y)_4$ are included in order to place the perovskite material within a larger context. Wherever possible, the observed defects are correlated with photovoltaic device performance parameters. The first chapter motivates research on defects in perovskite cells and introduces current voltage hysteresis and some hypotheses about its origin. The second chapter gives a photovoltaic device physics background discussing the impact of defects on device performance. The third chapter describes the characterization methods used in this work with examples of results from studies on non-perovskite solar cells. The fourth chapter describes the results of these measurements on $\text{CH}_3\text{NH}_3\text{PbI}_3$ perovskite solar cells and introduces a correlation between defects and performance. Portions of Chapter IV were taken from D.W. Miller, G.E. Eperon, E.T. Roe, C.W. Warren, H.J. Snaith, M.C. Lonergan, “Defect states in Perovskite solar cells associated with hysteresis and performance”, *App.Phys.Lett.*, vol. 109, pp. 153902, Oct. 2016. It was written entirely by me with editorial assistance of my co-authors. I collected the data with some assistance from E.T. Roe. The samples were fabricated by G.E. Eperon.

Chapter V considers a series of $\text{CH}_3\text{NH}_3\text{Pb}(\text{I}_{1-x}\text{Br}_x)_3$ based solar cells. It examines the variation in defect formation across the full range of mixed-halide compositions as well as the evolution of defect structure with exposure of the cells to moderate humidity. Portions of this chapter were taken from C.M. Sutter-Fella, D.W. Miller, Quynh P. Ngo, Ellis T. Roe, Francesca M. Toma, Ian D. Sharp, Mark C. Lonergan, and Ali Javey “Band Tailing and Deep Defect States in $\text{CH}_3\text{NH}_3\text{Pb}(\text{I}_{1-x}\text{Br}_x)_3$ Perovskites as Revealed by Sub-Bandgap Photocurrent”, ACS Energy Lett. submitted Dec. 2016. It was written with equal contributions by myself and C. M. Sutter Fella with editorial assistance of our co-authors. Data for this paper were collected by myself and with corroborating data using complementary techniques from C.M. Sutter-Fella. Data from D.W. Miller, C.W. Warren, O. Gunawan, T. Gokmen, D.B. Mitzi, J.D. Cohen, “Electronically active defects in the $\text{Cu}_2\text{ZnSn}(\text{Se,S})_4$ alloys as revealed by transient photocapacitance spectroscopy”, Appl.Phys.Lett., vol. 101, pp. 142106, Oct. 2012 are also included to place the results on $\text{CH}_3\text{NH}_3\text{Pb}(\text{I}_{1-x}\text{Br}_x)_3$ in a broader context. In this case, I collected data other than basic device performance metrics and wrote the paper with editorial assistance from my co-authors, particularly J.D. Cohen.

Chapter VI considers the results of Chapters IV and V together to draw conclusions regarding likely origins for the observed defects. Key among these conclusions are implications for defect origins. Paths for further research are outlined and preliminary data supporting those paths are considered.

Motivation

The global scientific community has achieved consensus that CO_2 emission from human activities are responsible for global climate change. The projected

problems associated with climate change are myriad, including ocean acidification, desertification, and rising sea levels[1]. While the consequences of inaction are dire, technological advances give us the option to slow, stall, and reverse growth in CO₂ emissions. To that end, carbon-free, renewable, energy sources have been deployed on a large scale. In particular, at least 228 GW of photovoltaic (PV) generation capacity were installed globally as of December 2015 [2]. The United States in the period from 2008 to 2015 demonstrated, for the first time, economic growth without associated growth in CO₂ emissions [3]. So, it is an established fact that we are capable as a society of slowing and stalling growth in CO₂ emissions without doing the same to the overall economy. While much of the credit for this shift in the United States is due to increased use of natural gas in lieu of coal for domestic energy production, some is due to wind and solar generation and achieving the necessary reductions in the CO₂ intensity of our energy production will require solar to play a bigger role. Market projections for PV predict 2–4 TW of capacity by 2030, though climate projections suggest that as much as 11 TW by 2030 will be required to limit global warming to 1.5–2 °C. While 2–4 TW of deployed PV capacity can be reached by 2030 using only extant PV production capacity, reaching higher deployment levels will require building additional PV manufacturing capability in addition to maintaining current facilities [4]. Ensuring that this can occur *in time* to mitigate the worst effects of climate change, therefore requires that PV profit margins grow or that the capital needed to build plants be greatly reduced. Thus, significant innovation in PV is still required to minimize the risks to the climate.

Photovoltaic devices can be divided into two major subgroups based on the type of material used to absorb the light: silicon and thin-films. Crystalline silicon (Si) based PV has historically dominated the terrestrial PV market and still represents

94% of deployed PV in the countries tracked by the International Energy Agency [2]. However, research cell efficiencies for single-crystal and multi-crystalline Si based solar cells of the type that currently dominate the market have hardly seen any efficiency improvements since the year 2000. This is not so surprising, record silicon solar cells are currently around 25–27 % while the theoretical limiting efficiency is about 29.8 % [5, 6]. The best commercially available module efficiencies are around 19–22 percent leaving room for improvement and decreased cost through increased efficiency [7, 8]. Costs have steadily decreased but line-of-sight improvements are not projected to allow the necessary increase in the rate of PV deployment [4].

Thin-film absorber based solar cells have long been considered a next-generation technology [2]. Because the active layer in a thin-film cell can absorb the same amount of light as a silicon absorber with one-hundredth or less the thickness, a variety of cost saving options in material processing and device fabrication become available to the manufacturer. Established thin-film semiconductors for photovoltaic devices include GaAs, CdTe, and $\text{CuIn}_{1-x}\text{Ga}_x\text{Se}_2$. GaAs makes the highest efficiency devices but requires high-purity single-crystalline films that are relatively free of defects which in turn requires expensive growth techniques [9]. As such, GaAs based cells have found use primarily in aerospace applications and in concentrating systems that require a clear sky so that the sun can be imaged on the cell. $\text{CuIn}_{1-x}\text{Ga}_x\text{Se}_2$ cells are the highest efficiency polycrystalline thin-film, single-junction, solar cells with 22.6 % power conversion efficiency [6]. $\text{CuIn}_{1-x}\text{Ga}_x\text{Se}_2$ has been commercialized for niche applications because it can be manufactured as a flexible thin-film on a steel substrate and as a utility scale power source with the largest single plant being the 82 MW Catalina, CA plant [10, 11]. CdTe has perhaps the greatest commercial success among thin-films with a record cell efficiency of 22.1 % [6], module efficiencies

of 17.0% and over 10 GW installed globally [12] including two 550 MW plants in California [13]. First Solar, the company producing the CdTe panels used in these power plants, also claims the world's lowest unsubsidized price for a solar photovoltaic power purchase agreement at 5.84 cents/kWh [14]. While $\text{CuIn}_{1-x}\text{Ga}_x\text{Se}_2$ and CdTe show great promise because they are already undercutting Si based cells and even fossil fuels in some locations, both may be unable to scale to the 4–11 TW scale by 2030 even if they do become much more profitable than they have been so far. This is because Indium and Tellurium are relatively rare elements in the Earth's crust that are mostly produced as a byproduct of copper mining. Discovery and development of higher quality tellurium and indium ores would change this assessment, but it would be unwise to depend on this kind of luck. For now, only the most optimistic scenarios allow for 1–2 TW of each to be deployed by 2030 with a cumulative production 7 TW possible by 2050 at the earliest[15]. Given the potential for resource limitations in $\text{CuIn}_{1-x}\text{Ga}_x\text{Se}_2$ and CdTe, the technological hurdles to cheaply processed GaAs solar cells, and the necessity for unforeseen cost reductions in Si-based solar cells it is clearly prudent to continue pursuing other options.

Emergence of Perovskite Solar Cells

Perovskite solar cells (PSCs) have emerged over the last eight years as a technology that could fulfill the promise of thin-film solar cells to be significantly cheaper than Si based cells without sacrificing efficiency. The perovskite semiconductors that serve as the absorber layer in these cells are named after the mineral CaTiO_3 with which they share a crystal structure. While the perovskites used in photovoltaics vary in their exact chemical composition, all have the general formula ABX_3 and those used in photovoltaic applications form a 3-dimensional perovskite

crystal structure which will be discussed in more detail in the next chapter. For photovoltaic applications the cations used at the A-site have been Cs^+ , CH_3NH_3^+ (methylammonium), and $\text{CH}(\text{NH}_2)_2^+$ (formamidinium); the cations at the B-site have been Sn^{2+} and Pb^{2+} ; and the anions at the X-site have been Cl^- , Br^- , and I^- . Excluding cesium, this group of elements and compounds is much cheaper, more plentiful, and therefore more suitable for large scale production than In or Te. As mentioned above, In and Te are produced primarily as by-products of other production. As such, they are likely to have very inelastic prices; i.e. increased demand due to solar applications will only drive up the cost of available material as opposed to funding a boost in production that would in turn decrease prices. The elements used in perovskite solar cells are often a primary product produced at rates 2-4 *orders of magnitude* higher than Te and In [16]. Cesium is the exception with very low production and it is unclear how much it could be scaled up. For now demand for Cs is very low and its use in PSCs does not appear to be essential for the perovskites that are optimized for conversion of the solar spectrum to electricity via a single junction solar cell.

Solar cells based on this material have seen their efficiencies rise from 3.8% in 2009 to a certified 22.1% today, tied with CdTe [6, 17]. This rate of improvement, 18.3% absolute in eight years, is unparalleled in the history of photovoltaic development. To cover that same ground, from 4% to 22% Si, $\text{CuIn}_{1-x}\text{Ga}_x\text{Se}_2$ and CdTe based solar cells each took at least 35 years [6, 18]. This incredibly quick rise is itself a phenomenon worth investigating as understanding what about perovskites allowed such quick progress will provide clues into whether it can be sustained beyond the current 22.1% or whether that efficiency level can be maintained as device areas are increased.

Certainly some of the progress was due to the low barrier for laboratories to begin working on perovskites. Perovskite solar cells are, in most cases, entirely solution processed with the exception of metal contacts evaporated onto the anode and cathode of the solar cell under vacuum. In addition to being solution processable, perovskite solar cells are processed at low temperatures. No processing steps over 120 °C are required. Given these requirements hundreds of laboratories worldwide are equipped to fabricate PSCs and the large number of groups working on them has no doubt aided progress. While the simple fact that there have been a lot of attempts explains some of the speed of progress, its still surprising that absolute efficiencies are already on par with much more mature technologies. Some have proposed that it is because this material simply does not favor the formation of deep defects that mediate recombination under most growth conditions. What types of defects perovskites form will be a central question in this work.

Low-temperature, solution-based processes also lend themselves to low-cost manufacturing using established techniques including: slot-die coating, inkjet printing, doctor blade (gravure) printing, and spin-coating. All but the last of these techniques are compatible with roll-to-roll processing and are already used industrially in the production of light emitting diodes and batteries. Roll-to-roll processing allows high-throughput manufacturing, lowering unit costs. So the same features that accelerated the progress of perovskite photovoltaics in the laboratory may allow them to be easily scaled up to commercial production. High-efficiency, low-temperature, solution-processed solar cells have been a long-standing goal for the reasons I just outlined. The achievement of these goals via perovskite solar cells emerged from a community of researchers that had long been pursuing this goal through what are known as dye-sensitized solar cells (DSSCs). DSSCs use a dye, that

is often organic, to absorb light but not to transport charge. Charge separation and transport is instead carried out by other materials one of which is often a porous or highly textured scaffold. This separates two roles that both occur in the absorber in the silicon or thin-film solar cells discussed above. The first reported perovskite solar cells were DSSCs with mesoporous TiO_2 anodes sensitized using either $\text{CH}_3\text{NH}_3\text{PbI}_3$ or $\text{CH}_3\text{NH}_3\text{PbBr}_3$ perovskites and with a liquid electrolyte mediating conduction to the cathode [17]. Regarding the stability of these cells, the authors stated ‘In studies of durability, continuous irradiation caused a photocurrent decay for an open cell exposed to air; this mechanism needs more study to improve the cell lifetime.’

From there, other groups were able to improve performance and stability first by using a different electrolyte [19] and later by replacing the electrolyte with a solid-state hole conductor [20, 21]. At this point the PSC was a solid-state dye-sensitized solar cell. While these cells were far more stable than their liquid-electrolyte based predecessors, the perovskites themselves were known to be sensitive to humidity and long term studies of material properties and device performance remain quite rare [22]. Experiments replacing the TiO_2 scaffold with a AlO_2 scaffold [21] or eliminating the hole transport layer and using a simple metal cathode [23] led to the realization that perovskites were good conductors of electrons and holes. In this way, the early evolution of perovskite solar cells can be seen as progressing from the use of perovskites as a new sensitizer in DSSCs to the realization that perovskites were high quality semiconductors capable of performing well in planar-heterojunction architecture like that used in other thin-film solar cells [22]. In comparisons between planar and meso-structured cells it emerged that the former showed pronounced hysteresis in the current-voltage sweeps used to measure power conversion efficiency [24]. To be clear, meso-structured cells did not lack current-voltage hysteresis entirely. Nonetheless,

it became clear that hysteresis was a phenomenon peculiar to PSCs that warranted study and complicated performance characterization [22].

To summarize, the emergence of perovskite solar cells has raised interesting questions regarding their defect structure, the origin of hysteresis in the material, and long-term stability of the solar cells based on a material that is sensitive to humidity. This dissertation attempts to address these questions by characterizing the performance and defect structure of a variety of perovskite solar cells both as fabricated and following long-term exposure to humid air.

CHAPTER II

BACKGROUND

A solar photovoltaic cell is any device which absorbs incident light and by dint of some asymmetry within that device generates a photovoltage and photocurrent. The first step in this process is absorption of an incident photon, resulting in the promotion of an electron from a lower energy state to a higher energy state. The material in which this takes place is referred to as an ‘absorber’. A schematic of a generic solar cell depicting this process is shown in Figure 1.

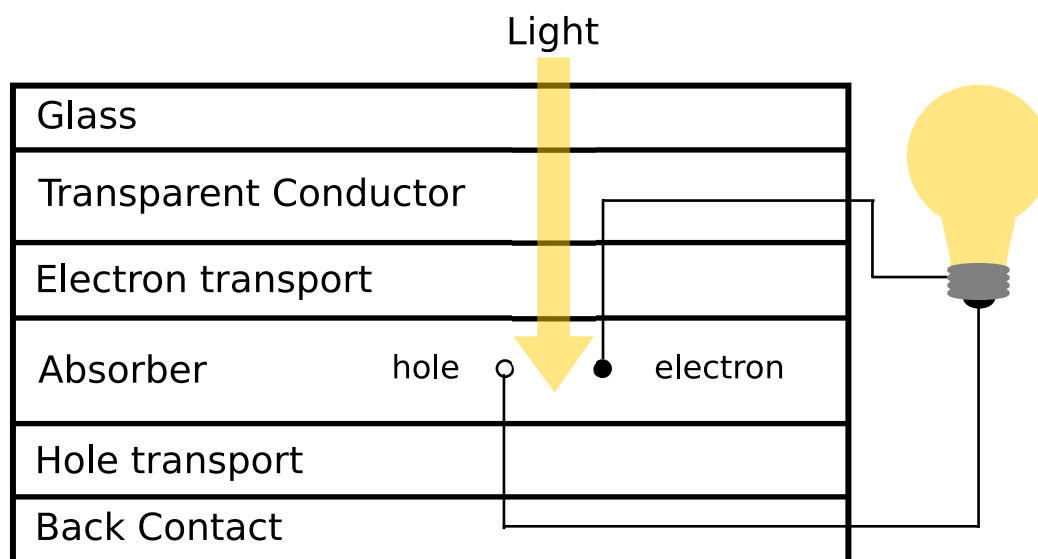


FIGURE 1. A schematic of a solar cell containing layers labeled by their function. These are the layers present in the Perovskite solar cells examined in this work.

Following the absorption, due to a built-in asymmetry in the electric potential through the absorber layer and/or due to asymmetry in the ability of electrons and holes to cross into the adjacent materials, the electron and hole are separated and exit the absorber in opposite directions. Note that this gives them the same sign of current due to their opposite charge. As drawn, in Figure 1, light enters through the glass and

passes through a transparent conductor and the electron transport material before being absorbed. Following absorption, the resulting electron-hole pair are separated by either a built-in electric field and/or a photovoltage that is present because of the inability for electrons to enter the hole transport material and vice-versa for holes. Any electrons that re-combine with holes before exiting to the external circuit to do work lower the efficiency of the device. Generally speaking, such a process is called recombination.

For most solar cells, and all those studied in this work, the absorber is a semiconductor that serves both to absorb the light and to transport the electron and hole away from each other and into other layers in the device. In this case, low rates of recombination within a material are important to its suitability for use as an absorber. Before entering into a discussion of recombination in absorbers and at interfaces with them, I will back up a bit to define a semiconductor and consider those things that contribute to the recombination of carriers in a semiconductor.

Semiconductors

A semiconductor can be described, phenomenologically, as follows: a material with a conductivity that increases with temperature (unlike a metal) and is much greater than that of an insulator but less than that of a metal at room temperature. This description can be improved by considering the physics behind the defining phenomena. An electron moving through a crystal will do so as a plane wave whose period, or wavelength, reflects the periodicity of that the atoms in the crystalline solid in question. Certain periods of the plane wave are not allowed due to destructive interference following scattering from the periodic array of atoms in the solid. Because the energy and wavelength of the plane wave are related, there are bands of allowed

electron energy, and bands in which there are no allowed states for an electron. The spacing and crystal structure of the atoms in the crystal will thus determine the allowed states of an electron in that crystal. Those allowed states, as a function of energy and wave vector, are collectively referred to as the band structure of the material. The band gap energy is the difference between the highest energy point in the valence bands and the lowest in the conduction bands, regardless of the wave-vector. If the valence band maximum (VBM) and conduction band minimum (CBM) occur at the same wave vector then the band gap is said to be *direct*. Otherwise, it is *indirect*. The Pauli exclusion principle dictates that two electrons (one of each spin) will be allowed in each available state. The electrons present will then fill the available energy states from the lowest energy on up. The available states are thus filled according to the Fermi-Dirac distribution

$$F(E) = \frac{1}{1 + \exp [(E - E_F)/k_B T]}, \quad (2.1)$$

where k_B is the Boltzmann constant, T is the temperature, E is the electron energy and E_F is the Fermi energy. E_F is the energy at which a hypothetical state has a 50 % chance of being occupied. States below the Fermi level are generally occupied and those above it are unoccupied. Note that at $T = 0$ equation 2.1 reduces to a step function that is 1 for $E < E_F$ and 0 for $E > E_F$. As temperature increases the chance of occupied states just below E_F decreases in proportion with an increase in the chance of occupied states just above. Considering the density of states at the VBM and CBM in relation to E_F allows a physical rather than phenomenological description of insulators, metals and semiconductors. Figure 2 shows some hypothetical densities of states near the VBM and CBM with different relationships to a single Fermi energy.

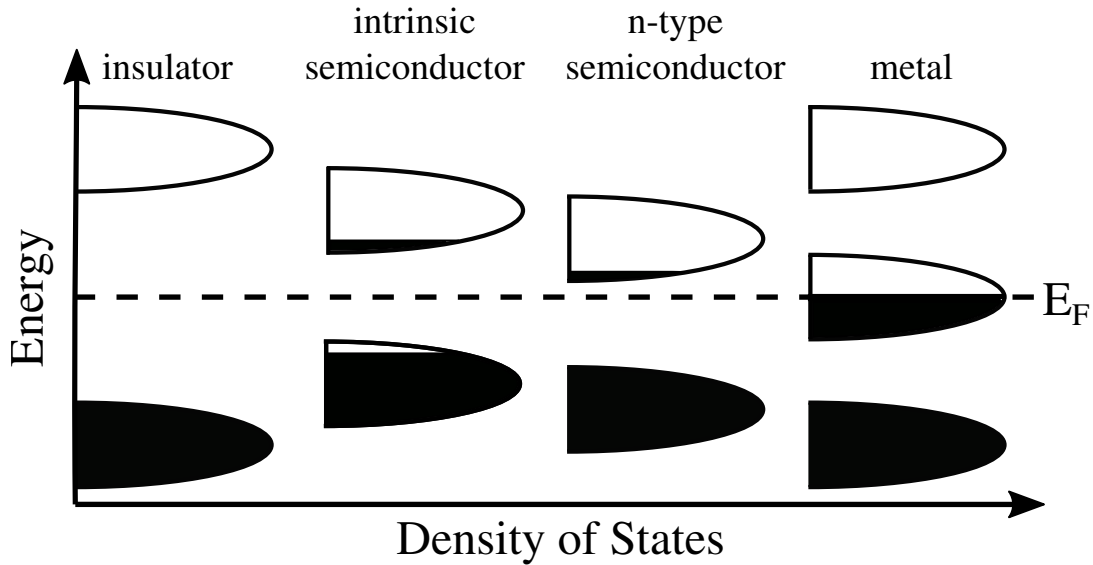


FIGURE 2. This diagram depicts band filling for various materials with different band structures. For each material the horizontal axis corresponds to the density of states in that band while while black shading indicates those states are occupied. The Fermi level E_F is the energy at which a hypothetical state has a 50 % chance of being occupied.

For insulators E_F falls between two bands which are far enough apart that the chance of some electrons occupying the higher energy band and leaving a state in the lower energy band unoccupied, is vanishingly small at room temperature. In a scenario such as this, the band below E_F is the aforementioned valence band, referring to the fact that these bands are in some sense made of the valence states of the solid's constituent atoms. The band above E_F is the aforementioned conduction band. The difference between the highest energy state in the valence band, E_v , and the lowest energy state in the conduction band, E_c , is defined as the band gap energy, denoted E_g . As a rule of thumb, intrinsic semiconductors with $E_g > 3$ eV will be insulators at room temperature. For a semiconductor, E_F again falls in a band gap, but it is a smaller band gap. In this case, a significant number of electrons are thermally promoted to the conduction band leaving behind a significant number of

holes in the valence band. As the temperature increases the density of electrons in the conduction band increases (along with holes in the valence band) and consequently conductivity increases. For a metal, on the other hand, E_F resides within a band so the concentration of electrons and holes in that band is very high and does not increase with temperature.

In addition to thermal excitation, it is possible to promote an electron from the valence to the conduction band. Consider a photon with energy E_γ . If $E_\gamma < E_g$ the photon cannot excite an electron from the valence band to the conduction band and will typically pass right through the semiconductor. If, on the other hand, $E_\gamma \geq E_g$, it may promote an electron from the valence band to the conduction band and is absorbed. This is the absorption process that was described earlier as the first step in the production of power from a solar cell. Up to E_g of the photon energy is now stored as the energy of the electron in the conduction band. Energy in excess of E_g is quickly lost to thermalization as the electron excited to $E_v + E_\gamma$ may take many small steps emitting heat in the form of vibrations in the crystal lattice known as phonons to lose this excess energy. This process takes place in femtoseconds. However, once it reaches the conduction band minimum, a single high energy phonon would need to be emitted in order for the electron to return to the valence band. This is due to the lack of intermediary states. Because such phonons are rare, this is a much slower process and for high quality semiconductors it is more likely that it will re-emit a photon. The average lifetime of the electron is an important metric for semiconductor quality. In the highest quality silicon, lifetimes can approach 1 ms at room temperature. So long as that electron does not recombine before reaching the external circuit, that stored E_g worth of energy may be used to do work.

So far we have given a very brief overview of insulators, metals and intrinsic semiconductors and introduced some ways in which conductivity in an intrinsic semiconductor or insulator may be temporarily increased. We left one material type depicted in Figure 2 out of the discussion, the n-type, as opposed to the intrinsic semiconductor. For a pure, intrinsic semiconductor such as totally pure, well-ordered, silicon, E_F lies very close to the middle of the gap. But, it is possible to create some states within the band gap by introducing impurities. If the resulting states are near the conduction band edge, then E_F will move closer to E_c and these states can easily donate their electrons to the conduction band resulting in high electron density and thus n-type conductivity. As defects in perovskite solar cells are central to this dissertation, we should spend a little time examining what constitutes a defect and what effect it can be expected to have on the band structure.

Defects and Dopants

The distinction between defects and dopants has more to do with our intentions than with the nature of the thing itself. Both are imperfections in the perfect order of the crystal. It is fair to say that all dopants are defects, but not all defects are dopants. Defects can be divided into native and impurity defects. Native defects are those that involve only the atoms meant to be in the crystal, but which are out of place. In an elemental semiconductor, such as crystalline silicon, the only intrinsic point defects are vacancies, denoted V_{Si} and interstitials denoted Si_i . In the notation just used, the main script indicates the element or vacancy associated with the defect and the subscript indicates its location on the ideal lattice of the material in which it is found. It is also possible to have extended defects such as stacking

faults, or boundaries between two grains. Lastly, there are impurity defects such as phosphorous-on-silicon, P_{Si} .

P_{Si} happens to be a dopant in Si. Because it has one extra electron, this electron is not needed to form a bond with its neighbors in the silicon lattice and is only weakly bound to the positive charge associated with the phosphorous atom. Because it is weakly bound the neutral P_{Si}^0 defect can be ionized to form $P_{Si}^+ + e^-$. It has now donated an electron to the conduction band and is said to be a donor. If the impurity atom in question instead had one too few electrons, then it would tend to borrow an extra electron from the valence band, leaving a hole. This is an acceptor.

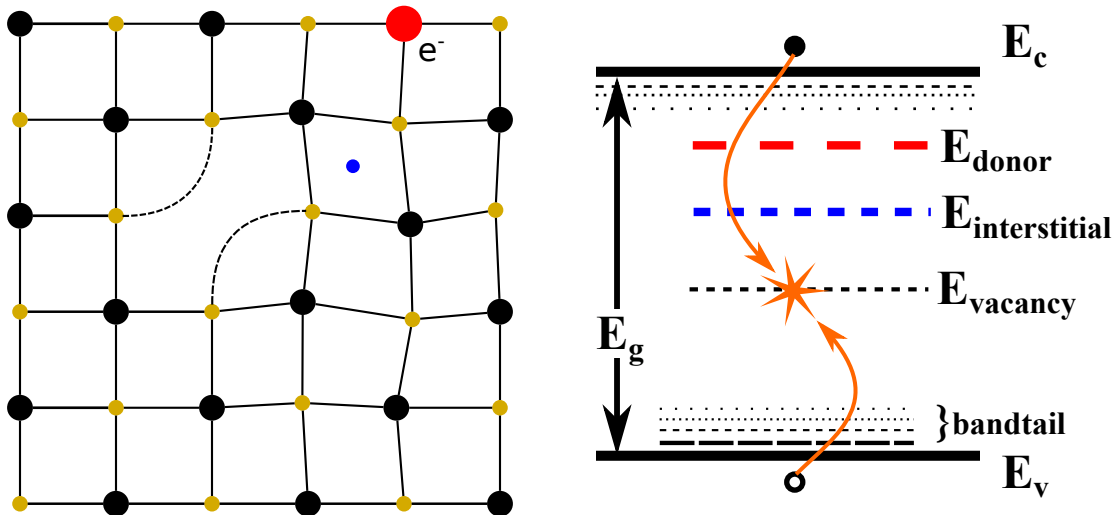


FIGURE 3. On the left side: a diagram of point defects in a 2-d crystal including a vacancy, an impurity dopant, an interstitial impurity, and strained bonds. On the right side: Some associated energy levels in the band gap and a depiction of defect mediated recombination.

If we consider a compound semiconductor, such as GaAs, the number of possible defects expands. In addition to increasing the number of possible locations where a vacancy or interstitial defect may be found, anti-site defects such as Ga_{As} are now possible. It should now be apparent that in the progression from an elemental group

IV semiconductor such as silicon, to a compound III-V semiconductor like GaAs, and on to a I-III-VI₂ or I₂-II-IV-VI₄ compound, the number of possible native defects increases combinatorially. I will not attempt to enumerate them. One last thing to consider are defect complexes. The density of defects is determined by the enthalpy of formation for the defect given the growth conditions of the crystal. Sometimes, it is energetically favored for a pair of defects to form together, as neighbors. One such example, predicted by density functional theory in an attempt to explain light-and biased induced metastabilities, is the V_{Se}-V_{Cu} di-vacancy complex in CuInSe₂ [25]. For the above reasons, it is less surprising that one can find extensive catalogs of the energy levels associated with various impurities in silicon, while some more complex semiconductors like Cu₂ZnSnSe₂ have so far resisted efforts to make extremely well-ordered crystals needed to systematically study impurity defects. This type of control is important because defects in their various forms are used to dope semiconductors or add deeper defects on purpose in order to engineer device properties such as extending the response range for a photodiode or modify band alignment with a neighboring material in the device.

Ultimately, whether a particular defect functions as a donor depends on: its allowed charge states; the energy of the state associated with that defect, E_D ; the temperature; and E_F as follows:

$$n_D^+ = n_D^0 \left\{ 1 - \left[1 + \exp\left(\frac{E_D - E_F}{k_B T}\right) \right]^{-1} \right\}. \quad (2.2)$$

Where n_D^+ and n_D^0 are the density of positively charged (ionized) and neutral donor defects, respectively. E_D is the energy of the donor-like defect. Likewise, the charge state of acceptor-like defects with energy E_A is set by:

$$n_A^- = n_A^0 \left[1 + \exp \left(\frac{E_A - E_F}{k_B T} \right) \right]^{-1}. \quad (2.3)$$

Defects can also serve as recombination centers, and whether they will do so efficiently depends on their energetic location in the bandgap. Defect mediated recombination in semiconductors was first described by W. Shockley, W. Read, and R. Hall in 1952 [26, 27]. Following the discussion of Shockley-Read-Hall recombination via defects presented in Chapter 3 of *The Physics of Solar Cells* by Peter Würfel, we will now present a couple examples of how defect behavior depends on the transition energy and the properties of the material in which it resides [28].

The rate at which a particular defect captures electrons is given by:

$$R_{e, d} = \sigma_e \nu_e n_e n_{h, d}. \quad (2.4)$$

Where σ_e is the capture cross-section for electrons of the unoccupied defect, ν_e is the thermal velocity of electrons in the conduction band, n_e is the density of electrons in the conduction band, and $n_{h, d}$ is the density of defects occupied by holes (unoccupied by electrons). Similarly the rate at which the defect captures holes is given by:

$$R_{h, d} = \sigma_h \nu_h n_h n_{e, d}. \quad (2.5)$$

The thermal velocity of holes is given by $\nu_h = (3k_B T / 2m_h^*)^{1/2}$, and for electrons $\nu_e = (3k_B T / 2m_e^*)^{1/2}$. Where m_h^* and m_e^* are the hole and electron effective masses.

If all the defects are occupied by electrons then we will maximize the rate of hole capture. Likewise, the electron capture is maximized if all the defects are unoccupied. These endpoints imply minimal lifetimes for holes and electrons respectively defined as $\tau_{h,\min} = (n_d\sigma_h\nu_h)^{-1}$ and $\tau_{e,\min} = (n_d\sigma_e\nu_e)^{-1}$ where n_d is the total defect density regardless of occupation. The actual lifetimes of the two carriers will be greater than these values, and competition between the two processes must be considered such that $n_{h,d} = n_d - n_{e,d}$. It is beyond the scope of this text to derive in detail how defect mediated recombination impacts actual carrier lifetimes in a semiconductor. But, it is easy enough to do so using the principle of detailed balance if one makes a number of reasonable assumptions including: $n_d \ll \Delta n_e, \Delta n_h$ and $\Delta n \ll n_e^0 + n_h^0$. Where Δn is the total density of photoexcited carriers, n_e is the density of electrons, and n_e^0 and n_h^0 are the densities of electrons and holes in the dark. These conditions amount to weak injection —i.e. most carriers are not photo-generated—and a relatively low impurity level relative to the generation rate. Such derivations can be found elsewhere [28]. The result is that we can express the minority lifetime, τ , as a function of the many variables introduced above.

$$\tau = \frac{1}{n_e^0 + n_h^0} \left\{ \tau_{h,\min} \left[n_e^0 + N_C \exp \left(-\frac{(E_C - E_D)}{k_B T} \right) \right] + \tau_{e,\min} \left[n_h^0 + N_V \exp \left(-\frac{(E_D - E_V)}{k_B T} \right) \right] \right\} \quad (2.6)$$

If we use a p-doped material with a shallow acceptor that is completely ionized at room temperature then $n_h^0 \simeq N_A$. Using the ‘*law of mass action*,’

$$n_e n_h = n_i^2 \quad (2.7)$$

where n_i is the ‘intrinsic density’ given by:

$$n_i^2 = N_C N_V \exp\left(-\frac{E_g}{k_B T}\right), \quad (2.8)$$

then $n_e^0 = n_i^2/N_A$. Making this substitution and referencing all energies with respect to $E_V \equiv 0$, Equation 2.6 becomes

$$\tau = \frac{1}{\frac{n_i^2}{N_A} + N_A} \left\{ \tau_{h,min} \left[\frac{n_i^2}{N_A} + N_C \exp\left(-\frac{(E_g - E_D)}{k_B T}\right) \right] + \tau_{e,min} \left[N_A + N_V \exp\left(-\frac{(E_D)}{k_B T}\right) \right] \right\}. \quad (2.9)$$

Using Equation 2.9 we can plot the minority carrier lifetime as a function of $E_V - E_D$ for a series of different values of N_A spanning the range of doping densities seen in solar cell absorbers. This plot is shown in Figure 4 for a material with parameters typical of the perovskite $\text{CH}_3\text{NH}_3\text{PbI}_3$. $E_g = 1.58$, $N_V = 2.5 \times 10^{18} \text{ cm}^{-3}$, $N_C = 7 \times 10^{18} \text{ cm}^{-3}$, $m_e^* = 0.17m_0$, and $m_h^* = 0.09m_0$ where m_0 is the electron mass. These values are based on experiments and density functional theory [29]. A defect with a cross-section for hole and electron capture $\sigma_h = \sigma_e = 1 \times 10^{15} \text{ cm}^{-2}$ and density of $N_D = 1 \times 10^{14} \text{ cm}^{-3}$ was used.

While Figure 4 shows generally good lifetimes with a minimum value comparable to that observed in very pure single crystals of $\text{CH}_3\text{NH}_3\text{PbI}_3$ [30], lower lifetimes would be expected in films with lots of unpassivated grain boundaries, or higher densities of bulk defects within each crystallite. It is apparent that higher doping limits lifetimes but this effect is compensated by the fact that high doping guards against losses in the open circuit voltage, V_{oc} due to recombination [28]. The most notable part of this result is that defects near mid-gap are much more effective recombination centers

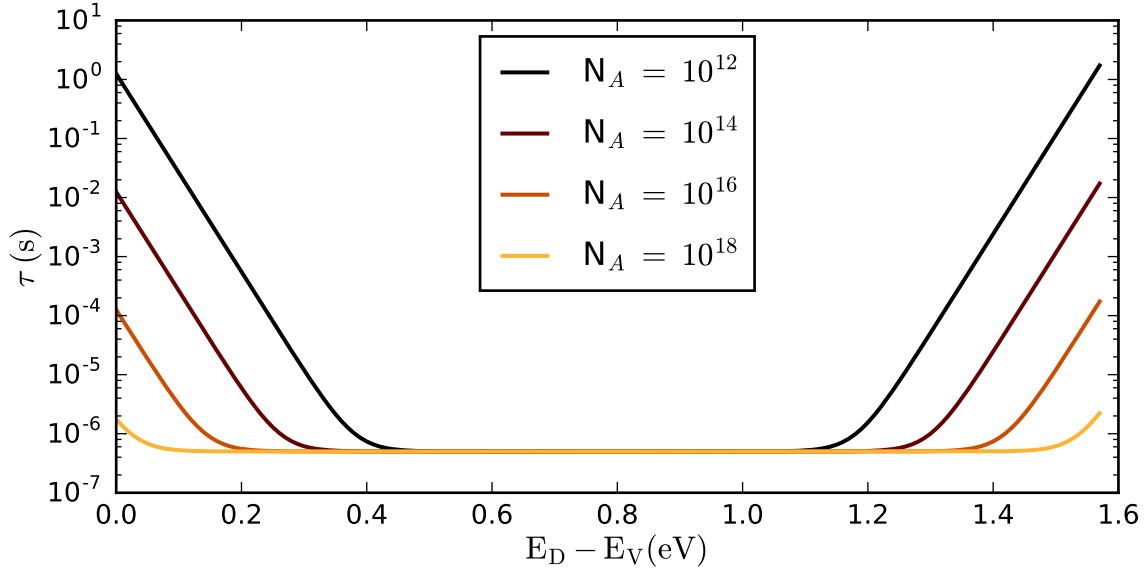


FIGURE 4. Minority carrier lifetime vs $E_D - E_V$ for various N_A using material properties expected of $\text{CH}_3\text{NH}_3\text{PbI}_3$. The minimal lifetime observed here is quite good for a direct-bandgap material and in rough agreement with lifetimes seen in high quality single crystals of $\text{CH}_3\text{NH}_3\text{PbI}_3$ [30]. Minimal lifetimes up to three order of magnitude lower might be expected for much more defective multi-crystalline films.

than those at the band-edges. Put another way, good dopants are bad recombination centers and vice-versa. But what happens with a wider band-gap material? In Figure 5 the same parameters as in Figure 4 are used, with $N_A = 1 \times 10^{12} \text{ cm}^{-3}$ for a series of band gaps spanning the range accessible to $\text{CH}_3\text{NH}_3\text{Pb}(\text{I}_{1-x}\text{Br}_x)_3$.

Figure 4 demonstrates that, all else being equal, defects near the middle of the gap are particularly deleterious to carrier lifetimes. Meanwhile, Figure 5 demonstrates that the region that is *near enough* to mid-gap to have the worst possible effects on lifetime expands with the band gap. Recalling that the minimal lifetimes for each carrier are set by $\tau_{h,\min} = (n_d \sigma_h \nu_h)^{-1}$ and $\tau_{e,\min} = (n_d \sigma_e \nu_e)^{-1}$ it becomes apparent that the density of defects near mid-gap must be minimized to maximize lifetime. Since defects near the band edges may provide a desired effect in the form of doping, while those closer to the middle may have unwanted consequences like enhanced

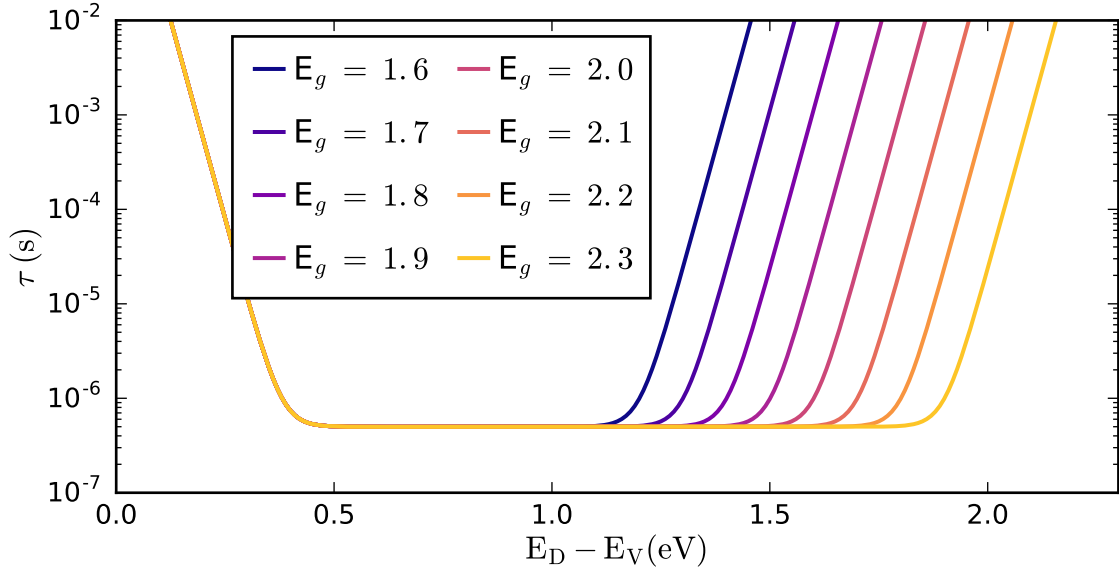


FIGURE 5. Minority carrier lifetime vs $E_D - E_V$ for various E_g . The region that is near-enough to mid-gap to allow this defect with a density of $N_D = 1 \times 10^{14} \text{ cm}^{-3}$ to cause the lifetime to reach its minimal lifetime expands with the band gap.

recombination, the development of methods to characterize the energy and density defects is crucial to progress and good device design. We will discuss the methods used in this study in Chapter III.

Photovoltaic Devices

By mating a lightly doped p-type semiconductor with a suitable band gap for absorbing the solar spectrum ($\sim 1.15\text{--}1.55 \text{ eV}$ being the optimal range for a single-junction solar cell) to another, more heavily doped n-type semiconductor with an appropriate band gap and electron affinity, one may form an n^+p junction that supplies the essential asymmetry needed to separate photocarriers produced in the absorber. The band structure for such a device in an open-circuit is shown in Figure 6.

A n^+p or p^+n junction with an ohmic back contact will function as a solar cell when exposed to light, but it is not the only architecture of solar cell. One could also

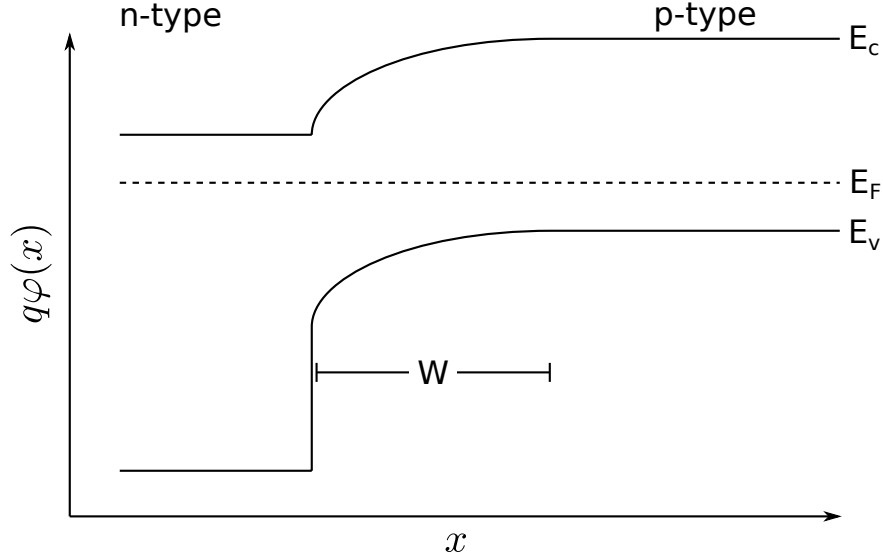


FIGURE 6. Diagram of a n^+p junction. W is the width of the *depletion region*, which is free of carriers due to the gradient in the potential, φ

have n:p structure in which the doping levels on either side of the interface are closer to equal; or a n-i-p structure, with a barrier to electrons at the back contact rather than an ohmic contact. Both of these structures are diodes that would pass current easily when a voltage is applied that flattens the bands but a voltage applied in the other direction only increases the barrier height and does not allow a large current to pass. In the dark, devices such as these will obey the ideal diode equation:

$$J_{\text{dark}}(V) = J_s \left(\exp \left[\frac{qV}{k_B T} \right] - 1 \right), \quad (2.10)$$

Where $J_{\text{dark}}(V)$, is the current density passed by the diode in the dark as a function of the applied voltage V ; J_s is the reverse saturation current density; and q is the

fundamental charge. An ideal solar cell exposed to light obeys this same equation but with the addition of a current source, J_L :

$$J_{\text{light}}(V) = J_s \left(\exp \left[\frac{qV}{k_B T} \right] - 1 \right) - J_L, \quad (2.11)$$

Where J_L is the current density produced in the solar cell under light exposure. Equations 2.10 and 2.11 are plotted in Figure 7 for a solar cell with $J_s = 1 \times 10^{-6}$ mA/cm² and $J_L = 25$ mA/cm². The circuit model implied by treating a solar cell in this way is shown in Figure 8.

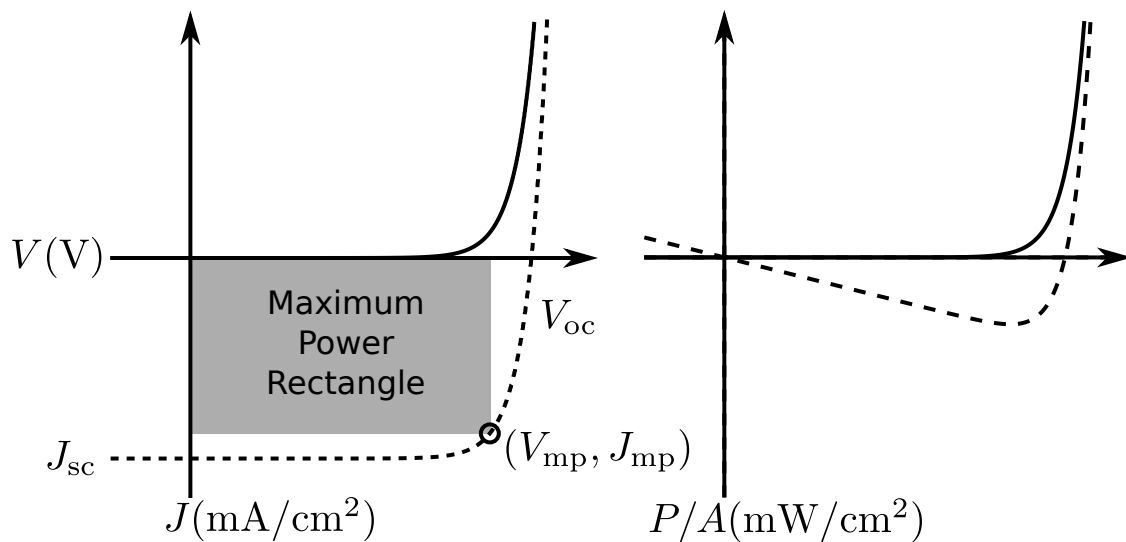


FIGURE 7. J - V (left) and P - V (right) of an ideal solar cell. Solid lines indicate the performance in the dark, dashed lines in the light.

Characterizing Performance

From Figure 7, we can identify a number of important parameters used to characterize the performance of solar cells. These are: V_{oc} ; the short-circuit current density J_{sc} ; and the current density and voltage at the maximum power point J_{mp}

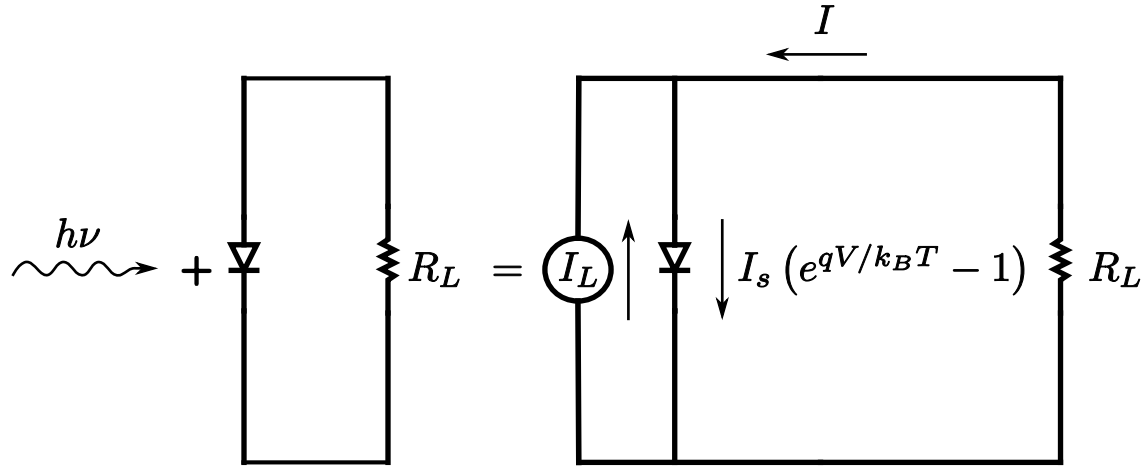


FIGURE 8. Equivalent circuit model of an ideal solar cell. In the dark, the solar cell is simply a diode, but with the addition of light The direction of the photocurrent and saturation current, I_L and I_s , are depicted next to their sources.

and V_{mp} . In Figure 7, we plot both the current density J and the power density $P/A = JV$. The maximum power point is easiest to identify on the P/A (V) plot. Because the photocurrent is defined to be negative—opposite the current produced by applying a voltage that flattens the bands—the maximum power output of the solar cell occurs at the absolute minimum of the P/A curve. The quadrant of the J - V plot with negative current density and positive voltage is thus referred to as the ‘power quadrant’.

It is interesting to note that in the quadrant defined by positive current and positive voltage the solar cell is operating as a light-emitting diode (LED), while in the quadrant defined by negative voltage and negative current it is operating as a photodiode. Efficient solar cells generally make efficient LEDs and photodiodes, neither of which must be particularly efficient for all applications; solar cells on the other hand must be efficient and yet, they need to cost much much less than both

LEDs and photodiodes, per unit area. This comparison provides stark relief to the challenge of producing a cost-effective solar cell. Returning to the task at hand, we ought to define efficiency. The maximum power density output can be identified on the J - V curve by drawing the maximum area rectangle circumscribed by the axes and the J - V curve within the power quadrant. This rectangle allows us to define the ‘fill-factor,’

$$FF \equiv \frac{J_{\text{mp}}V_{\text{mp}}}{J_{\text{sc}}V_{\text{oc}}}. \quad (2.12)$$

Which in turn facilitates defining the efficiency,

$$\eta \equiv \frac{P_{\text{out}}}{P_{\text{in}}} = \frac{J_{\text{mp}}V_{\text{mp}}A}{P_{\text{in}}} = \frac{J_{\text{sc}}V_{\text{oc}}FF \cdot A}{P_{\text{in}}}, \quad (2.13)$$

the primary figure of merit for a solar cell.

The efficiency for a solar cell as defined above generally depends on the total irradiance above the absorber’s band gap and the temperature. For that reason, when the efficiency of a cell or module is quoted that value refers to the value of η under standard measurement conditions: 25 °C and 100 mW/cm², also known as ‘1-sun’ irradiance. That 100 mW/cm² of irradiance is a total irradiance, as opposed to spectral, and should have a well-defined spectral distribution. This should generally match the terrestrial solar spectrum after passing through 1.5 air masses (equivalent to a solar zenith angle of 48°) on a clear day. The details of what is accepted as a proxy for this spectrum are defined and updated by various agencies such as the American Society for Testing and Materials or the International Electrotechnical Commission. While laboratories that certify record efficiencies meet exacting standards, the typical

academic laboratory simply uses a commercial ‘solar simulator’ that is intended to give a reasonably close match, at least above the band-gap of most solar cells.

It is difficult to reproduce the solar spectrum in a laboratory. In doing so, one will typically end up with a good approximation for the spectral shape but have a total irradiance that depends strongly on the distance to the source. This is not at all like the light from the sun itself near the Earth’s surface, which is virtually constant for practical heights. Beyond that, the exact spectral shape and total power will vary with the age of the lamp used to reproduce the spectrum. So, it is necessary to calibrate the distance to the source using a reference cell with a calibrated J_{sc} under ‘1-sun’, AM 1.5 irradiance that is traceable to a national laboratory or other such institution. Because solar simulators are far from perfect in their spectral imitation of the sun, the band-gap of this reference cell should be as close as possible to the device under test. This way, *at least* the total irradiance above the band-gap of the device under test will be about right. Typical standard cells are made with silicon, having a band-gap of 1.11 eV, though in some cases a short-wavelength-pass filter might be used in conjunction with it to achieve a better standard for a higher band-gap cell. However, the device under test, particularly for investigations of thin-films in material systems with tunable band-gaps may not be a particularly good match for the reference cell. For these reasons, along with the fact that many labs do not mention active temperature monitoring or control, absolute measurements of η are likely to have significant systematic errors. While this summarizes the challenges faced by the experimentalist wishing to characterize the efficiency of well established inorganic thin-film solar cells and newer ones with particularly wide band gaps, perovskite solar cells require extra care due to their instability and due to hysteresis in the current-

voltage sweeps commonly used to characterize the efficiency and other performance parameters of a solar cell.

Current-Voltage Hysteresis

Characterization of basic performance parameters in perovskite solar cells is complicated by hysteresis in J - V sweeps. The observed phenomena depend on the ramp-rate, direction, and sample history before beginning the sweep. At very high ramp rates (typically in excess of 10000 mV/s), the ‘pre-bias’ voltage that the sample equilibrates at before beginning the sweep determines the performance of the cell during the sweep, and cyclic curves will lie nearly on top of each other. If this voltage is in excess of the *steady-state* open-circuit voltage it can enhance the apparent performance; if it is below it, or in reverse bias it degrades the apparent performance. At more moderate ramp rates —10–1000 mV/s—the sample state seems to change over the course of the scan with the effective pre-bias being that of the previous voltages within that scan, leading to a separation of forward and reverse cycles in a cyclic J - V sweep. Finally, at very low ramp rates, the sample is able to equilibrate at each voltage for which the current is recorded leading results that are independent of ramp-direction. These phenomena are illustrated in Figure 9.

These effects may have corrupted many lab-reported efficiencies, particularly before the hysteresis itself became a topic of interest around 2013 [22]. However, efficiencies independently certified as world-record holders throughout the evolution of perovskite solar cells are steady-state values, unaffected by hysteresis. Beyond experimental difficulties hysteresis must be understood, first because failing to do so could prevent commercialization of perovskite solar cells and secondly because this interesting and somewhat novel phenomenon may provide insights into the nature of

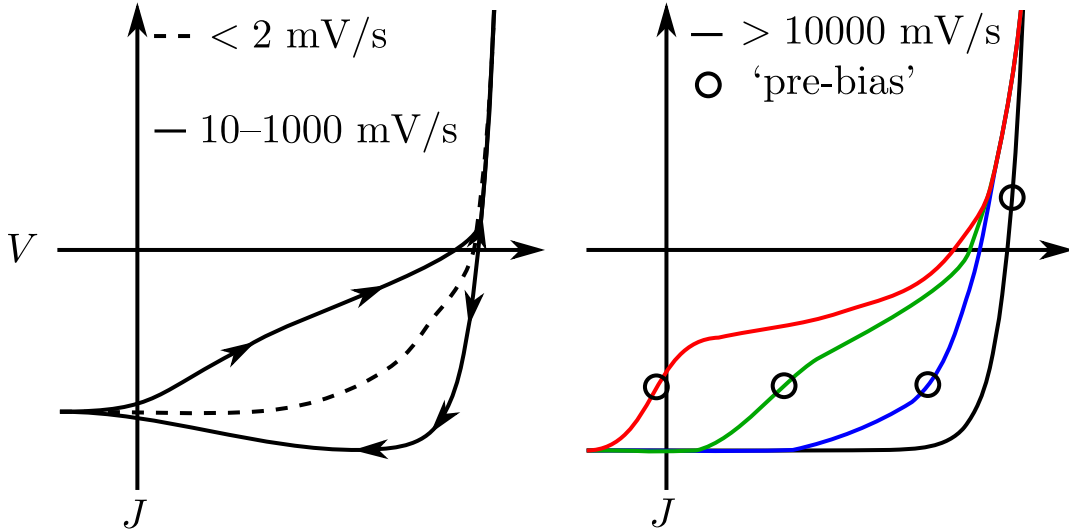


FIGURE 9. Illustration of hysteresis effects in J - V of Perovskite solar cells. Note, these are *not* real results, *nor* simulations! They are merely illustrations that are qualitatively consistent with observed phenomena. The left pane shows quasi-steady state and moderate ramp rate effects for continuous, cyclic sweeps. The right pane shows cyclic sweeps at very high ramp rates following equilibration at various ‘pre-bias’ voltages.

perovskite materials allowing improved performance of photovoltaic devices or as yet unanticipated applications.

A number of theories have been posited to explain hysteresis in perovskite solar cells. These include: trapping of electronic carriers at interface defect [31, 32]; various effects associated with mobile ions in the lattice [33–35]; and, ferroelectric effects [36] including those due to the dipole moment of large organic cations [37]. The presence of hysteresis in completely inorganic CsPbI_3 —whose symmetric cation and space group do not allow for ferroelectricity—demonstrates that ferroelectricity is not sufficient to explain hysteresis in PSCs [38]. However, further experimentation is needed to determine whether and to what extent the prior two theories describe the observed phenomena. The first two theories implicate some form of defect. The first implies defects as a recombination centers or as a modifiable space charge at the interface.

The second implies mobile ions in the form of either interstitial ions or vacancies that can move through the perovskite lattice temporarily screening or enhancing the built-in voltage of the solar cell. Therefore, studies of defects in PSCs should prove enlightening.

CHAPTER III

DEFECT CHARACTERIZATION METHODS

Portions of this chapter were taken from D.W. Miller, C.W. Warren, O. Gunawan, T. Gokmen, D.B. Mitzi, J.D. Cohen, “Electronically active defects in the $\text{Cu}_2\text{ZnSn}(\text{Se,S})_4$ alloys as revealed by transient photocapacitance spectroscopy”, *Appl.Phys.Lett.*, vol. 101, pp. 142106, Oct. 2012

I collected all the data used in this paper aside from basic performance characteristics and wrote it with editorial and analytical assistance from my co-authors, primarily J.D. Cohen.

This chapter also contains Transient Photocapacitance and Photocurrent Spectra from:

Hsin-Ping Wang, Carolin M. Sutter-Fella, Peter Lobaccaro, Mark Hettick, Maxwell Zheng, Der-Hsien Lien, D. Westley Miller, Charles W. Warren, Ellis T. Roe, Mark C. Lonergan, Harvey L. Guthrey, Nancy M. Haegel, Joel W. Ager, Carlo Carraro, Roya Maboudian, Jr-Hau He, and Ali Javey, “Increased Optoelectronic Quality and Uniformity of Hydrogenated p-InP Thin Films”, *Chemistry of Materials* 2016 28 (13), 4602-4607

I collected and analyzed the Transient Photocapacitance and Photocurrent Spectra for the above publication that will be re-produced in this chapter. H.S. Wang fabricated the samples. All authors contributed to writing process with primary drafting executed by H.S. Wang.

Optical Absorption in Semiconductors

Three different methods are used in this dissertation to characterize the sub-bandgap density of states (DOS) in the solar cell absorbers investigated: external quantum efficiency (EQE), transient photocapacitance spectroscopy (TPC), and transient photocurrent spectroscopy (TPI). All of these measurements are predicated on the absorption of light by the semiconducting absorber. Therefore, we will begin with a brief discussion of absorption processes. Optical absorption in solids can result from a wide variety of processes including: the excitation of crystal vibrations or phonons; the excitation of free electrons and holes within allowed bands ('free carrier absorption'); the excitation of electrons from the valence to the conduction band; and excitation of electrons (or holes) from defects to the conduction (or valence band). We are interested in the last two processes which dominate absorption for the range of optical energies we are interested in here. Transitions from the valence band to the conduction band allow us to measure the band gap energy using Tauc plots, as described in Appendix 7.2. Transitions from various states in the band gap or the band edges to the valence or conduction band can yield information about the sub-bandgap DOS and will be discussed here.

The rate of transitions, and thus the absorption, for a given optical energy is governed by:

$$\alpha(E) \propto \int |\langle i|ex|f \rangle|^2 g_{unocc}(E') g_{occ}(E' - E) dE', \quad (3.1)$$

where $\langle i|ex|f \rangle$ is the optical matrix element associated with the transition, g_{occ} is the density of states associated with the occupied band or defect, g_{unocc} is the same for the unoccupied states, and E is the photon energy. Let us consider transitions from

an occupied valence band state to a defect state (i.e. *any* state in the band gap). We define all energies relative to the valence band maximum so that $E_V = 0$. For very low illumination levels, the Fermi energy, E_F , determines which portion of the defect band is occupied. Assuming that the optical matrix element varies slowly as compared to the densities of states we obtain:

$$\alpha(E) \propto \int_{E_V}^{E_V+E} F(E')g_d(E')g_V(E' - E)dE'. \quad (3.2)$$

where $F(E')$ is the Fermi distribution given by equation 2.1 and g_d is the generic unoccupied state in the band gap. For spectra taken at room temperature and below, most transitions allow us to treat the Fermi Dirac distribution as a step function. However, if the transition is within ~ 0.25 eV of E_F at room temperature then partial occupation of the defect will obscure the defect's true activation energy. Depending on the doping level of the material, this means transitions with energies less than $E_g/2$ merit extra scrutiny. We will come back to this question momentarily. For now, allowing $F(E')$ to be treated as a step function we obtain:

$$\alpha(E) \propto \int_{E_F}^{E_V+E} g_d(E')g_V(E' - E)dE'. \quad (3.3)$$

Here we should pause to consider the allowed transitions for an example sub-bandgap DOS. Figure 10 shows such a DOS along with various transitions labeled in both an illustration of the transitions between states and the resulting sub-bandgap absorption spectrum. Transition 'A' is a transition from an occupied valence band state to an unoccupied conduction band state. If the energy of the photon driving the transition is much bigger than the minimum needed to drive this transition, then the integral in equation 3.3 would include transitions from deeper within the valence band

to the conduction band minimum, and from the valence band maximum to higher energies in the conduction band. Moving from these higher energy transitions to one just above E_g one might see features in the absorption spectrum due to the fact the the valence and conduction band DOS are not constant. While we are not concerned with this portion of the spectrum, we will make analogous considerations for lower energy transitions and again ask whether features in the valence or conduction band DOS can impact the sub-band gap features.

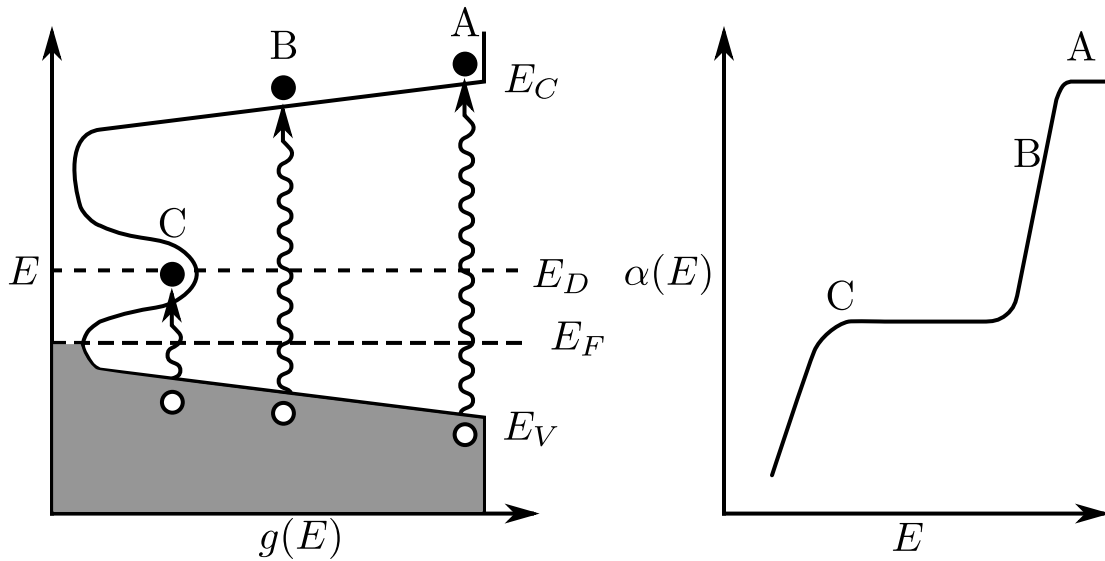


FIGURE 10. The left half of this figure shows an example sub-bandgap DOS (x-axis, logarithmically scaled) as a function of energy with transitions corresponding to features in the sub-bandgap absorption spectra shown in the right half of the figure.

Transition ‘B’ indicates transitions from the valence band maximum to the conduction band edge. Transition ‘C’ illustrates transitions from the valence band to a defect state. The impact of these transitions on a spectrum will be dominated by the density of states for the feature within the band gap so long as the valence band density of states is slowly varying compared to the defect DOS in question over the range of energy from E_V to $E_V - (E - E_D)$. This criterion is fairly easy to meet,

as $E - E_D$ is typically small for the relevant values of E . Unlike the above gap situation described before, in the case that E is significantly greater than E_D the features that would be introduced to the absorption due features in the valence band will be obscured by the interband transitions. In the case of a somewhat deep defect, features in the valence band might add a few small features to what is shown as a plateau between transitions ‘B’ and ‘C’ in Figure 10. It would not greatly change the apparent energy of the defect transition or the total absorption associated with it near $E = E_D$. Transitions like ‘B’ yield information about the band-tail states, while those like ‘C’ yield information about defects deeper in the gap. We will consider these in turn.

The Urbach Energy and Disorder

A perfect crystal would be expected to have a density of states that approaches zero at E_V with a dependence proportional to $(E_V - E)^{1/2}$ and likewise $(E - E_C)^{1/2}$ for E_C . However, an exponential band of tail states above E_V (below E_C) is almost universally observed. As illustrated in Figure 3, this is due to disorder in the crystal lattice. This is manifest in the absorption below E_G as an exponential decline with the form:

$$\alpha(E) \propto \exp\left(\frac{E - E_g}{E_U}\right), \quad (3.4)$$

where E_U is the ‘Urbach Energy’ named for Franz Urbach who first observed a temperature dependent exponential band-edge in AgBr crystals while studying materials used in photographic emulsions for the Eastman Kodak company in 1953. Further investigation revealed that strain, defects and the phonon temperature contribute to the Urbach energy [39–41]. Therefore, the Urbach energy of a particular

semiconductor is of interest for applications in solar cells because the associated disorder will impact charge transport and recombination. One such example is that of the larger Urbach energies in $\text{Cu}_2\text{ZnSn}(\text{Se}_{1-x}\text{S}_x)_4$ correlating with the voltage deficit $E_g - V_{oc}$ that I demonstrated in 2012 [42]. Figure 11 shows increasing Urbach Energy with increasing x in $\text{Cu}_2\text{ZnSn}(\text{Se}_{1-x}\text{S}_x)_4$.

Example of Urbach Energy Characterization in $\text{Cu}_2\text{ZnSn}(\text{Se}_{1-x}\text{S}_x)_4$

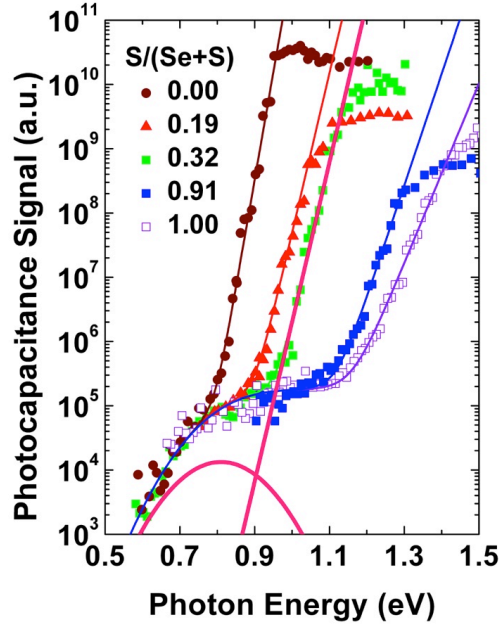


FIGURE 11. Urbach energy vs x in $\text{Cu}_2\text{ZnSn}(\text{Se}_{1-x}\text{S}_x)_4$. As the sulfur content increases the bandgap widens and the E_U increases. A deep defect transition is seen at ~ 0.8 eV.

In this instance, it was desirable to increase the bandgap by alloying with sulfur in place of selenium to optimize the bandgap for a single-junction solar cell. However, E_U increased along with E_G while the open circuit voltage of the resulting solar cell did not. This is demonstrated in Figure 12:

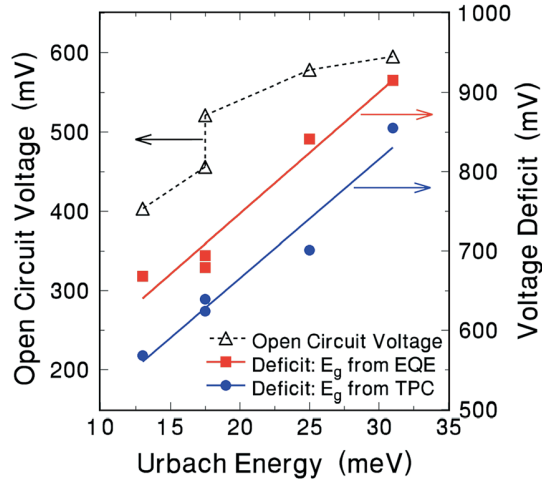


FIGURE 12. Voltage deficit versus Urbach Energy in $\text{Cu}_2\text{ZnSn}(\text{Se}_{1-x}\text{S}_x)_4$. The voltage deficit was found to increase approximately linearly with the E_U limiting the performance of solar cells based on this material. The slight difference in E_G as measured via TPC and EQE was attributed to an absorption length at E_g exceeding the depletion width.

The behavior was consistent with a model wherein band-tail states or a deeper defect whose density correlated with the Urbach energy limited V_{oc} . Subsequent studies corroborated this interpretation[43], and the goal of lowering the E_U has guided ongoing efforts to develop higher performance $\text{Cu}_2\text{ZnSn}(\text{Se}_{1-x}\text{S}_x)_4$ analogues such as $\text{Ag}_2\text{ZnSn}(\text{Se}_{1-x}\text{S}_x)_4$ [44]. The impact of the deeper defect seen in Figure 11 was unclear, but sometimes the impact of such a defect is readily apparent.

Defect Absorption

As demonstrated in Figures 4 and 5, the energy of a point defect within the band gap is, along with its density, crucial to understanding how it will impact the performance of a solar cell. In order to assign transition energies to the absorption associated with a defect, a little more work is needed. Returning to equation 3.3

we find that treating g_V as relatively constant over the range E_V to $E_V - (E - E_D)$ yields

$$\alpha(E) \propto \int_{E_F}^{E_V+E} g_d(E') dE'. \quad (3.5)$$

If we choose a Gaussian distribution for the density of states associated with g_D equation 3.5 becomes

$$\alpha(E) \propto \frac{G_D}{\sigma_d \sqrt{2\pi}} \int_{E_F}^{E_V+E} \exp\left(-\frac{(E' - E_d)^2}{2\sigma_d^2}\right) dE', \quad (3.6)$$

where E_d is the defect energy and σ_d^2 is the variance of the Gaussian distribution. We can split this into a sum of two integrals

$$\alpha(E) \propto \frac{G_D}{\sigma_d \sqrt{2\pi}} \left\{ \int_0^{E_V+E} \exp\left(-\frac{(E' - E_d)^2}{2\sigma_d^2}\right) dE' - \int_0^{E_F} \exp\left(-\frac{(E' - E_d)^2}{2\sigma_d^2}\right) dE' \right\}, \quad (3.7)$$

each of which is, by definition an *error function*. So long as $E_F - E_D \gtrsim 2\sigma_d$ the second integral evaluates to ≈ -1 and the absorption due to excitation of an electron from the valence band to an unoccupied defect should obey

$$\alpha_d(E) \propto \frac{G_D}{2} 1 + \operatorname{erf}\left(\frac{E - E_D}{\sigma_d \sqrt{2}}\right). \quad (3.8)$$

Transitions from an occupied defect to the conduction band would obey the same equation. Equation 3.8 has been used extensively fit sub-bandgap absorption spectra [42, 45–53]. As evidenced by the extensive use of these methods, characterizing defects can be very helpful in providing feedback for solar cell fabrication efforts. One recent example of a straightforward connection I was able to

make between point a defect and photovoltaic performance resulted from a study of Hydrogenation of InP thin films [54]. Figure 13 shows the TPI spectrum for a set of five solar cells utilizing InP absorbers.

Example of defect characterization in InP

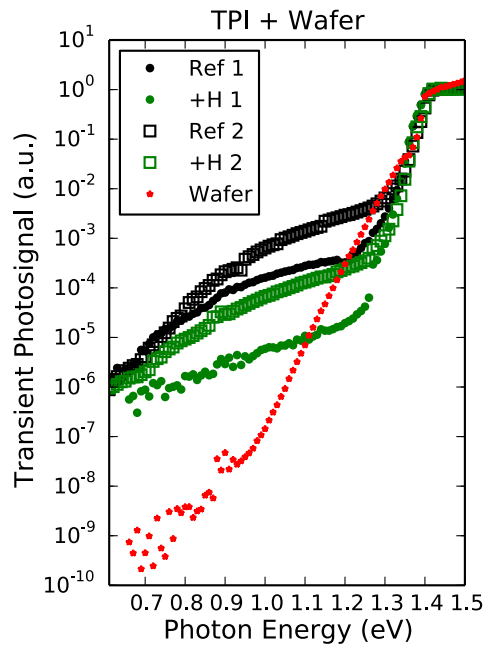


FIGURE 13. Transient photocurrent spectra for a series of five solar cells with InP absorbers. All five show $E_g = 1.41$ eV and $E_u \leq 15$ meV. The five solar cells utilized for their absorbers: a commercial wafer (red stars) and a pair of TF-VLS grown thin-films split into cells completed with (green) and without (black) hydrogenation.

The sample set included one solar cell made using a commercially produced indium phosphide wafer for the absorber, and four utilizing thin-film InP absorbers grown by a novel technique: ‘Thin-Film Vapor-Liquid-Solid’ (TF-VLS) growth. TF-VLS growth produces a thin-film of poly-crystalline InP directly on a molybdenum substrate by phosphorization of liquid InP that is prevented from de-wetting with the use of a porous silica cap [54]. The TF-VLS grown films yielded solar cells with

promising efficiencies, but performance was significantly lower than that produced by the wafer. TPI reveals only a what appears to be a shallow dopant in the wafer based cell, but a broad defect band centered at 1.1 eV and extending towards mid-gap in the TF-VLS cells. Hydrogenation of the InP was resulted in a reduction of this defects density by a factor of 10-30. The effects on the performance were notable.

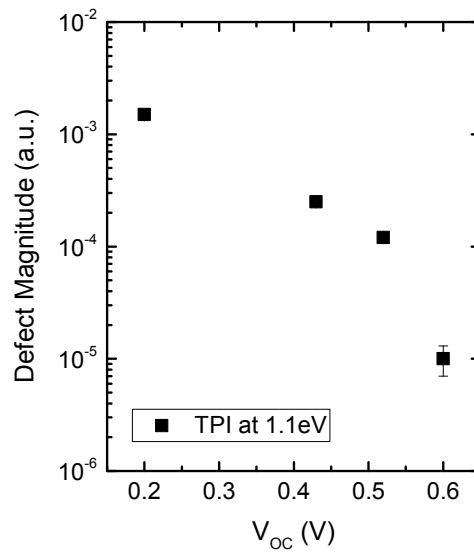


FIGURE 14. The open circuit voltage for a series of InP solar cell versus the strength of the TPI signal at 1.1 eV.

Figure 14 shows a strong correlation between V_{oc} and the strength of the TPI signal at 1.1 eV. This result helped to explain an average improvement of ~ 100 mV in V_{oc} resulting from hydrogenation in tests of ~ 500 solar cells. In conjunction with data on the efficiency of Zn-doping in the TF-VLS films it led to a working theory that Zn_i defects left not properly incorporated into the InP lattice were responsible for the defect absorption and were passivated by the hydrogenation.

So far I have used EQE, TPC, and TPI almost interchangeably on the grounds that they are all predicated by absorption and allowed absorption processes dominate

their features. Indeed, nothing in particular about the way the examples above were interpreted depended on the things that distinguish these techniques. I will now explain the differences in how these measurements are performed and the impact that can have on the resulting spectra.

Comparing EQE, TPC, and TPI

EQE measurements, in contrast to TPC and TPI are performed near steady-state. The cell is typically held at 0 volts (short-circuit) while being illuminated with weak, monochromatic light. This light is chopped and a lock-in amplifier is used to reject noise and isolate the photo-current generated by the light.

In contrast to EQE, TPC and TPI are performed with the sample far from steady-state. A voltage pulse is used to fill states in the depletion region that would otherwise be empty by raising them above the Fermi level. A transient is produced as these charges thermally escape the trap states. The difference between this transient in the dark and under weak monochromatic illumination is the TPC or TPC signal. For TPC, you monitor the sample capacitance. For TPI, the current is measured. While TPC is sensitive to the *net* charge leaving the depletion region, TPI is sensitive to the total. Put another way, if an electron exits to the left, and a hole exits to the right, the current adds, however, the net charge in the depletion region has not changed. For this reason, good minority carrier collection *from the depletion region* suppresses the TPC signal, particularly above the bandgap and near the band edge. Minority carriers left in deep defects are unlikely to escape on the timescale permitted for a typical transient. This allows one to estimate the minority carrier collection by

aligning the spectra in the defect band and using the formula (shown for electrons as the minority carrier):

$$\frac{n}{p} = \frac{1 - R}{1 + R}. \quad (3.9)$$

Where R is the ratio TPC/TPI above gap, after aligning the spectra in a defect band. Applying this method to the InP samples described in the previous section showed an increase in the minority carrier collection *from the depletion region* from 95 to > 99 %. Note that this does not describe total minority carrier losses as recombination may occur outside the depletion region. Nonetheless, poor minority carrier collection from the depletion region, where an electric field is present to facilitate charge separation would be a strong indication that non-radiative recombination is a bulk problem in the material under test. The execution of TPC, TPI and the derivation of the analysis described above have been described in more detail in other dissertations [55–60].

Because TPC can be suppressed by minority carrier collection above gap the ratio of the signals above and below E_g is not indicative of the relative density of the defect DOS to the band edge DOS. However, in TPI and EQE the opposite is true. Because any loss mechanisms affect all photocarriers in the conduction and valence bands, regardless of their origins, it is appropriate to align TPI and EQE spectra for devices with the same absorber material near E_g in order to compare the relative density of defect bands between samples [59].

In the chapters that follow, I will use the techniques and analyses introduced in this chapter to characterize defects found in $\text{CH}_3\text{NH}_3\text{PbI}_3$ and $\text{CH}_3\text{NH}_3\text{Pb}(\text{I}_{1-x}\text{Br}_x)_3$ thin-films. These defects will be connected to the performance of perovskite solar cells based on these materials or non-radiative recombination rates in sister samples.

CHAPTER IV

DEFECTS IN $\text{CH}_3\text{NH}_3\text{PbI}_3$ AND HYSTERESIS

Portions of this chapter were taken from D.W. Miller, G.E. Eperon, E.T. Roe, C.W. Warren, H.J. Snaith, M.C. Lonergan, “Defect states in perovskite solar cells associated with hysteresis and performance”, *App.Phys.Lett.*, vol. 109, pp. 153902, Oct. 2016. This paper was written primarily by D.W. Miller with the editorial assistance of my co-authors. I collected the data with some assistance from E.T. Roe. The samples were fabricated by G.E. Eperon, and the description of fabrication is only lightly edited by D.W.Miller.

Introduction

As discussed in Chapter I, perovskite solar cells with the general formula ABX_3 have been the focus of a worldwide swarm of research activity leading to an unprecedented pace of progress. The methylammonium lead triiodide perovskite ($\text{CH}_3\text{NH}_3\text{PbI}_3$), was the first demonstrated perovskite solar cell. It’s efficiency has risen from 3.8 % in 2009 to 20.1 % today [17, 61]. However, characterization of the electronic properties of perovskite thin films in perovskite solar cells (PSCs) has not kept pace with publications on perovskite synthesis, device fabrication and performance. In particular, characterization of the sub-bandgap density of states (DOS) is needed as it has a strong influence on carrier mobilities and recombination rates and can be used to inform fabrication efforts.

The sub-bandgap DOS can be divided into two parts: the valence and conduction band edges with exponential distributions and defect bands with Gaussian distributions. The energetic width of the band edges is described by the Urbach

Energy, E_u , and is related to the degree of disorder in the crystal. Research to date has found E_u between 15–18 meV in $\text{CH}_3\text{NH}_3\text{PbI}_3$ thin films [62–64]. This compares favorably with other thin-film technologies and fits a trend that has been observed across thin-film materials between E_u and the voltage deficit, $E_g - V_{oc}$, where E_g is the band gap energy and V_{oc} is the open-circuit voltage [62]. Indeed, similar trends have been observed within alloys of $\text{CuIn}_{1-x}\text{Ga}_x\text{Se}_2$ and $\text{Cu}_2\text{ZnSnSe}_{2-x}\text{S}_x$ pointing to fundamental limits on device performance set by E_u [42, 47]. While the values of E_u reported are fairly consistent, there is a great deal of variation in the energy and density of defect states observed in $\text{CH}_3\text{NH}_3\text{PbI}_3$ thin films. Defects have been reported at 0.24 and 0.65 eV below the conduction band [63], and 0.17, 0.3 and 0.5 eV above the valence band [65, 66]. Densities associated with these defects range from $1 \times 10^{15}\text{cm}^{-3}$ to $3 \times 10^{16}\text{cm}^{-3}$. None of these studies found defects at the same energy as any other. This wide variation may be explained by the use of different preparation methods. Further, experience with other thin-film technologies demonstrates that the electronic properties of thin films can be strongly influenced by other layers (glass, transparent conducting oxides, emitters, back-contacts, etc.) in the device [48, 67–69]. Therefore, variations in cell architecture and associated processing steps may also contribute the variability in observed defects.

Characterization of the sub-bandgap DOS is particularly useful when it is connected to solar cell performance. Efforts to do so for perovskites are hindered by the relatively low number of samples for which the sub-bandgap DOS has been characterized (one $\text{CH}_3\text{NH}_3\text{PbI}_3$ sample in each of the studies summarized above), difficulty in comparing these samples to each other, and rate dependent hysteresis in current density-voltage (J - V) behavior. Rate dependent hysteresis was not adequately addressed in much of the early literature,[22] and it has since become

clear that meaningful performance characterization must consider voltage ramp rate, ramp direction, pre-scan bias, and pre-scan illumination conditions [34, 70].

Here I report rate-dependent J - V , external quantum efficiency (EQE) and transient photocapacitance (TPC) spectra for a series of five planar $\text{CH}_3\text{NH}_3\text{PbI}_3$ -based photovoltaics. All measurements were performed in a dry- N_2 atmosphere at 298 K. As previous studies reporting on the sub-bandgap DOS found little agreement, perhaps owing to variation in fabrication methods, I chose to include PSCs with absorbers formed by dip and vapor conversion. In all cases, the device structure was Glass / FTO / TiO_2 / $\text{CH}_3\text{NH}_3\text{PbI}_3$ / spiro-MeOTAD / Au. The resulting data show that a higher density of defect states in the $\text{CH}_3\text{NH}_3\text{PbI}_3$ absorber, as revealed by EQE and TPC, correlates with diminished performance at low voltage ramp rates and more pronounced hysteresis at high ramp rates. It is not immediately apparent what causes the variation of defect density, but both dip and vapor converted devices showed a wide variation in J - V and the sub-bandgap DOS. Let us begin with a description of the fabrication methods.

Sample Fabrication

Device Structure and Materials

The results described in this chapter were obtained on planar heterojunction perovskite solar cells (PSCs) with $\text{CH}_3\text{NH}_3\text{PbI}_3$ absorbers deposited by two methods, dip conversion and vapor conversion. In all cases, the device structure was Glass/FTO/ TiO_2 / $\text{CH}_3\text{NH}_3\text{PbI}_3$ /spiro-MeOTAD/Au. Spiro-OMeTAD refers to the optically transparent hole conductor 2,2',7,7'-tetrakis-(N,N-di-p-methoxyphenylamine)9,9'-spirobifluorene, which was purchased from Borun

Chemicals. $\text{CH}_3\text{NH}_3\text{PbI}_3$ was synthesized according to a reported procedure [71]. All other materials were purchased from Sigma-Aldrich and used as received.

Substrate Preparation

Devices were fabricated on fluorine-doped tin oxide (FTO) coated glass (Pilkington, $7 \Omega \square^{-1}$). Initially, FTO was removed from regions under the anode contact by etching the FTO with 2M HCl and zinc powder. Substrates were then cleaned sequentially in hallmanex detergent, acetone, propan-2-ol (IPA) and oxygen plasma. A hole-blocking layer of compact TiO_2 was deposited by spin-coating a mildly acidic solution of titanium isopropoxide in anhydrous ethanol ($350 \mu\text{l}$ in 5 ml ethanol with 0.013 M HCl), and annealed at 500°C for 30 minutes. Spin-coating was carried out at 2000 rpm for 60 seconds.

$\text{CH}_3\text{NH}_3\text{PbI}_3$ Vapor-Converted Film Formation

A 0.75 M solution of PbI_2 in dimethylformamide was spin-coated on the titania-coated FTO substrate at 3000 rpm for 15 s, with both solution and substrate at 85°C immediately prior to coating. Films were subsequently dried at 85°C for 10 minutes. The resulting PbI_2 films were then transferred into a nitrogen-filled glovebox and placed on raised supports in a small sealed glass chamber with the lead iodide facing upwards. A mass of 900 mg of $\text{CH}_3\text{NH}_3\text{I}$ was crushed with a pestle and mortar and placed on the bottom surface of the chamber. The chamber was then heated from below on a hotplate at 155°C for 5 hours. The resulting $\text{CH}_3\text{NH}_3\text{PbI}_3$ thin films were rinsed in anhydrous IPA and annealed for 30 minutes at 100°C .

CH₃NH₃PbI₃ Dip-Converted Film Formation

A 1M solution of PbI₂ in dimethyl sulfoxide was spin-coated onto the titania-coated FTO substrate at 4000 rpm for 30 s. This film was then rapidly transferred into a bath of 10 mg/ml CH₃NH₃I in IPA for 10 minutes at room temperature. The resulting CH₃NH₃PbI₃ thin films were then rinsed in IPA and annealed at 100° C for 10 minutes.

Perovskite Solar Cell Fabrication and Care

The perovskite was deposited on the titania-coated substrate as described above. A hole-transporting layer was then deposited via spin-coating a 96 mg/ml solution of spiro-OMeTAD in chlorobenzene, with additives of lithium bis(trifluoromethanesulfonyl)imide (0.018 M) and 4-tert-butylpyridine (0.066 M). Spin-coating was carried out at 2000 rpm for 45 seconds. Devices were then left overnight in air for the spiro-OMeTAD to dope via oxidation [72]. Finally, gold electrodes were thermally evaporated under vacuum of 10⁻⁶ Torr, at a rate of 0.1 nm/s, to complete the devices. From this time on, air exposure was minimized. Samples were shipped from Oxford University to the University of Oregon in vacuum packs containing dessicants.

All subsequent measurements were carried out in a sealed Linkam LTS-350 stage purged with dry N₂. Stage temperature was maintained at 298 ± 2 K during all measurements unless explicitly specified to be otherwise. Air exposure was limited to less than 10 minutes per sample while contacting and storing samples. Between measurements samples were stored in the dark in a desiccator purged with dry N₂.

Using these methods a total of six samples were fabricated for the study. Three samples were fabricated using vapor conversion of the CH₃NH₃PbI₃ layer and three

using the dip conversion. One of the dip converted samples was shunted and therefore excluded from the study. The remaining dip-converted samples will be referred to as ‘Dip 1’ and ‘Dip 2’, while the vapor converted samples are referred to as ‘Vapor 1’, ‘Vapor 2’, and ‘Vapor 3’. The following sections investigate and detail the device performance and defect properties of these samples.

Current-Voltage Hysteresis

PSCs are subject to rate-dependent current-voltage hysteresis. This effect can obscure the operational efficiency of the PSC if care is not taken to establish that a near steady-state limit has been reached. At the same time, characterizing the hysteresis itself may provide insights into perovskite materials. I performed four types of J - V sweeps: reverse sweeps from 1.4 to 0 V and forward sweeps from 0 to 1.4 V with each direction swept at both 2 mV / s and 360 mV / s. Note that I have defined the photocurrent as negative so that forward bias on the diode is positive and “forward” sweeps imply a positive ramp rate. In every case, the sample was pre-biased for 10 s at V_{oc} under 1-sun illumination.

Figure 15 compares the ± 2 and ± 360 mV / s J - V curves for Vapor 1. This sample displays pronounced hysteresis when voltage is swept at ± 360 mV / s. Corresponding J - V curves for the other four samples can be found in Appendix 7.1. Power conversion efficiencies for the samples studied varied from 0.9 to 9.6 % depending on sample, ramp rate and direction, and pre-bias condition. The J - V sweeps at ± 2 mV / s had almost no hysteresis in the power quadrant. One should note, there is evidence of a transient effect enhancing J_{SC} for the +2 mV / s scan due to the 10 s pre-bias at V_{OC} before beginning each scan. This indicates that illumination under the open-circuit condition changes the state of the sample in a

TABLE 1. Deposition method and quasi-steady-state J - V characteristics for the devices measured by EQE and TPC in this study. Note that faster J - V scans yielded significantly enhanced performance with power conversion efficiency (PCE) up to 9.6%.

Sample ID	PCE %	FF %	V_{OC} mV	J_{SC} mA/cm ²
Dip 1	0.7	27	810	3.2
Dip 2	8.4	59	930	15.2
Vapor 1	2.1	47	800	5.6
Vapor 2	5.2	36	930	15.4
Vapor 3	7.3	46	970	16.5

way that improves carrier collection. For this reason, parameters extracted from the -2 mV / s scan will be quoted as the quasi-steady-state performance parameters. Table 1 summarizes these performance parameters —fill factor (FF), V_{oc} , short-circuit current density (J_{SC}), and power conversion efficiency (PCE) —extracted from J - V data taken at -2 mV / s.

My J - V data agree with the observations of many others working on a variety of planar perovskite cells in the following ways: 1) at the slower voltage ramp rate (± 2 mV / s), the effect of pre-bias and hysteresis is minimized or eliminated; 2) at the faster rate (± 360 mV / s), significant gains over quasi-steady-state performance are made in V_{oc} and J_{sc} when ramping toward short-circuit from $V > V_{oc}$; 3) at the faster rate, the FF is significantly higher for reverse sweeps than for forward sweeps. Explanations for this rate-dependent hysteresis often invoke defects in the perovskite crystal in the form of mobile ions that work to screen applied fields and/or recombination centers that can be neutralized by minority carrier injection [34, 35, 70, 73]. It has been noted that these defects may have a significant impact on performance at too low a concentration to easily observe with standard approaches [34]. However, our measurements of this sample set reveal sub-bandgap optical transitions indicative

of defects. I find that the defect density correlates with both steady-state performance metrics and the degree of hysteresis in performance metrics at faster ramp rates.

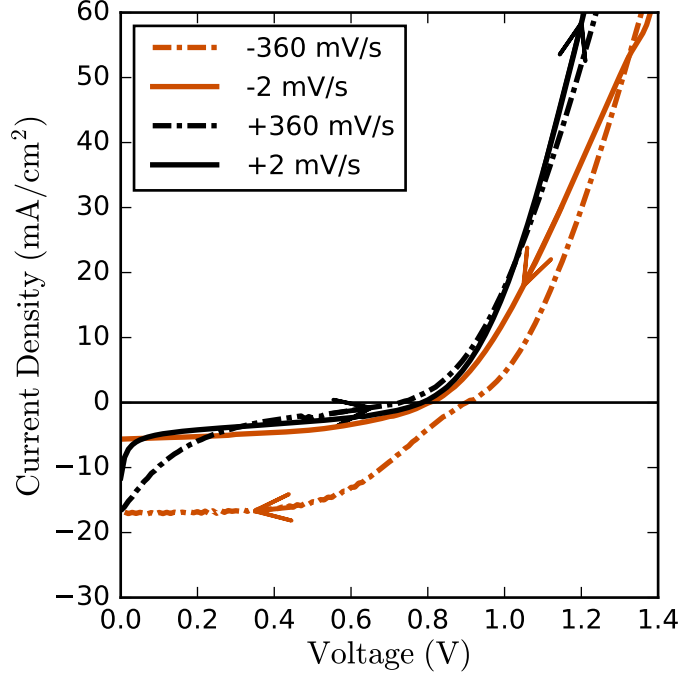


FIGURE 15. Forward and reverse J - V curves at different scan rates for Vapor 1. Note the large hysteresis for the ± 360 mV / s scans is almost entirely eliminated at ± 2 mV / s in the power quadrant.

Sub-Bandgap External Quantum Efficiency

Sub-bandgap external quantum efficiency (EQE) and transient photo capacitance (TPC) spectra were obtained at 298 K for all devices and are shown in Figures 16 and 17. Band-gaps were determined from EQE using the method of Tauc [74]. Relevant plots are shown in Appendix 7.2. In every case, these spectra reveal a relatively sharp absorption edge below $E_g = 1.58$ eV, with $E_u = 15$ to 18 meV. This agrees with prior work [62–64]. It is meaningful that the TPC and EQE extracted Tauc plots yield the same E_g . This is not always the case [42] and indicates that

either: the depletion region extends through most of absorber and/or; the absorption length is shorter than the depletion width.

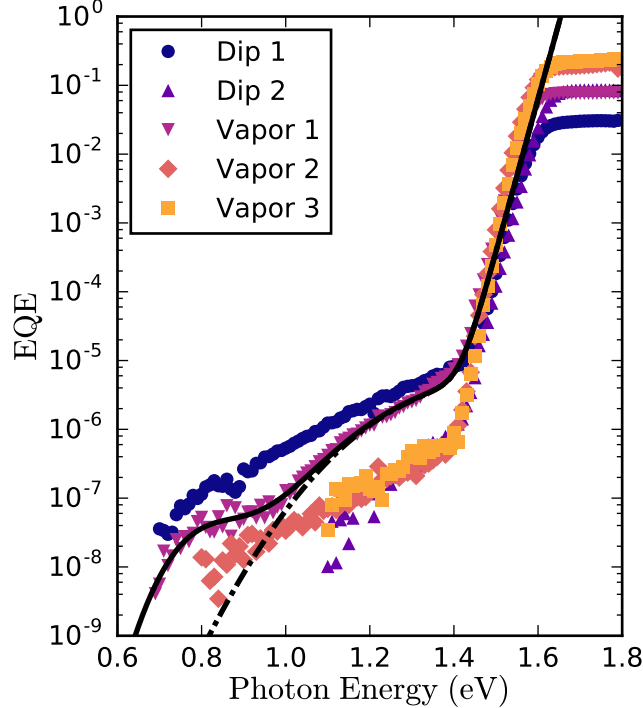


FIGURE 16. Sub-bandgap EQE spectra for the five devices studied. The spectra reveal $E_g = 1.58$ eV and $E_u = 15$ meV in all devices while the defect response varied strongly across the samples. It was possible to fit all the spectra with a pair of defects at 1.34 and 0.76 eV by varying only the magnitude of the defects from one sample to another. The fit to Vapor 1 is shown with (full line) and without (dash-dotted line) the influence of the 0.76 eV defect.

As discussed in Chapter III, the Urbach energy, E_u , is related to the level of disorder in a crystalline structure. Low E_u has been linked to high performance in photovoltaic devices. The Urbach energy is the inverse slope of the exponential bandtail at energies just below E_g , and appears as the linear region on the semilogarithmic plot shown in Figure 16. The low E_u consistently achieved by $\text{CH}_3\text{NH}_3\text{PbI}_3$ is remarkable for a material processed so quickly (conversion can complete in a matter of seconds and subsequent annealing treatments are 10-30 minutes for the samples in this study) and at such low temperatures (around 100 °C).

Consider that to achieve comparably low E_u in AgInSe₂, CuInSe₂ and CuZnSnSe₂ at least one processing step over 500 °C is required [42, 48, 50]. The relative ease with which perovskites achieve a low E_u may help explain the rapid rise in efficiency of PSCs. Despite uniformly low E_u , the performance varied widely for this sample set.

Examining the EQE at energies below the ‘Urbach edge’ I find a region of non-exponential behavior. This region could be due to absorption by point defects in the crystal. Point defects would include broken bonds, vacancies or substitutional defects as opposed to the strained bonds and thermal deviations from lattice points that contribute to non-zero Urbach energy. I observed some defect response that varied in magnitude and energetic distribution across the samples investigated. Following the discussion in chapter III, the contribution by a Gaussian point defect to the EQE spectrum is fit by a function of the form:

$$EQE_d(E) = \kappa \frac{G_d}{2} \left[1 + \operatorname{erf} \left(\frac{E - E_d}{\sigma_d \sqrt{2}} \right) \right]. \quad (4.1)$$

Here, “erf” is the error function, and E_d , G_d and σ_d^2 are the energy, volume density, and variance of the Gaussian energy DOS associated with the point defect [47, 51, 75]. The variable κ is a constant of proportionality specific to EQE. For the purposes of this discussion the product κG_d will be referred to as the “Defect EQE”. Because G_d is the *volume density* of the defect with units of cm^{-3} as opposed to the density at the peak of the Gaussian density of states with units of $eV^{-1} cm^{-3}$ it follows that κG_d then yields the *total* contribution to the EQE by a defect with a Gaussian density of states centered at E_d for $E \gg E_d$. For a pair of defects, one would sum two such expressions, each with its own E_d , κG_d and σ_d^2 .

The EQE spectra below the exponential band edge are well fit using a function of this form. For a single defect model, best fits for some EQE spectra (Dip 1, Vapor

1 and Vapor 2) yield $E_d > E_g$ and a full width at half max (FWHM= $2\sqrt{2\ln 2}\sigma_d$) exceeding 0.95 eV. This is an unreasonably large value. Vapor 1 in particular is simply not well-fit using a single defect model. Meanwhile, TPC spectra for Dip 1 and Vapor 1 were well fit by single defect near 1.34 eV with a FWHM of 0.29 eV. This led us to consider a two defect model for all the spectra using one defect fixed near 1.34 eV and another at a lower energy. Simultaneously minimizing the residuals for all the spectra with the higher energy defect constrained to 1.34 eV results in best fits of 1.34 ± 0.04 eV and 0.76 ± 0.02 eV with FWHMs of 0.38 ± 0.05 eV and 0.09 ± 0.02 eV, respectively. Thus, it is possible to fit all of the EQE and TPC spectra by tuning only the parameter proportional to G_d (i.e. the Defect EQE for EQE spectra) for the 1.34 and 0.76 eV defects while keeping the FWHM and energy of the underlying Gaussian distributions fixed. Individual fits to each EQE spectrum are shown in Appendix 7.3.

Transient Photocapacitance Spectroscopy

As discussed in Chapter III, there are some differences between the EQE and TPC measurement that impact how I interpret the resulting spectra. While the very small currents associated with non-zero sub-bandgap EQE could be due to photocurrent generated in any part of the device, TPC is most sensitive to the bulk of the absorber. In particular, its sensitivity increases linearly from zero at the junction to a maximum at the edge of the depletion region. TPC also differs from EQE in that the above-gap response is strongly suppressed by minority carrier collection [47]. Even if this device is not an ideal one-sided p-n junction, capacitance measurements like TPC will still be most sensitive to the layer of the device with the lowest carrier density, longest depletion width, and lowest capacitance. This is most likely the perovskite layer. Therefore, EQE facilitates comparison of the

absolute defect magnitude between samples and TPC localizes the defect response in the depletion region of the absorber.

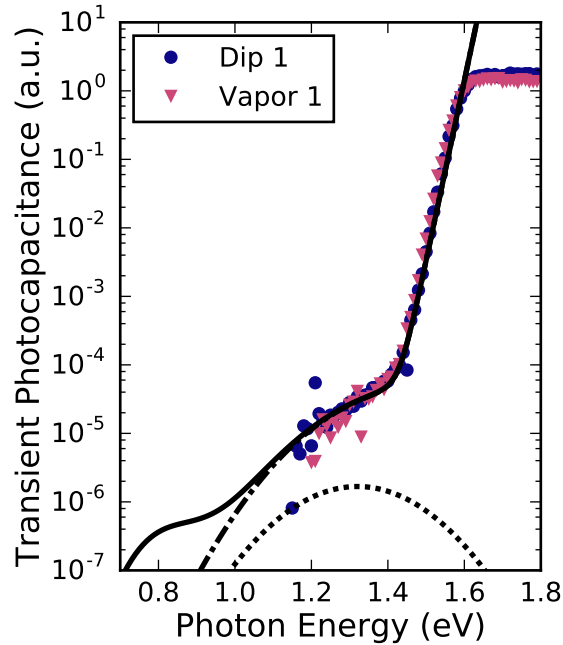


FIGURE 17. TPC spectra for Dip 1 and Vapor 1. The best fit to the defect band from EQE spectrum for Vapor 1 with (full line) and without the contribution from the 0.76 eV defect (dash-dotted line) are overlaid on the data. While the 1.34 eV feature remains a good fit, the data can neither confirm nor exclude the presence of a 0.76 eV defect. The dotted line indicates the underlying gaussian defect band associated with the 1.34 eV transition.

Figure 17 compares the TPC spectra for Dip 1 and Vapor 1 with the fit to the EQE spectrum for Dip 1. I observe the same E_g and nearly the same E_u . The defect response in the TPC spectrum is dominated by the 1.34 eV defect while the 0.76 eV defect transition, if present, is below the detection limit of the TPC measurement. Fits to the individual TPC spectra can be found in Appendix 7.3. This suggests that the 1.34 eV defect band seen in the EQE spectra is due to a defect in the bulk of the perovskite absorber. The absence of the 0.76 eV feature may indicate that it is an interface defect or that the EQE signal originates outside the absorber. However,

I would need better signal to noise in TPC to be sure because its presence does not strongly impact the fits of the EQE spectra until 1.1 eV. The 1.34 eV defect appears in our TPC spectra for Dip 1 and Vapor 1, which showed the highest levels in EQE, but for the other samples it is not observed.

Correlations with Device Performance

Figure 18 presents the performance of the samples at -2 and -360 mV / s following a 10 s pre-bias under 1-sun illumination at V_{OC} plotted against the defect EQE, κG_d , of the 1.34 eV defect. The defect EQE is correlated to several cell metrics measured at -2 mV / s. I observe a loss of at least 100 mV in V_{OC} , 10 mA cm⁻² in J_{SC} , and 3 to 8 % in PCE for cells with a defect EQE in excess of 10^{-6} as compared to their low defect counterparts. For scans at -360 mV / s, the defective cells recover performance parameters much closer to their low defect counterparts. The less defective cells show a much smaller difference between the two ramp rates. This establishes a correlation between poor steady state performance, large hysteresis at high ramp rates, and the defect EQE.

The correlation of the defect density with steady-state performance parameters, particularly V_{OC} , is indicative of defect mediated recombination. The presence of defect mediated recombination is corroborated by the large dynamic range of the TPC spectrum in the two worst performing devices, Dip 1 and Vapor 1. As described in Chapter III, the above gap TPC signal is suppressed by minority carrier collection while transient photocurrent (TPI) is not. By assuming minority carrier collection from a state near mid-gap is essentially zero and therefore aligning the TPI and TPC spectra at this energy, the above gap ratio of the TPC and TPI signals yields the minority carrier collection efficiency *from the depletion region*. The TPC and TPI

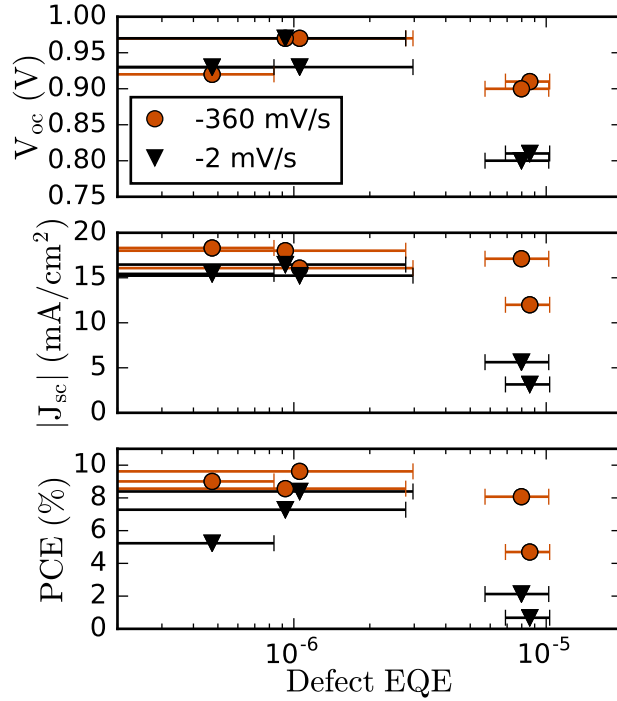


FIGURE 18. Performance parameters extracted from fast (orange circles) and slow (black triangles) J - V scans from forward bias toward short-circuit compared with defect EQE due to the 1.34 eV transition. Higher defect density is associated with reduced V_{oc} , J_{sc} , and PCE for slow scans. The impact of the defects is ameliorated in -360 mV / s sweeps.

spectra aligned in this way for Vapor 1 and Dip 1 are shown in Figures 51 and 52, respectively. For Dip 1 and Vapor 1 the resulting minority carrier collection efficiencies were between 20–40%. These values are higher than the *total* minority carrier collection implied by low steady-state J_{sc} values, suggesting more recombination is occurring outside the depletion region. For the other samples the defect band in TPC was not observed so no estimate can be made of the minority carrier collection from within the depletion region.

The correlation with the degree of hysteresis indicates that the observed defects play a role in hysteresis as well. There are a couple of ways that defects could create the hysteresis observed in these and other perovskite solar cells. Let us consider two

ways: one would be if the ions or vacancies associated with defects themselves are charged and mobile; another would be immobile defects that serve as recombination centers, but are temporarily passivated when filled with minority carriers following application of forward bias.

First I will consider mobile ions, e.g. ionized interstitial iodide atoms, I_i , with charge $-e$. In this scenario, an applied bias causes these charges to re-distribute in the absorber. Assuming that the ions cannot migrate out of the perovskite layer they will accumulate at the interfaces to some extent and arrange themselves in a way that screens the applied voltage. For instance, following an applied forward bias, negatively charged mobile ions would accumulate at the solar cell's hole collecting layer. Upon a return to biases closer to short-circuit these ions would enhance the solar cell's built-in potential, thus enhancing the separation of electrons and holes and drawing holes towards the hole collecting layer until the ions find their new equilibrium. If significant recombination centers are present in the bulk of the absorber this improved charge separation would result in higher J_{SC} and V_{OC} . Pre-biasing at voltages greater than the built-in voltage would then temporarily enhance performance, while pre-biasing at lower biases would temporarily hinder them.

Transient defect passivation would result in hysteresis if, following the application of forward bias traps are occupied and thus passivated by trapped charge carriers, temporarily increasing minority carrier mobility. In this scenario, device performance would improve until the trapped carriers escape and the traps recover their steady-state occupation. This explanation is a little more dubious because typical emission from traps occurs much more quickly than the transient performance enhancements observed in these perovskite cells decay [35].

A thorough accounting of the traps and recombination centers in these perovskite cells along with their capture and emission rates at room temperature would be needed to completely eliminate the possibility that trapping and passivation alone account for the hysteresis. However, when others have addressed this question by modeling rate-dependent hysteresis in current-voltage sweeps they are best able to replicate our results and those of Tress et. al. [34] by including trap-assisted recombination with typical emission and capture rates and mobile ions that are largely confined to the perovskite layer [35]. Our finding that the magnitude of sub-bandgap absorption typical of point defects negatively correlates with steady-state performance and positively correlates with the magnitude of enhancement during fast sweeps following pre-bias at V_{OC} lends credence to this picture. The defect energies observed in this study could be used to inform modeling efforts by restricting the choice of reasonable values for capture and emission rates used in modeling.

Comparison with results of DFT studies finds reasonable agreement for the higher energy defect with predicted transition energies for a number of defects [76]. One of these matches, a lead vacancy, V_{Pb} , has a relatively low formation energy and is predicted to migrate across the device on timescales that would impact our $J-V$ measurements [77]. Furthermore, its presence should be more strongly favored in a lead-poor, iodine-rich, material that would also favor the formation of iodine-on-methylammonium, I_{MA} , and iodine-on-lead, I_{Pb} , anti-site defects, which are reasonably good matches for the 0.76 eV defect. That said, DFT simulations vary widely on defect transition and band gap energies predicted for $CH_3NH_3PbI_3$ [78]. Studies varying stoichiometry of $CH_3NH_3PbI_3$ thin films in PSCs and then measuring relative defect densities would provide a useful check on simulations and help identify

the chemical origins of defects. Finally, I cannot exclude the possibility of extrinsic defects, nor is it clear that the 0.76 eV defect is due to a defect in the $\text{CH}_3\text{NH}_3\text{PbI}_3$.

Summary

To summarize, I have observed a correlation between quasi-steady-state performance parameters V_{oc} , J_{sc} , and PCE with the defect EQE at 1.34 eV that varies over an order of magnitude across a set of five planar perovskite solar cells. I also find larger hysteresis for fast J - V measurements in the more defective cells. Collectively, the EQE and TPC spectra are best fit by a pair of defects with varying densities. The appearance of the 1.34 eV defect in TPC locates its source in the perovskite absorber. Together, the data suggest this defect, or a deeper one correlated with it, in the perovskite absorber limits steady-state performance of the solar cell and perhaps plays a role in hysteresis. Prior work implicating defects in performance limitations and hysteresis [34, 35, 73, 79] by modeling J - V curves is thus supported by this work which directly observes elevated defect densities in cells with relatively poor steady-state performance and pronounced hysteresis. The energy of defect transition is consistent with DFT simulations for V_{Pb} which also predict it is mobile on timescales consistent with observed hysteresis [76, 77]. This suggests a path toward improved performance of planar PSCs by controlling the formation of V_{Pb} defects. Finally, I have established that EQE and TPC are sensitive enough to detect these defects in working PSCs and may be used to enhance understanding of perovskite formation, aging and stability.

In this chapter, I have established a connection between defects in $\text{CH}_3\text{NH}_3\text{PbI}_3$ thin-films and performance characteristics of perovskite solar cells utilizing this absorber. Having established this connection some attempt should be made to

understand what might affect the defect density and energy. In the next chapter, I will examine the evolution of the defect density as the perovskite ages in moderately humid air. Furthermore, we will see how alloying $\text{CH}_3\text{NH}_3\text{PbI}_3$ with bromine to form $\text{CH}_3\text{NH}_3\text{Pb}(\text{I}_{1-x}\text{Br}_x)_3$ changes the observed defect transition energies and whether this alloying impacts the evolution of the defect structure.

CHAPTER V

DEFECTS AND DISORDER IN $\text{CH}_3\text{NH}_3\text{Pb}(\text{I}_{1-x}\text{Br}_x)_3$

Portions of this chapter were taken from C.M. Sutter-Fella, D.W. Miller, Quynh P. Ngo, Ellis T. Roe, Francesca M. Toma, Ian D. Sharp, Mark C. Lonergan, and Ali Javey “Band Tailing and Deep Defect States in $\text{CH}_3\text{NH}_3\text{Pb}(\text{I}_{1-x}\text{Br}_x)_3$ Perovskites as Revealed by Sub-Bandgap Photocurrent”, ACS Energy Letters published February 15, 2017. It was written with equal contributions by myself and C. M. Sutter Fella with editorial assistance of our co-authors. Data for this paper were collected by myself and with corroborating data using complementary techniques from C.M. Sutter-Fella. The solar cells used were fabricated by C.M. Sutter-Fella and as such the description of fabrication has only been lightly edited by D.W. Miller.

Introduction

In the previous chapter, I described an experiment which characterized the sub-bandgap density of states in $\text{CH}_3\text{NH}_3\text{PbI}_3$ perovskite solar cells (PSCs), revealing defect states correlated with steady-state performance and J - V hysteresis of PSCs and strengthening the case that hysteresis is due to mobile ions. In this chapter, I will expand the range of characterized materials to include wider bandgap perovskites alloyed with bromine to form $\text{CH}_3\text{NH}_3\text{Pb}(\text{I}_{1-x}\text{Br}_x)_3$ and observe how long term exposure to moderately humid air affects the material properties.

As mentioned earlier in this work, organometal lead-halide perovskites with the general formula ABX_3 have generated a lot of interest over the last 8 years as their solar cell power conversion efficiencies have increased from 3.8% in 2009 [17] to the current world record of 22.1 % [6]. Much of this progress has been attributed

to composition engineering: at the A site with $\text{CH}(\text{NH}_2)_2^+$, CH_3NH_3^+ , and Cs^+ cations [80]; at the B site with Pb_2^+ and Sn_2^+ cations [81]; and at the X site with I^- , Br^- , and Cl^- anions [64, 82]. These changes have allowed researchers to increase photovoltaic power conversion efficiency and stability of PSCs, and to engineer the band gap (E_g) for use in high efficiency tandem photovoltaic devices. Despite the intense interest in composition engineering, the effects of alloying on structural disorder and the densities of states (DOS), particularly within the bandgap, are not well documented. Their characterization is of central importance to identifying factors that contribute to efficiency loss and instability for a number of reasons. First, defects mediate non-radiative recombination and modify the band alignment [83]. Second, there is a growing consensus that current-voltage hysteresis and photocurrent transients in organometal perovskite solar cells are due to defect states and related mobile ionic species [33, 83, 84]. Third, alloying might be expected to increase disorder in a crystal as the variety of possible defect states is increased. Importantly, the optical band edge, characterized by the Urbach energy (E_u) [85], can be broadened by disorder and defects in the crystal lattice [39–41] and thus provide a measure of how alloying affects crystal order. Finally, the evolution of defect states and structural disorder with age could provide insights into various phenomena associated with degradation.

Probing the role of defects and disorder on optoelectronic properties requires sensitive spectroscopic probes. Defect transitions typically have much longer absorption lengths than interband transitions therefore requiring the analysis of optical absorption over several orders of magnitude below that at E_g . To this end, photothermal deflection spectroscopy (PDS) has been performed on isolated thin films [62, 64], and Fourier transform photocurrent spectroscopy (FTPS), sub-bandgap

external quantum efficiency (EQE), transient photocapacitance (TPC), and transient photocurrent measurements have been applied to full photovoltaic devices [54, 62, 84].

For $\text{CH}_3\text{NH}_3\text{PbI}_3$ films, previous PDS and FTPS measurements have shown regimes of exponential absorptance behavior with steep slopes that correspond to low values of E_u (~ 15 meV) and without the signatures of deep states within the band gap for up to four orders of magnitude of response below E_g [62]. Similarly, $E_u \simeq 25$ meV in $\text{CH}_3\text{NH}_3\text{PbBr}_3$ films has been measured using PDS [64] and in devices $E_u \simeq 14$ meV using a combination of photocurrent spectroscopy and PDS [86]. Values on mixed bromide/iodide alloys $\text{CH}_3\text{NH}_3\text{Pb}(\text{I}_{1-x}\text{Br}_x)_3$ have been more varied. Sadhanala et al. observed higher values of E_u at intermediate x with a peak of 90 meV for $x = 0.8$ [64]. In contrast, Hoke et al. observed low values of E_u in the range 12–17 meV over nearly the full range of x , with an outlier at $x = 0.5$ [86].

Although the methods described above have been successful at characterizing E_u in $\text{CH}_3\text{NH}_3\text{Pb}(\text{I}_{1-x}\text{Br}_x)_3$ materials and solar cells, the signatures of electronically-active defect states residing deep in the gap are rarely observed. In this regard, achieving higher sensitivity in sub-bandgap EQE would help to probe sub-bandgap absorption that can be several orders of magnitude weaker than absorption at E_g . High sensitivity is enabled by using a high throughput monochromator, a low-noise current pre-amplifier, and careful filtering of above bandgap stray light, allowing investigation of the sub-bandgap DOS. The apparatus used in this case is described in Chapter III. As described in Chapter IV and elsewhere [84], a combination of high-sensitivity sub-bandgap EQE and TPC were recently used to reveal a defect band at 1.34 eV with varying density that was linked to photovoltaic characteristics in $\text{CH}_3\text{NH}_3\text{PbI}_3$ solar cells.

Here, I present sub-bandgap EQE measurements of Au / spiro-OMeTAD / $\text{CH}_3\text{NH}_3\text{Pb}(\text{I}_{1-x}\text{Br}_x)_3$ / TiO_2 / FTO / glass photovoltaic devices at room temperature and extending over the full halide composition space ($0 \leq x \leq 1$). In addition, I assess the impact of long-term aging of devices under atmospheric conditions, as monitored via formation of PbI_2 , on photoluminescence quantum yields and Urbach energies. Samples were aged for up to 2300 hours in a laboratory environment in which temperature ranged from 21–23 °C and relative humidity ranged from 43–57%. For all compositions, I find Urbach energies in the range of 15–23 meV that remain approximately constant throughout the experiment. Moreover, I find direct evidence of sub-bandgap electronic states within the perovskite light absorbers. For pure $\text{CH}_3\text{NH}_3\text{PbI}_3$ a single, relatively shallow state is observed. With increasing Br content, this state moves closer to mid-gap while another defect is revealed. If the densities of the defect state nearest mid-gap cannot be controlled, then they will likely enhance Shockley-Read-Hall recombination in higher bandgap perovskites and potentially limit device performance. Our results provide important insight into the defect characteristics of the explored perovskite compositions, with implications for understanding disorder and defect induced performance limits.

Sample Fabrication

$\text{CH}_3\text{NH}_3\text{Pb}(\text{I}_{1-x}\text{Br}_x)_3$ preparation

$\text{CH}_3\text{NH}_3\text{Pb}(\text{I}_{1-x}\text{Br}_x)_3$ thin films with controlled Br concentration were synthesized by a two-step low pressure vapor-assisted solution process (LP-VASP) that is adapted from previous reports [87, 88]. Previous vapor assisted methods enabled uniform planar thin film based cells but processing conditions were limited

by the low vapor pressure of $\text{CH}_3\text{NH}_3\text{I}$ [89]. Lowering the overall pressure allowed exploration of a larger range of processing conditions.

First, the mixed lead halide precursor, comprising 0.8 M PbI_2 (Alfa Aesar, 99.9985%) and 0.2 M PbBr_2 (Sigma-Aldrich, 99.999%) dissolved in N,N-dimethylformamide (Sigma-Aldrich, 99.9%) and filtered with a 0.45 μm syringe filter, was spin-coated onto the FTO/ TiO_2 coated glass substrate and dried at 100 °C for 15 min in N_2 atmosphere. Spin coating of the mixed lead halide film was conducted in air at 500 rpm for 5 s, followed by 2000 rpm for 3 minutes. Second, the precursor film was annealed in a test tube with a mixture of $\text{CH}_3\text{NH}_3\text{I}$ and $\text{CH}_3\text{NH}_3\text{Br}$ totaling 0.1 g at 120 °C for 2 hours at a pressure of ~ 0.4 Torr. The Br content is tuned by the ratio of $\text{CH}_3\text{NH}_3\text{Br}$ to $\text{CH}_3\text{NH}_3\text{I}$. After conversion of the $\text{PbI}_2/\text{PbBr}_2$ precursor to $\text{CH}_3\text{NH}_3\text{Pb}(\text{I}_{1-x}\text{Br}_x)_3$ the sample was rinsed in isopropyl alcohol and dried with N_2 before the hole selective contact layer was deposited by spin-coating.

Device Completion

As show in Figure 19, the structure of the perovskite solar cells (PSCs) used in this study was: Au / spiro-MeOTAD / $\text{CH}_3\text{NH}_3\text{Pb}(\text{I}_{1-x}\text{Br}_x)_3$ / TiO_2 / FTO / glass.

As a reminder, spiro-OMeTAD refers to the optically transparent hole conductor 2,2',7,7'-tetrakis-(N,N-di-p-methoxyphenylamine)9,9'-spirobifluorene. The spiro-OMeTAD used in this study was purchased from Luminescence Technology Corporation. Commercially available FTO patterned glass substrates with a sheet resistance of (7–10 Ω/\square) were used, following cleaning with soap and water, deionized water, acetone, and isopropyl alcohol. The electron selective contact was a layer of compact, as opposed to mesoporous, TiO_2 . A 100 nm TiO_2 layer was deposited on

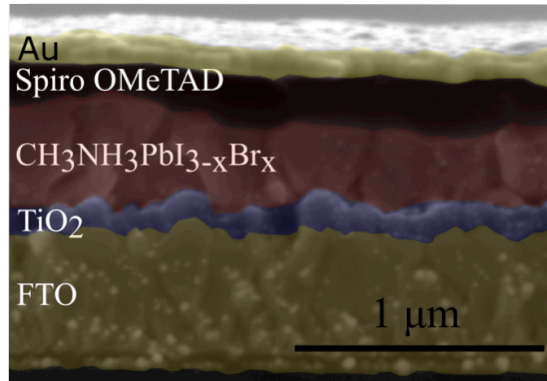


FIGURE 19. Shown above is a false colored cross-sectional scanning electron microscopy (SEM) image of a typical Au/spiro-MeOTAD/ $\text{CH}_3\text{NH}_3\text{Pb}(\text{I}_{1-x}\text{Br}_x)_3$ / TiO_2 /FTO/glass solar cell fabricated for this study. Image credit to Carolin Sutter-Fella [90].

the FTO glass substrate by electron beam evaporation (Angstrom NEXDEP 006) at a base pressure of $\sim 7 \times 10^{-6}$ Torr and a substrate temperature of 350°C .

The precursor for the hole selective contact required a few steps. Firstly, 520 mg of the dopant lithium- bis(trifluoromethanesulfonyl)imide (Li-TFSI, Sigma-Aldrich, 99.95%) was dissolved in 1 ml acetonitrile. Then 17.5 microliter of that mixture, 80 mg spiro-OMeTAD (Lumtec, 99.5%) and 28.5 microliter of 4-tert-butylpyridine (Sigma-Aldrich, 96%) were mixed in 1 milliliter of chlorobenzene (Sigma-Aldrich, 99.8%). This mixture is spin-coated onto the perovskite layer in air at 500 rpm for 5 s, followed by 3000 rpm for 30 s. The film was dried in a desiccator overnight before the Au contact was deposited through a shadow mask in an electron beam evaporator. The overlap of the Au contact with the FTO defines the active cell area of 0.062 cm^2 .

Samples Studied

All of the samples used in this study were prepared using the above described method with the only intentional variation between them being the Br content, x in $\text{CH}_3\text{NH}_3\text{Pb}(\text{I}_{1-x}\text{Br}_x)_3$. The Br content of the samples was measured using energy

dispersive x-ray spectroscopy (EDX). EDX was measured using a 7 kV, FEI Quanta FEG 250. For $x \lesssim 0.2$, the perovskite crystal is tetragonal. It is cubic otherwise, and the tetragonal (110) plane is equivalent to the (100) cubic plane. I can thus track the change in the lattice constant by tracking the change in the angle of the (100) (or (110)) peak angle. Figure 20 shows the variation of the lattice constant with x . The roughly linear decrease in lattice parameter with increasing x indicates that the smaller bromine anion is taking the place of iodine in the perovskite crystal lattice and covers the range of lattice constants spanned by similar studies [64, 86].

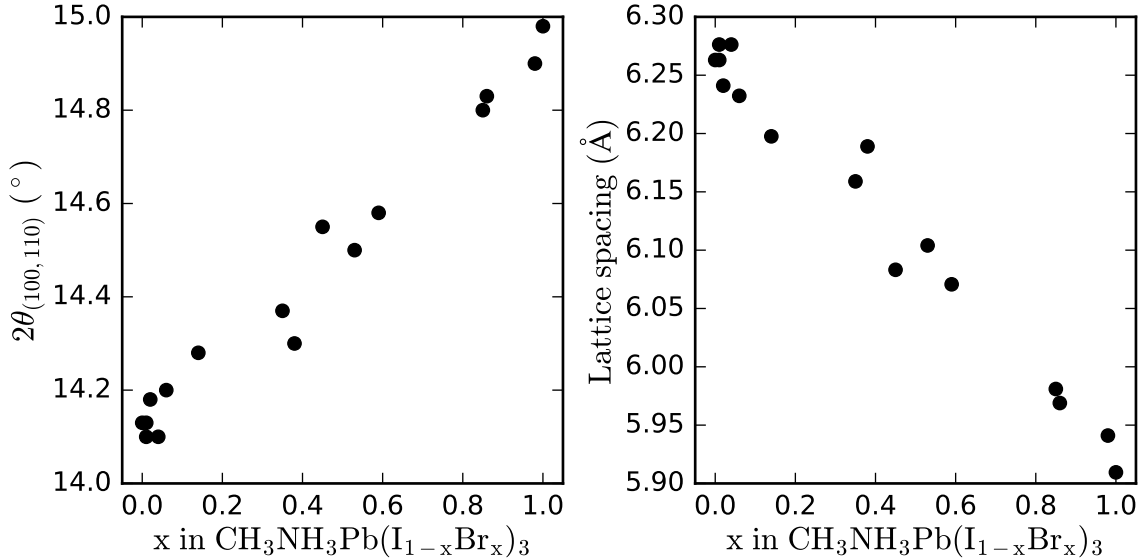


FIGURE 20. Left pane: Change in the (100) peak angle is plotted versus $x \equiv \text{Br}/(\text{Br}+\text{I})$; for $x \lesssim 0.2$ the perovskite is tetragonal and the (110) plane is equivalent to the cubic (100). Right pane: Change in the lattice constant with x .

Fifteen samples in all were created and five of those fifteen were investigated in detail at the University of Oregon as they aged for up to 2400 hours in air. These samples spanned the full range from $x = 0$ to $x = 1$ with $x = 0, 0.4, 0.6, 0.9$ and 1.0 where x defines the Br content in the $\text{CH}_3\text{NH}_3\text{Pb}(\text{I}_{1-x}\text{Br}_x)_3$ films. For this reason, I will refer to the different samples simply by their Br content. All these devices

had relatively low power conversion efficiencies and could not be easily compared to each other using performance metrics due to the wide variation in band gap energy without corresponding variation and optimization of the hole and electron transport layers. Instead, this study focuses on absorber properties. While some techniques used depend on the absorber being in a working solar cell, it need not be a particularly good one.

Effects of Bromine Alloying on Sub-Bandgap EQE

The sub-bandgap EQE was measured using the apparatus described in Chapter III. Long-pass filters were used to limit above bandgap stray light from a scanning monochromator to one part in 10^7 throughout most of the spectral range. Given reports of light-induced halide segregation in $\text{CH}_3\text{NH}_3\text{Pb}(\text{I}_{1-x}\text{Br}_x)_3$ films forming iodine and bromine rich regions[86, 91] it is important to note that the intensity of the monochromatic light, above the band gap of the samples investigated was less than 0.04 mW/cm^2 . The light intensity varied over the spectral measurement and was below 0.4 mW/cm^2 at 0.8 eV, 0.04 mW/cm^2 at 1.6 eV, and 0.01 mW/cm^2 at 2.3 eV. This is much lower than the $10\text{--}100 \text{ mW/cm}^2$ used in the studies in which varying degrees of halide segregation were observed[86, 88, 91]. The proposed mechanisms for halide-segregation are predicated on the generation of mobile charges, thus low above-gap irradiance should limit halide segregation during the measurement. Furthermore, halide segregation in these alloys is reported to fully reverse after a few minutes in the dark[86]. Because the EQE measurements reported here are performed at least 5 minutes after exposure to above-bandgap light more intense than that used for the measurement itself and the sub-bandgap portion is recorded several minutes to hours after any exposure to above-bandgap light, halide segregation during the

measurement should be quite limited. However, it is important to consider that halide segregation has not been well characterized. For instance, the activation energies for halide migration have not been identified. Halide ion mobilities may, for example, depend on the density of halide vacancy defects. Therefore, light-induced halide segregation in mixed I/Br samples cannot be fully discounted and may contribute to sub-bandgap absorption. However, transitions below the bandgap of $\text{CH}_3\text{NH}_3\text{PbI}_3$ (1.58 eV) or those observed in the $x = 0$ and $x = 1$ samples cannot be explained by the formation of iodine-rich domains.

Representative sub-bandgap EQE spectra of $\text{CH}_3\text{NH}_3\text{Pb}(\text{I}_{1-x}\text{Br}_x)_3$ devices ($x = 0, 0.4, 0.6, 0.9$ and 1.0) are shown in Figure 21. There are three main observations of note in these spectra. Firstly, they show that by changing x , the $\text{CH}_3\text{NH}_3\text{Pb}(\text{I}_{1-x}\text{Br}_x)_3$ the band gap is tuned over the range from 1.58–2.3 eV. Secondly, the Urbach energy varies from 15–23 eV and is not strictly increasing with bandgap. Lastly, they reveal photocurrent due to optical transitions in the bandgap that likely involve point defects within the perovskite thin films. The latter two observations have performance implications for devices utilizing these materials and we should examine them in more detail.

Effect of Br Alloying on the Urbach Energy

As noted in Chapter II, the Urbach energy (E_u) is a measure of the disorder in a material with its origins in the deviation of atoms from their lattice positions, whether that is due to thermal fluctuations or frozen-in disorder[39–41, 85]. The Urbach energies extracted from EQE and photoluminescence versus bandgap are provided in Figure 22. Bandgaps were determined from EQE using Tauc plots [74], resulting in values in the expected range of 1.58 to 2.3 eV. Further detail on extracting band gaps

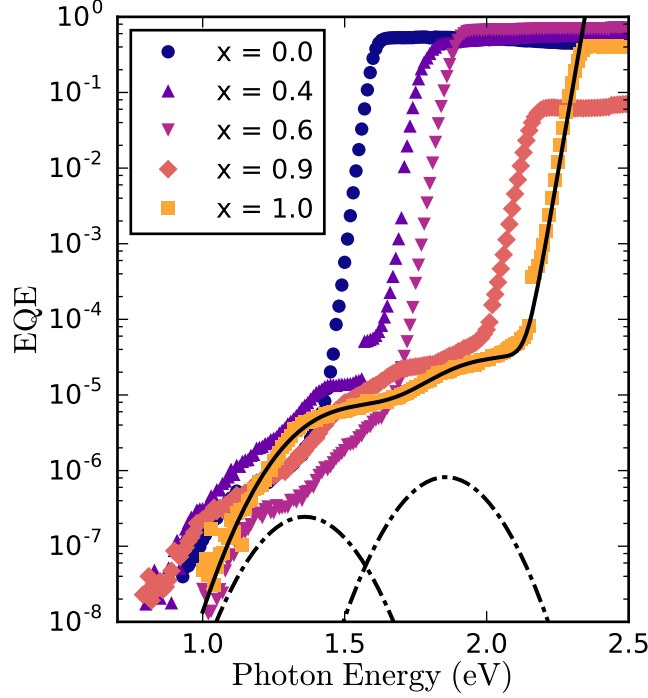


FIGURE 21. Sub-bandgap EQE spectra of $\text{CH}_3\text{NH}_3\text{Pb}(\text{I}_{1-x}\text{Br}_x)_3$ PSCs with bromine content spanning the full composition space. E_u is consistently in the range from 15–23 eV and point defects are observed that are close to mid-gap for the high Br devices. The solid line indicates the line of best fit to the $x = 1.0$ spectrum while the dash-dotted lines illustrate the Gaussian density of states for the pair of point defects used to fit the $x = 1.0$ defect band.

from EQE is given in Appendix 7.2. Urbach energies of LP-VASP samples grown on glass substrates were extracted from PL spectra using the van Roosbroeck-Shockley equation, where the optical emission rate is related to the absorption coefficient [92].

All of the EQE spectra for the $\text{CH}_3\text{NH}_3\text{Pb}(\text{I}_{1-x}\text{Br}_x)_3$ PSCs examined in this study display sharp absorption edges below E_g that translate into low Urbach energies (15–23 meV) and are in excellent agreement with those obtained from PL spectra (13–19 meV). One can argue that this alone indicates that $\text{CH}_3\text{NH}_3\text{Pb}(\text{I}_{1-x}\text{Br}_x)_3$ is very promising for photovoltaic applications by considering a brief survey of Urbach energies and the best achieved performance of other non-crystalline thin film based solar cells. In photovoltaic cells utilizing $\text{Cu}_2\text{ZnSn}(\text{Se}_y\text{S}_{1-y})_4$ absorbers, high Urbach

energies were correlated with high voltage deficits defined as $E_g - qV_{oc}$ [42]. A similar correlation was found in the I-III-VI₂ chalcopyrites, $\text{CuIn}_{1-x}\text{Ga}_x(\text{Se}_{1-y}\text{S}_y)_2$ [93]. It was later shown that high Urbach energies in $\text{Cu}_2\text{ZnSn}(\text{Se}_y\text{S}_{1-y})_4$ and $\text{CuIn}_{1-x}\text{Ga}_x\text{Se}_2$ were also associated with photoluminescence emission peaks farther below E_g and voltage deficits in a large number of samples [43]. Indeed, considering the available data in aggregate demonstrates this correlation across materials [62]. This suggests that high Urbach energies may universally provide a mechanism for limiting V_{oc} and therefore low E_u is universally desirable for solar cell absorbers.

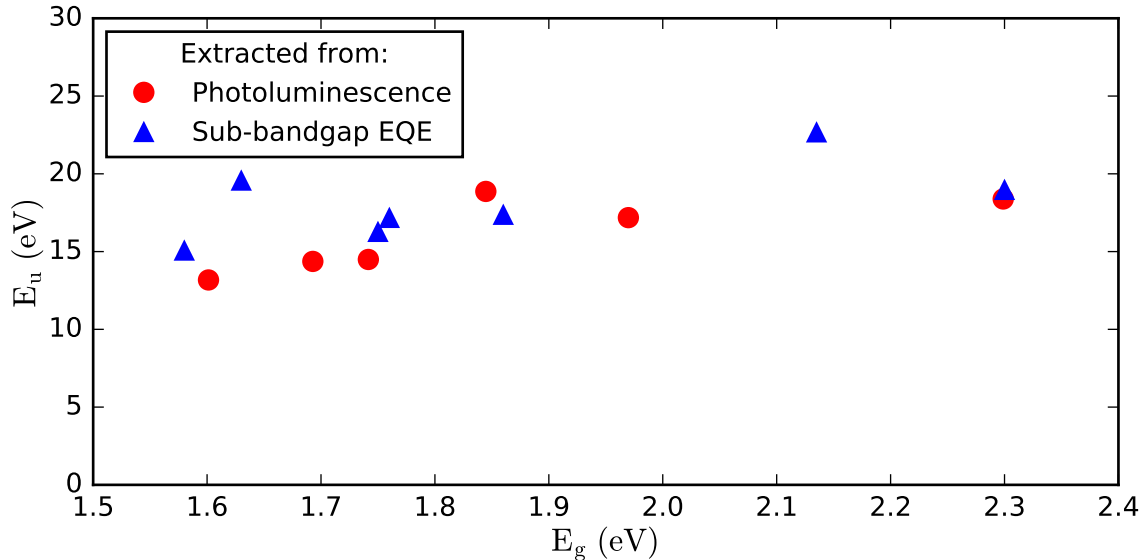


FIGURE 22. Summary of Urbach energies extracted from EQE and PL measurements plotted against the bandgap. The investigated $\text{CH}_3\text{NH}_3\text{Pb}(\text{I}_{1-x}\text{Br}_x)_3$ films show consistently low Urbach energies between in the range 15–23 eV over the full bandgap range of $1.58 \leq E_g \leq 2.3$ eV.

With that in mind, it is interesting to compare Urbach energies of $\text{CH}_3\text{NH}_3\text{Pb}(\text{I}_{1-x}\text{Br}_x)_3$ films to a range of technologically important inorganic semiconductors used in photovoltaic and other optoelectronic applications. The Urbach energies obtained in this study from fitting sub-bandgap EQE data are plotted against their optical bandgaps, together with available literature values,

in Figure 23. The bandgap range accessible with $\text{CH}_3\text{NH}_3\text{Pb}(\text{I}_{1-x}\text{Br}_x)_3$, 1.58–2.32 eV, is highlighted. We see that LP-VASP grown $\text{CH}_3\text{NH}_3\text{Pb}(\text{I}_{1-x}\text{Br}_x)_3$ achieves near constant Urbach energies that are significantly lower than in conventional semiconductors, especially for $E_g > 1.9$ eV. These values are comparable to the best achieved by other poly-crystalline thin films and are the first such thin films to achieve Urbach energies under 50 meV for $E_g > 1.9$ eV. This is especially remarkable given the nature of the synthesis process, which does not exceed 120 °C and is performed on non-lattice matched substrates. While the $\text{Cu}_2\text{ZnSn}(\text{S}_x\text{Se}_{1-x})_4$, $\text{CuIn}_{1-x}\text{Ga}_x(\text{Se}_{1-y}\text{S}_y)_2$, CdTe and InP poly-crystalline thin films all achieve comparable E_u values they each require at least one processing step at a temperature over 400 °C to do so. Furthermore, the available literature data for Urbach energies in $\text{CH}_3\text{NH}_3\text{Pb}(\text{I}_{1-x}\text{Br}_x)_3$ yielded significantly higher E_u than reported here for some of the mixed I/Br compositions (compare blue triangles in Figure 23) [64, 86]. This suggests the synthesis method could play a role in defining disorder, particularly in compositionally complex mixed halide perovskites.

As discussed in the previous chapter, the ease with which such a low Urbach energy is achieved may thus help to explain the relatively quick improvement of perovskite solar cell efficiencies. The fact that this ease is replicated across the material system with such a broad range of accessible bandgaps makes $\text{CH}_3\text{NH}_3\text{Pb}(\text{I}_{1-x}\text{Br}_x)_3$ perovskites promising candidates for a wide variety of tandem solar cells using crystalline silicon, cheaper polycrystalline silicon, CuInSe_2 or even perovskite-perovskite tandem solar cells [94]. Such efforts are already underway, and in some cases experimentation has already begun alloying the cation or the metal in addition to the halogen [81, 95]. That being said, while a low Urbach energy does appear to be necessary for the highest performing solar cells, it is not sufficient. States

deep in the band gap can be even more detrimental to performance than those at the band edges and we should consider the signatures of such states in our cells.

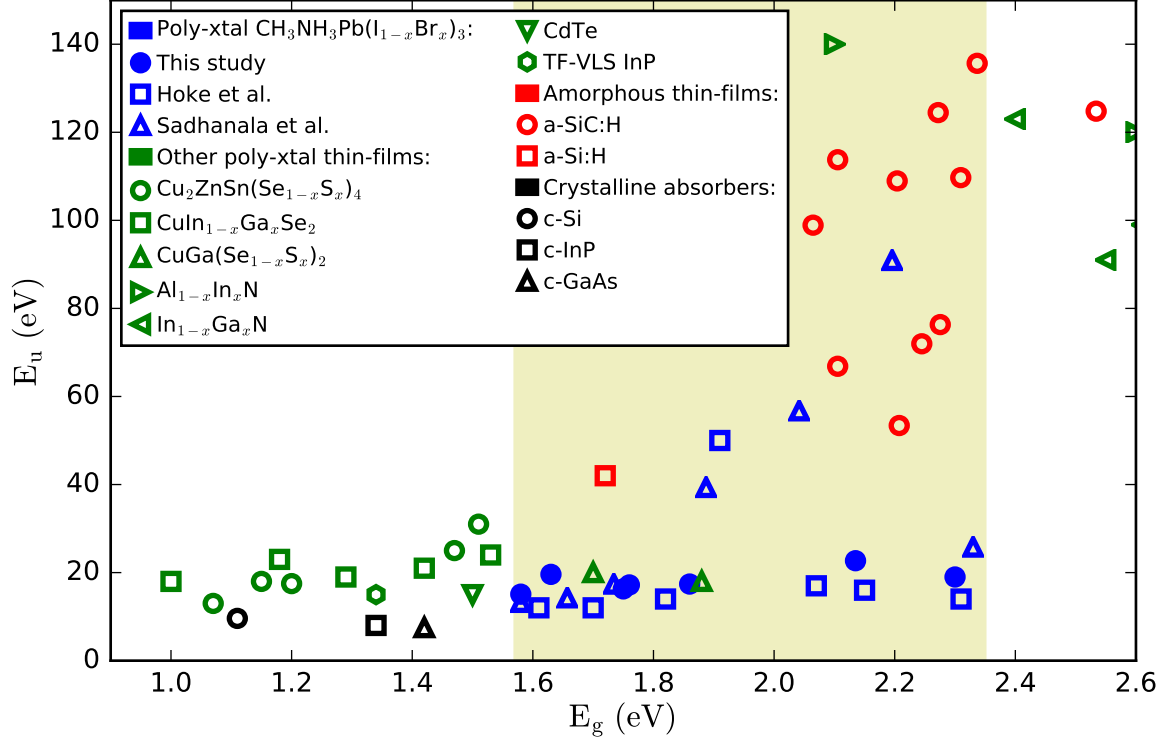


FIGURE 23. Urbach energies versus bandgap with the range accessible by $\text{CH}_3\text{NH}_3\text{Pb}(\text{I}_{1-x}\text{Br}_x)_3$ perovskites highlighted in the shaded region. Urbach energies from $\text{CH}_3\text{NH}_3\text{Pb}(\text{I}_{1-x}\text{Br}_x)_3$ perovskites in this study are shown as solid blue circles. $\text{CH}_3\text{NH}_3\text{Pb}(\text{I}_{1-x}\text{Br}_x)_3$ from other studies [64, 86] are hollow blue squares and triangles. Also shown are a range of technologically important semiconductors. Poly-crystalline data shown in green are sourced as follows: $\text{Cu}_2\text{ZnSn}(\text{S}_x\text{Se}_{1-x})_4$ [42]; $\text{CuIn}_{1-x}\text{Ga}_x\text{Se}_2$ [47]; TF-VLS InP [54]; CdTe [52]; $\text{CuGa}(\text{Se}_{1-x}\text{S}_x)_2$ [93]; $\text{Al}_{1-x}\text{In}_x\text{N}$ [96]; $\text{In}_{1-x}\text{Ga}_x\text{N}$ (In-rich, graded In profile) [97]. Data for crystalline materials shown in black are sourced as follows: c-Si [39]; c-InP [98]; c-GaAs [40]. Data for amorphous thin films shown in red are sourced as follows: a-Si [39]; a-SiC:H [99].

Effect of Br Alloying on Point Defects

As motivated in Chapter III and established in Chapter IV, sub-bandgap defect-related transitions in the EQE spectra (EQE_d) were fit using a function of the form:

$$EQE_d(E) \propto 1 + \operatorname{erf}\left(\frac{E - E_d}{\sigma_d\sqrt{2}}\right), \quad (5.1)$$

where E_d is the optical transition energy of the defect, E is the incident photon energy, and σ_d is the standard deviation of the underlying Gaussian energy density of states associated with a point defect. An example of a fit to these spectra is shown in Figure 21. For pure $\text{CH}_3\text{NH}_3\text{PbI}_3$, the best fit was obtained using a single defect model. However, with increasing Br content, the bandgap opens and a second defect-related transition emerges, requiring the use of a two-defect model to describe the response. Let us note here, that it is possible that thin film interference effects, coupled with a single deep defect, could produce a feature such as the one at ~ 1.7 eV in the defect band of the $x = 1$ device shown in Figure 21. That being said, a two defect model that allows variations in relative density of the two defects can better explain variations in the shape of the defect band over time as these cells age, so I will proceed with that model. The best fits to defects for each of the above cells are summarized in Table 2.

All defect positions given in Table 2 are the optical transition energies with respect to a band edge, though the technique does not provide information about the carrier type. While the sub-bandgap EQE corresponds to transitions from bound to free electronic states that generate a photocurrent, it does not indicate whether the observed transitions are associated with trapped holes that are excited to the valence band or trapped electrons that are excited to the conduction band. Therefore, further

TABLE 2. Result of best fits to the sub-bandgap portions EQE spectra shown in Figure 21. The last column shows the value of the EQE at midgap for each sample revealing a clear increase.

x Br/(Br+I)	E_g eV	E_u meV	E_{d1} eV	E_{d2} eV	$E_{d1} - E_g/2$ eV	EQE($E_g/2$) EQE
0.0	1.58 ± 0.01	15.3 ± 1	1.36 ± 0.06	—	0.57	4.0×10^{-8}
0.4	1.76 ± 0.01	17.1 ± 1	1.07 ± 0.06	1.43 ± 0.05	0.19	8.8×10^{-8}
0.6	1.86 ± 0.01	17.4 ± 1	1.14 ± 0.05	1.73 ± 0.05	0.20	2.7×10^{-8}
0.9	2.15 ± 0.01	21.0 ± 1	1.10 ± 0.04	1.63 ± 0.06	0.02	3.7×10^{-7}
1.0	2.30 ± 0.01	18.6 ± 1	1.42 ± 0.05	1.89 ± 0.05	0.27	4.2×10^{-7}

research will be required to identify the specific nature of these defects, as well as their energetic positions on an absolute scale relative to each band edge, as a function of composition. Regardless of the exact defect positions, the observed sub-bandgap responses suggest that the higher bandgap alloys tend to form defects closer to mid-gap. For example, the 1.36 eV defect observed in the $x = 0$ sample corresponds to a state that is 220 meV from a band edge, and 570 meV away from the midgap position. In stark contrast, the 1.42 eV transition seen in the $x = 1$ sample is positioned 880 meV away from a band edge, and only 270 meV from the middle of the bandgap. Defects closer to mid-gap are much more efficient recombination centers, even for the same defect density. While Table 2 does not show a strict trend of the lowest energetic assignment moving toward mid-gap, it should be noted that these energy assignments are probably less accurate than the estimated margin of error. Firstly because the spectra are not corrected for reflectance, and secondly because choices made in setting bounds for the non-linear fitting can change the resulting fit. However, neither of these effects would not change the overall absorption near mid-gap by large factors. The last column of the table indicates clearly that there is a trend towards higher EQE near mid-gap with increasing x . This trend holds whether or not the spectra are normalized at E_g . Therefore, so long as this portion of the EQE spectra

is due to absorption in the absorber, one would expect higher recombination rates in the higher bandgap material.

Since the exceedingly low photocurrents measured in sub-bandgap EQE could be generated in any part of the device, reference measurements were performed on spiro-OMeTAD and TiO_2 photoconductors (glass / FTO / spiro-OMeTAD / Au and glass / FTO / TiO_2 / Ti, respectively) under identical conditions to the PSCs. Figure 24 shows the EQE spectrum for the spiro-OMeTAD photoconductor.

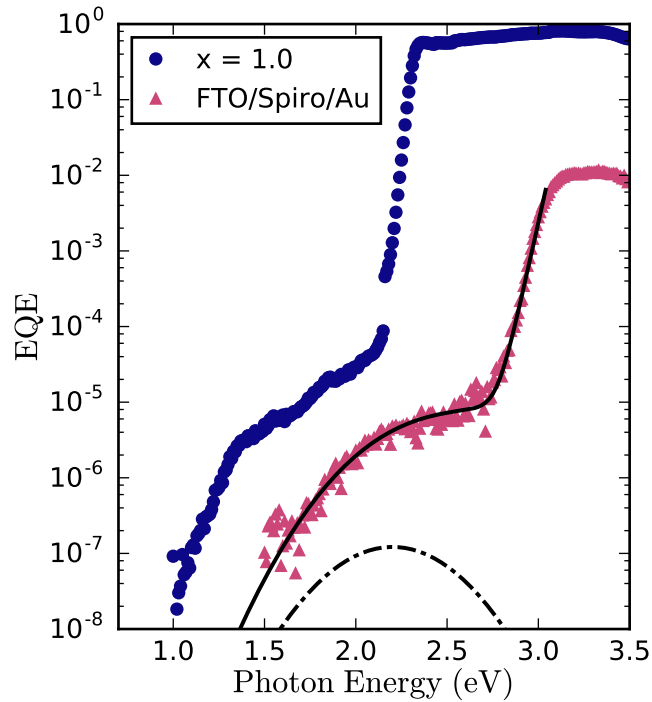


FIGURE 24. The sub-bandgap EQE of an FTO/spiro-OMeTAD/Au photoconductor is plotted with the $x = 1.0$ sample for comparison. The black line indicates a fit to the data using an exponential below 3.05 eV with an Urbach energy of 40 meV and defect-like feature centered at 2.2 eV. These features do not fully account for those seen in the perovskite solar cells.

In this case, I observed a weak sub-bandgap response centered at 2.2 eV, which is higher in energy than any defect response observed from perovskite-containing photovoltaic devices. The band-edge below 3.05 eV has a 40 meV Urbach energy,

suggesting a more amorphous structure. Both of these features roughly correspond to features seen in absorption spectra of doped spiro-OMeTAD in solution [100]. While the feature at 2.2 eV could have an impact on the sub-bandgap EQE of the PSCs with $x > 0.8$, it would only change the energy assignment of the higher energy defects. It certainly cannot account for that portion of the EQE spectra which is close to mid-gap in any of the PSCs, or for any portion of the sub-gap response in lower bandgap PSCs.

No photoresponse was observed from the glass / FTO / TiO₂ / Ti photoconductor. While the TiO₂ photoconductor should be expected to show a band-edge optical response in the ultraviolet, it appears the light source used in these EQE spectra provided insufficient intensity in this spectral range and did not produce any measurable photocurrent. This includes measurements done under a small bias. Based on these reference measurements, it is concluded that the sub-bandgap response detected from full photovoltaic device stacks is generated within the CH₃NH₃Pb(I_{1-x}Br_x)₃ absorber layers. Having investigated the full photoresponse from these perovskite free photoconductors I can now reasonably state that the sub-bandgap response seen in the perovskite solar cells is due to defects in the perovskite itself. This interpretation is even more likely given that a similar defect signature was seen in the transient photocapacitance spectra of the CH₃NH₃PbI₃ PSCs discussed in the previous chapter and published elsewhere [84].

In contrast to our finding, some previous density functional theory (DFT) studies have found that deep defects should have prohibitively high formation energies in organolead iodide perovskites[76, 101]. However, others predict a high density of deep traps under I-rich, Pb-poor, synthesis conditions due to the formation of I-on-Pb antisite (I_{Pb}) defects with a formation energy < 0.2 eV[102]. The 1.36, 1.43

and 1.42 eV transitions observed in the $x = 0, 0.4$ and 1 cells, respectively are within one standard deviation of each other and are a reasonably close match for the lead vacancy (V_{Pb}) (1-/2-) transition energy predicted as the dominant shallow defect for lead-poor $\text{CH}_3\text{NH}_3\text{PbI}_3$ [76, 101, 102]. Furthermore, this matches that of the defect identified in $\text{CH}_3\text{NH}_3\text{PbI}_3$ perovskite solar cells in the previous chapter and published elsewhere[84]. These findings are consistent with the V_{Pb} appearing at near the same energy relative to the conduction band across the samples studied. The 1.89 eV transition observed in the $x = 1$ cell is a close match for the V_{Pb} (0/-1) transition, which is predicted to be obscured by the valence band in $\text{CH}_3\text{NH}_3\text{PbI}_3$ [76]. Previous studies have indicated that alloying $\text{CH}_3\text{NH}_3\text{PbI}_3$ with Br mostly shifts the energetic position of the valence band [103, 104] suggesting that such defect states would become optoelectronically active as the bandgap opens.

Given these indications that the density of states near mid-gap is increasing with the bromine fraction, one might expect higher non-radiative recombination rates in the high bromine films. We will therefore compare our results to photoluminescence quantum yield used to examine sister $\text{CH}_3\text{NH}_3\text{Pb}(\text{I}_{1-x}\text{Br}_x)_3$ thin films deposited using the LP-VASP process.

Evaluating Non-Radiative Recombination

In a closely related experiment, a series $\text{CH}_3\text{NH}_3\text{Pb}(\text{I}_{1-x}\text{Br}_x)_3$ thin films spanning the full composition space were deposited on glass using the LP-VASP process used in this study[88]. These films were then coated in a 30 nm poly(methyl methacrylate) (PMMA) capping layer to prevent exposure to moisture that can cause the decomposition of the lead halide perovskites. The internal photoluminescence quantum yield was then evaluated for each sample as a function of illumination

intensity. This study revealed regimes limited by trap-assisted recombination for intensities below 10-100 suns, depending on the bromine content, and regimes of bi-molecular (direct electron-hole recombination) or Auger recombination at higher intensities [88]. By re-examining these data I can evaluate whether the sub-bandgap defects observed in this study might have an impact on recombination rates in LP-VASP grown $\text{CH}_3\text{NH}_3\text{Pb}(\text{I}_{1-x}\text{Br}_x)_3$ thin films. Figure 25 shows the internal photoluminescence quantum yield for a series of LP-VASP grown $\text{CH}_3\text{NH}_3\text{Pb}(\text{I}_{1-x}\text{Br}_x)_3$ thin films under 1-sun generation.

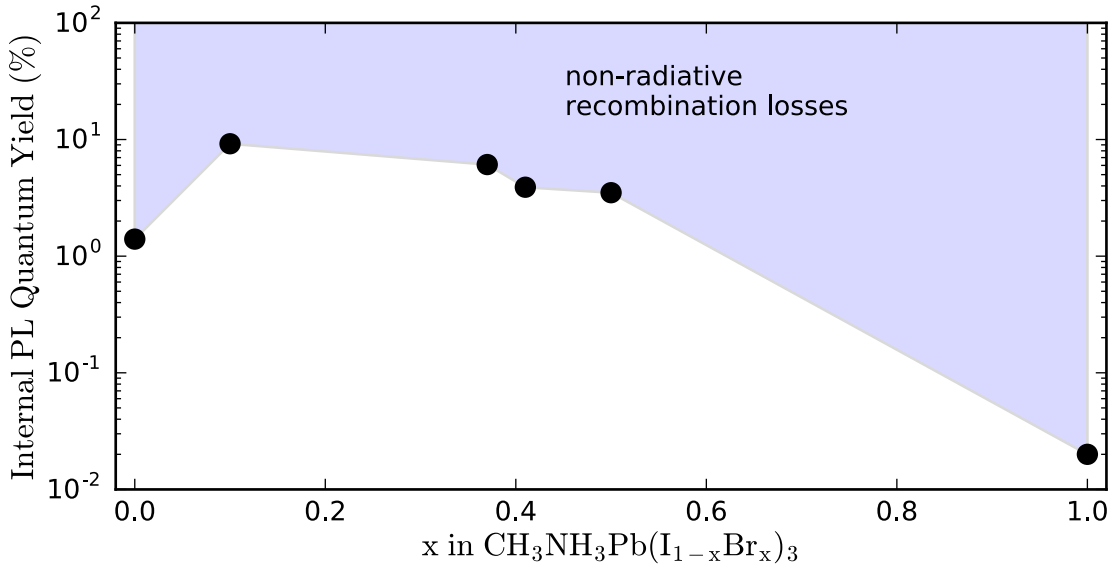


FIGURE 25. Internal photoluminescence quantum yield (PLQY) extracted at 1-sun illumination for different $\text{CH}_3\text{NH}_3\text{Pb}(\text{I}_{1-x}\text{Br}_x)_3$ compositions. The shaded area illustrates non-radiative recombination losses.

PL quantum yield measurements corroborate the sub-bandgap EQE detection of deep defects by showing that trap-assisted recombination is the limiting mechanism at 1-sun intensities, which are of relevance to the current work. PL quantum yield of 100 % would correspond to radiative recombination as the only recombination mechanism in the studied sample. PL quantum yields below 100 % are indicative of

non-radiative recombination losses. Figure 25 indicates significantly lower quantum yield in $\text{CH}_3\text{NH}_3\text{PbBr}_3$. In fact, previous analysis showed that $\text{CH}_3\text{NH}_3\text{PbBr}_3$ was limited by trap-assisted recombination up to at least 1000 suns [88]. So long as the PMMA and glass interfaces with the $\text{CH}_3\text{NH}_3\text{Pb}(\text{I}_{1-x}\text{Br}_x)_3$ have surface recombination velocities that do not strongly depend on x it is reasonable to conclude that these dependence of the PL quantum yield on x is due to changes in the sub-bandgap density of states. This would be consistent with work on the closely related material $\text{CH}_3\text{NH}_3\text{Pb}(\text{I}_{1-x}\text{Cl}_x)_3$ which was shown via time-resolved photoluminescence to be limited by defect mediated recombination at low generation rates [105]. The combination of PL quantum yield measurements indicating trap-assisted recombination at low illumination intensities in the perovskite films and sub-bandgap EQE data revealing the presence of deep defect states in the absorber layer both of which are worst for $x > 0.8$, suggests that deep defects can be expected to play an active role in affecting performance characteristics of optoelectronic devices incorporating $\text{CH}_3\text{NH}_3\text{Pb}(\text{I}_{1-x}\text{Br}_x)_3$. I will now examine how these sub-bandgap features evolve as intentional degradation of the PSCs in air proceeds.

Effects of Degradation

While it is well established that methylammonium lead halide perovskites decompose upon exposure to humid air [106], less is known about how this process impacts defects and disorder in the material. The un-encapsulated devices in this study were aged in the dark under laboratory conditions for up to 2400 hours. Aging was carried out in a dark box in a climate controlled laboratory with samples sheltered from drafts but open to the atmosphere. Humidity and temperature were monitored throughout the experiment. Temperature ranged from 21–23 °C and relative humidity

ranged from 43–57%. Decomposition of $\text{CH}_3\text{NH}_3\text{Pb}(\text{I}_{1-x}\text{Br}_x)_3$ leaves PbI_2 as a primary solid state product. Therefore, X-ray diffraction (XRD) can be used to probe changes of the film in fully assembled devices. The evolution of the (001) PbI_2 / (110) perovskite XRD integrated peak area ratio provides a useful metric for tracking decomposition as a function of time after synthesis. For the mixed bromide samples, peaks associated with PbBr_2 must be integrated along with their PbI_2 counterparts. For simplicity then, I will refer to the integration of all these XRD peaks simply as PbX_2 . Figure 26 shows a typical XRD pattern with PbI_2 (100) and $\text{CH}_3\text{NH}_3\text{Pb}(\text{I}_{0.6}\text{Br}_{0.4})_3$ (100) perovskite peaks present.

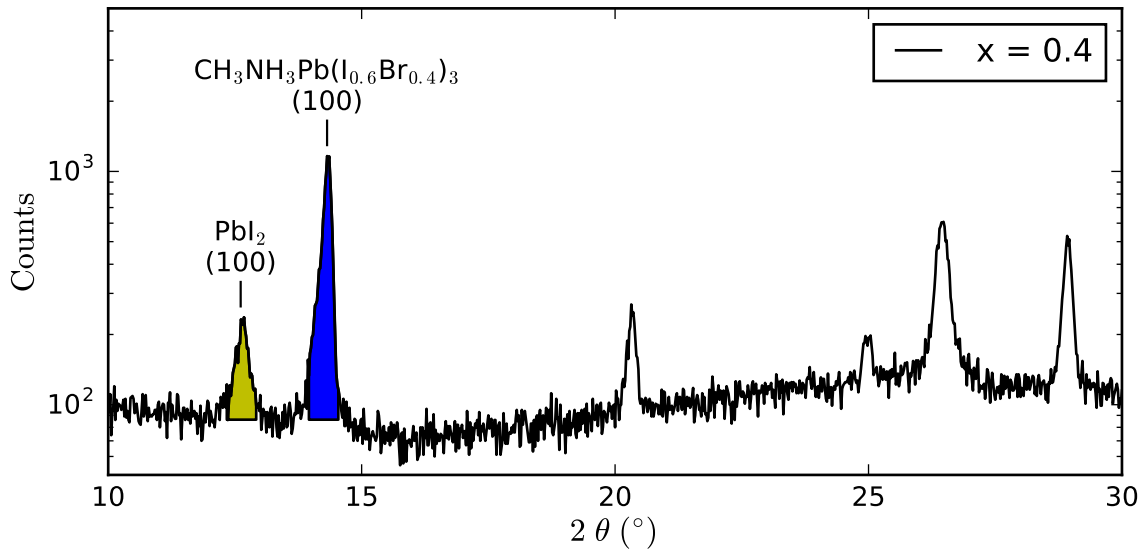


FIGURE 26. XRD pattern of $\text{CH}_3\text{NH}_3\text{Pb}(\text{I}_{0.6}\text{Br}_{0.4})_3$ thin film aged for 126 hours in air. The peaks used as a metric for aging are highlighted, no PbBr_2 peak is present.

The ratio of the PbX_2 / $\text{CH}_3\text{NH}_3\text{Pb}(\text{I}_{1-x}\text{Br}_x)$ peaks for seven samples are plotted as a function of time in the upper pane of Figure 27. A majority of the samples show some increase in PbX_2 / $\text{CH}_3\text{NH}_3\text{Pb}(\text{I}_{1-x}\text{Br}_x)_3$ although the time until a marked increase is observed varies quite a lot. Two samples, $x = 0.0$ and 1.0 , showed no distinct PbX_2 peaks at any point in the experiment. One might be tempted to

conclude that the endpoints are more stable than the mixed halide samples. But a second sample with $x = 0$, labeled $x = 0^*$ in 27 defies this trend. One could also be tempted conclude that samples in which the PbI_2 and PbBr_2 is fully converted during film formation are more stable, as those with the lowest indications of PbX_2 at the outset showed the least at the end. It is the opinion of this author that more data is needed to make a firm conclusion on these questions. Lastly, $x = 0.9$ shows a noticeable decrease in the PbX_2 peak after 300 hours. This decrease was associated with a decrease in the PbI_2 (100) peak concurrent with an increase in a few PbBr_2 diffraction peaks. As described before, the location of these peaks were included in the integration for all the mixed halide samples. That said, the XRD pattern taken at 2193 hours on the $x = 0.9$ sample was the only pattern where the PbBr_2 peaks had a significant impact. It is unclear whether this one time appearance is due to slight variations in sample positioning, sample non-uniformity, halide segregation, or some combination thereof. All of these are more likely than a reversal of the aging process.

Along with XRD patterns, I recorded the sub-bandgap EQE spectra for the aged samples and extracted the Urbach energies. The lower pane of Figure 27 displays the evolution of the Urbach energies over time for different $\text{CH}_3\text{NH}_3\text{Pb}(\text{I}_{1-x}\text{Br}_x)_3$ devices. The data points are connected for better visibility. Given that the variation hardly exceeds the uncertainty in fitting of ± 1 meV, this result indicates nearly constant Urbach energies for most samples for over 2300 h of degradation. In summation, there are two things to note: samples that started with higher PbX_2 content do not have higher Urbach energies; and the various increases and decreases in PbX_2 are in no way correlated with changes in Urbach energy. Taken together these results indicate that aging and decomposition do not significantly increase disorder and band-tail states

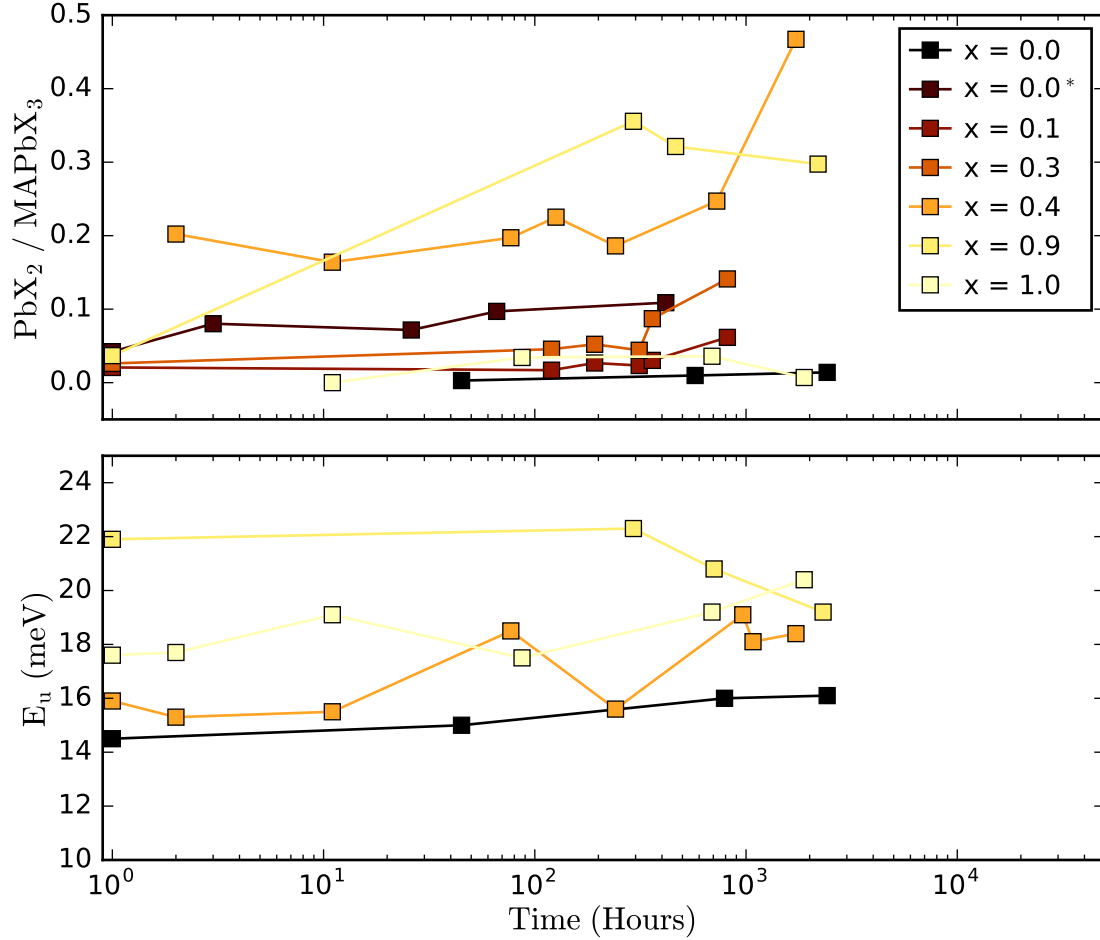


FIGURE 27. Upper pane: Evolution of PbX_2 precipitation as indicated by the relative intensity of the (110) $\text{CH}_3\text{NH}_3\text{Pb}(\text{I}_{1-x}\text{Br}_x)_3$ (or (100) for $x > 0.2$) and various PbX_2 peaks with time. Lower pane: Urbach energies measured throughout the same time period as the upper pane on the same samples.

within the remaining $\text{CH}_3\text{NH}_3\text{Pb}(\text{I}_{1-x}\text{Br}_x)_3$ as portions of it decompose into PbX_2 and $\text{CH}_3\text{NH}_3\text{X}$. Let us now consider the evolution of the deeper defect signatures.

We recorded EQE spectra well into the bandgap at many times throughout the aging process for four of the samples: $x = 0, 0.4, 0.9,$ and 1.0 . The spectra, normalized at E_g , are reproduced in Figures 28 to 31. Normalization allows comparison of the relative defect density in each sample as it ages. Normalization at E_g is permissible to the extent that the band edge density of states in the

$\text{CH}_3\text{NH}_3\text{Pb}(\text{I}_{1-x}\text{Br}_x)_3$ is independent of the defect density or crystallite size, and necessary because the overall performance of the solar cell changes as it ages. The basis for aligning EQE spectra above gap to compare relative defect densities is discussed in more detail in Chapter III.

Trends of increasing or decreasing sub-bandgap EQE in the defect band would imply a change in the sub-bandgap density of states. Again, I should note that due to the previous reports of light-induced halide segregation in $\text{CH}_3\text{NH}_3\text{Pb}(\text{I}_{1-x}\text{Br}_x)_3$ [86, 91] and well established evidence of ion migration in $\text{CH}_3\text{NH}_3\text{PbI}_3$ in response to applied voltages and photovoltage [34, 35, 84], I took care that the samples had several minutes in the dark at short circuit before beginning each of these measurement of the sub-bandgap EQE. Examination of the EQE response further below the bandgap reveals that aging does not, in general, increase concentrations of sub-bandgap defects, as shown in Figures 28 to 31.

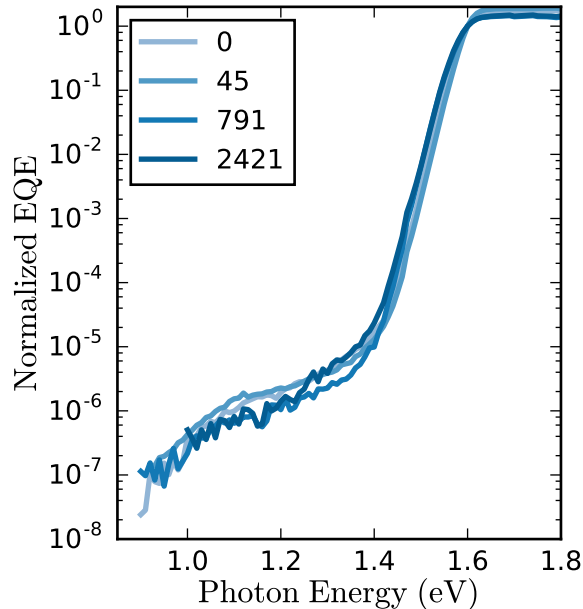


FIGURE 28. EQE spectra, normalized at E_g , for the $\text{CH}_3\text{NH}_3\text{PbI}_3$ PSC as a function of time following air exposure. The low signal region in the defect band gets noisier with age as the overall EQE degrades with time.

In fact, for the $\text{CH}_3\text{NH}_3\text{PbI}_3$ -based device shown in Figure 28, the defect-related response is nearly unaffected by aging for up to 791 hours. Keeping in mind that this same device ($x = 0$ in Figure 27) showed no measureable PbI_2 peak at any time, perhaps the relative stability of the defect signal is unsurprising. The $x = 1$ device in Figure 27 also showed no distinct PbBr_2 peak throughout the examined aging period. Let us consider the evolution of its EQE spectra, shown in Figure 29. While it is not as quite as stable as the $x = 0$ device in EQE, the movement for the $x = 1$ device is in no clear direction and limited to within a factor of 3 or so for most of the spectra. Hours 2 and 87 show larger deviations from the mean at a some optical energies. But these larger deviations also differ in functional form from the other three spectra, suggesting that perhaps they are anomalous. Such anomalies could arise from unstable electrical contact, which can have a big impact in this low-current regime.

Unlike the $x = 1$ and $x = 0$ samples, the $x = 0.9$ and $x = 0.4$ samples showed significant variation in the PbX_2 peak intensities (shown in Figure 27) and large variations in the defect bands apparent in Figures 30 and 31. In particular, the $x = 0.9$ sample showed a large increase in PbX_2 between hour 1 and hour 300. As mentioned before, the slight decrease after hour 300 was associated with a shift from a large PbI_2 peak to a few smaller PbBr_2 peaks and probably does not indicate a reversal of the aging process. So, with that in mind, how did the decomposition of the $\text{CH}_3\text{NH}_3\text{Pb}(\text{I}_{0.1}\text{Br}_{0.9})_3$ into $\text{CH}_3\text{NH}_3\text{I}$, PbI_2 and PbBr_2 impact the sub-bandgap EQE spectra? Figure 30 reveals a monotonic *decrease* in the defect band relative to the above gap signal, ultimately falling by a factor of ~ 100 . This drop is concurrent with the increased PbX_2 as measured by XRD.

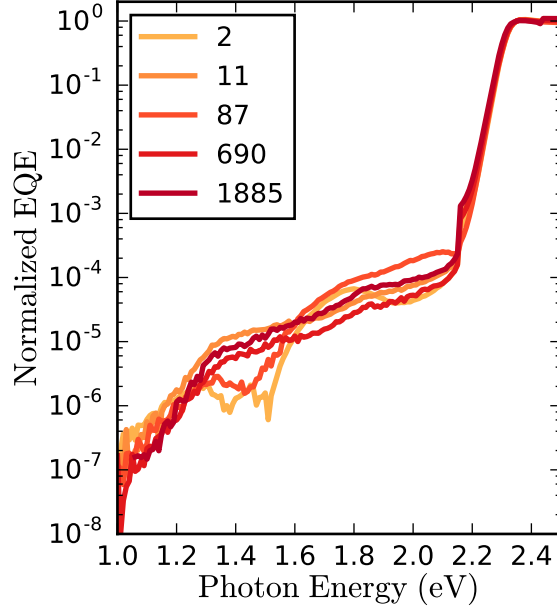


FIGURE 29. EQE spectra, normalized at E_g , for the $\text{CH}_3\text{NH}_3\text{PbBr}_3$ PSC as a function of time following air exposure. The sharp drop in all the spectra, near the bottom of the band edge near 2.15 eV is due to above-bandgap stray light being eliminated by the addition of a long-pass filter.

The evolution of XRD and the defect band seen in EQE for the $x = 0.4$ sample is similar but not as clear. Figure 31 shows a clear, nearly monotonic drop in the portion of the defect band between 1.2 and 1.5 eV. The results for $x = 0.4$ differ from $x = 0.9$ below 1.2 eV and after 241 hours in air. For these energies, at long times, a lower energy defect seems to be increasing with age.

To summarize, four samples were studied longitudinally using XRD to track PbX_2 formation and EQE to track the defect density as they aged. Of those four, two showed very little change in both XRD and the relative defect band. The other two showed clear increases in PbX_2 formation and concurrent decreases in defect band, with the notable exception of the deepest portion of the defect band in the $x = 0.4$ sample for times in excess of 241 hours. Decreasing defect densities in $\text{CH}_3\text{NH}_3\text{Pb}(\text{I}_{1-x}\text{Br}_x)_3$ would help to explain prior observations of increasing internal

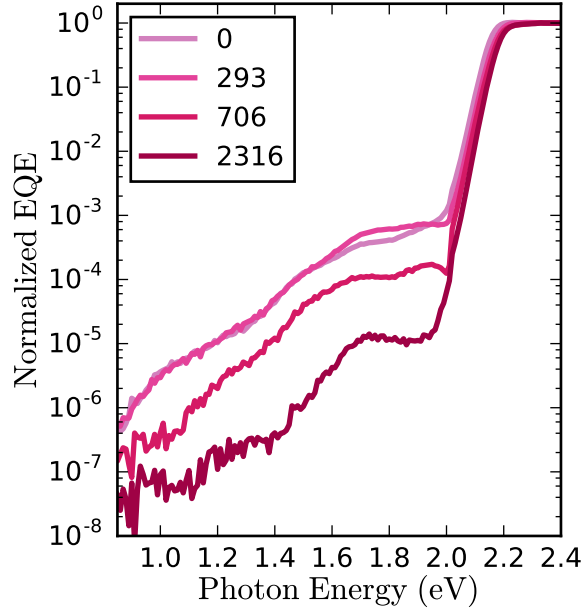


FIGURE 30. EQE spectra, normalized at E_g , for the $\text{CH}_3\text{NH}_3\text{Pb}(\text{I}_{0.1}\text{Br}_{0.9})_3$ PSC as a function of time following air exposure. The marked decrease in the defect band relative to the above bandgap response is concurrent with the formation of PbX_2 species as the perovskite decomposes.

PL quantum yield after several weeks of aging under N_2 , which implies lower defect-mediated recombination rates at low illumination intensities [88]. This increase of PL efficiency with aging time can be explained by passivation of interface states by formation of PbI_2 [107, 108]. According to this interpretation, initial formation of PbI_2 and PbBr_2 at grain surfaces and boundaries would lead to an increase in PL efficiency. In an otherwise optimized device one might expect the photocurrent to increase as well. But, at some point, the degradation will begin reduce absorptive volume within the device as the perovskite phase is consumed and both PL and photocurrent would decrease.

As a final caution, linking PbX_2 formation to the sub-bandgap EQE data could be compromised by the highly non-uniform degradation over the sample area. As shown in Figure 32. Because XRD patterns represent an average over regions much larger

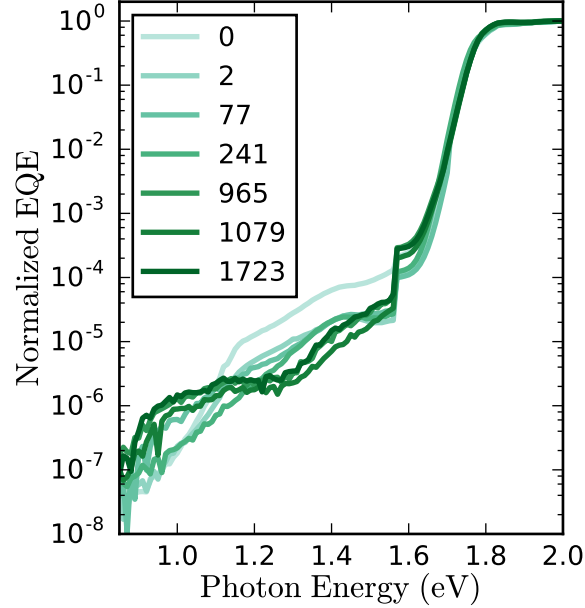


FIGURE 31. EQE spectra, normalized at E_g , for the $\text{CH}_3\text{NH}_3\text{Pb}(\text{I}_{0.6}\text{Br}_{0.4})_3$ PSC as a function of time following air exposure. The sharp feature appearing prominently in spectra with lower defect bands at ~ 1.55 eV is due to the addition of a long-pass filter eliminating above-bandgap stray light. Stray light does not significantly impact these spectra away from the band edges.

than the device area probed by EQE there is no guarantee that the PbX_2 increases detected via XRD lie within the active device area (under the gold contacts) that EQE is sensitive to.

Summary

I have presented sub-bandgap EQE measurements on Au / spiro-OMeTAD / $\text{CH}_3\text{NH}_3\text{Pb}(\text{I}_{1-x}\text{Br}_x)_3$ / TiO_2 / FTO / glass photovoltaic devices. All $\text{CH}_3\text{NH}_3\text{Pb}(\text{I}_{1-x}\text{Br}_x)_3$ compositions, with corresponding bandgaps of $1.6 \leq E_g \leq 2.3$ eV, exhibit low Urbach energies in the range of 15 to 23 meV. While previous studies [64, 86] seemed to indicate that $\text{CH}_3\text{NH}_3\text{Pb}(\text{I}_{1-x}\text{Br}_x)_3$ with middling bromine contents may not be able to achieve such low E_u , this study makes clear that it



FIGURE 32. A photograph of degraded $\text{CH}_3\text{NH}_3\text{Pb}(\text{I}_{0.6}\text{Br}_{0.4})_3$ solar cells. Note the paler patch in the upper left hand corner of the cell. The two cells in this region were not used because this PbI_2 rich section shunted the cells. This region seemingly contributes to the high baseline of PbI_2 seen from $t=0$ in this cell. Subsequent evolution apparent in XRD was not visually recorded anywhere, but there is no guarantee that it took place within the cells used for electrical characterization as the region of sensitivity for XRD would have included almost all the devices.

is simply a matter of optimizing the growth conditions. These Urbach energies are significantly lower than most conventional inorganic semiconductors with similar bandgaps, especially for $E_g \geq 1.9$ eV and are not affected by long-term aging of perovskite-based photovoltaic devices (as indicated by co-presence of PbI_2 and PbBr_2). Moreover, this study reveals the presence of sub-bandgap defect states for all compositions. These states can be fit with one or two point defects for pure $\text{CH}_3\text{NH}_3\text{PbI}_3$ or mixed $\text{CH}_3\text{NH}_3\text{Pb}(\text{I}_{1-x}\text{Br}_x)_3$ compositions, respectively. With increasing Br-content the observed defect bands tend to have higher densities near the middle of the band gap. This is particularly true for $\text{CH}_3\text{NH}_3\text{PbBr}_3$ which also show much lower internal photoluminescence quantum yield.

While the longitudinal study of XRD patterns and EQE spectra demonstrates that precipitation of PbI_2 and PbBr_2 do not affect the Urbach energy in these perovskites, it also shows that precipitation may result in a reduction of deep defects. This latter development would help to explain previous observations of *increased* photoluminescence efficiency concurrent with PbI_2 precipitation [88, 107, 108]. Such a theory would imply that at least some portion of the observed defect bands are due to surface states residing at grain boundaries. Given these observations, it seems likely that the combination of sub-bandgap EQE, which can directly detect midgap states, and PL-based measurements that track total non-radiative recombination could be further utilized to develop synthesis methods that passivate the observed defects. Clearly, it would be useful to identify a passivating agent that is not part and parcel to the slow-but-sure decomposition of the solar cell's absorber layer.

In the next chapter, I will summarize the work presented in this dissertation and discuss the implications of the results presented in Chapters IV and V for our understanding of defect formation in the $\text{CH}_3\text{NH}_3\text{Pb}(\text{I}_{1-x}\text{Br}_x)_3$ system.

CHAPTER VI

CONCLUSION AND FUTURE DIRECTIONS

In this work, I have used sub-bandgap EQE, TPC, and TPI to map out the sub-bandgap density of states (DOS) in a wide variety of solar cell absorbers and connect the DOS to the performance of the solar cell, or of the absorber itself. Reference to some of my earlier work on $\text{Cu}_2\text{ZnSn}(\text{Se}_{1-x}\text{S}_x)_4$ [42] and InP [54] was used demonstrate the broad applicability of these techniques in characterizing solar cell absorbers and establish clear cut examples of the impact the sub-bandgap DOS can have photovoltaic device performance. The work on $\text{Cu}_2\text{ZnSn}(\text{Se}_{1-x}\text{S}_x)_4$ demonstrates the importance of the Urbach energy as a metric for solar cell absorbers by confirming the deleterious impact that a large Urbach energy (broad band-edges) can have on performance. The example in InP illustrates some advantages of TPC and TPI over EQE. Specifically, the selective sensitivity of TPC to absorption processes within the depletion region and the ability of TPC and TPI, taken together, to estimate minority carrier collection from the depletion region. This information was used in concert with other data to develop a theory regarding the effectiveness of hydrogen plasma passivation of InP thin-films.

In applying these techniques to perovskite solar cells, we were again able to begin identifying the connection between the sub-bandgap DOS and various aspects of device performance and carrier dynamics. The first point of interest is meaningful mostly in contrast with prior work on other poly-crystalline thin films. Every single perovskite cell investigated in this study showed an Urbach energy in the relatively narrow range of 15–23 meV. This is despite the fact that these samples were fabricated using three different methods in two different labs; one at Oxford, and the other at UC

Berkeley. The longitudinal comparison of Urbach energies with aging demonstrated that low Urbach energy in perovskites is robust against the degradation of the perovskite. The collective experience of the photovoltaics research community in poly-crystalline $\text{Cu}_2\text{ZnSn}(\text{Se}_{1-x}\text{S}_x)_4$ [42, 43] and $\text{Cu}(\text{In}_{1-x}\text{Ga}_x)(\text{Se}_{1-y}\text{S}_y)_2$ [93], as well as across a wide-variety of solar cell absorbers including crystalline and amorphous materials [62] suggests that this is very good news for the future of perovskite solar cells. Perhaps this fact, coupled with the relative ease of perovskite synthesis (no high vacuum required; no need for temperatures in excess of 120 °C) helps to explain how perovskites have managed to make the same gains in efficiency over the last 7 years that each of today’s established commercial technologies took 30 to achieve.

While the observation of easily achievable, and stable, low Urbach energies fits with the notion that perovskites tend not to form native defects this study revealed defect bands that come quite close to mid-gap in some samples. All of the $x=0$, $\text{CH}_3\text{NH}_3\text{PbI}_3$, samples showed a broad defect that was best fit by a gaussian defect between 1.3 and 1.4 eV, and some required an additional component closer to the middle of the gap. In the set of samples from Oxford, this defect’s density (using the EQE as a proxy) was correlated with lower-steady state performance and more pronounced hysteresis. Furthermore, the most defective cells permitted the detection of the defect band in TPC and TPI, in addition to EQE. This suggests that the defect signal originates in the absorber layer. The minority carrier collection implied by the large dynamic range from interband transitions to the defect band was commensurate with the low performance in these devices.

The higher band gap perovskites corroborated this story by again revealing mid-gap states. In this case, a higher density of states near mid-gap was in agreement with direct measurement of higher rates of non-radiative recombination.

While Urbach energies in these samples were insensitive to the decomposition of $\text{CH}_3\text{NH}_3\text{Pb}(\text{I}_{1-x}\text{Br}_x)_3$ samples that showed the largest increase in PbI_2 and PbBr_2 showed a reduction in deep defect density. This supports previous work suggesting that PbI_2 passivates grain boundaries in $\text{CH}_3\text{NH}_3\text{Pb}(\text{I}_{1-x}\text{Br}_x)_3$ [88, 107, 108].

Taken together these results show that defects in perovskite solar cells, likely residing at grain boundaries, can form in sufficient numbers to reduce steady state performance and play a role in hysteresis, certainly via recombination and probably also in the form of mobile ions that temporarily modify the built-in field. This conclusion is consistent with a growing consensus [34, 35, 73, 79] emphasizing defect control as a means to eliminating hysteresis in perovskite solar cells and minimizing the importance of ferroelectric effects [38].

Attempts to improve the synthesis method of perovskites or develop passivating treatments based on the information and characterization methods presented in this dissertation should be sure to also consider the effects on the stability of the cell. Stability, not peak efficiency, is the biggest challenge in commercializing this promising class of materials. If we are lucky, these goals will go hand-in-hand.

CHAPTER VII

APPENDICES

A. Rate-Dependent Current-Voltage Data

The data in Table 1 and Figure 18 were sourced from the current voltage data shown in Figures 15 and 33 to 36

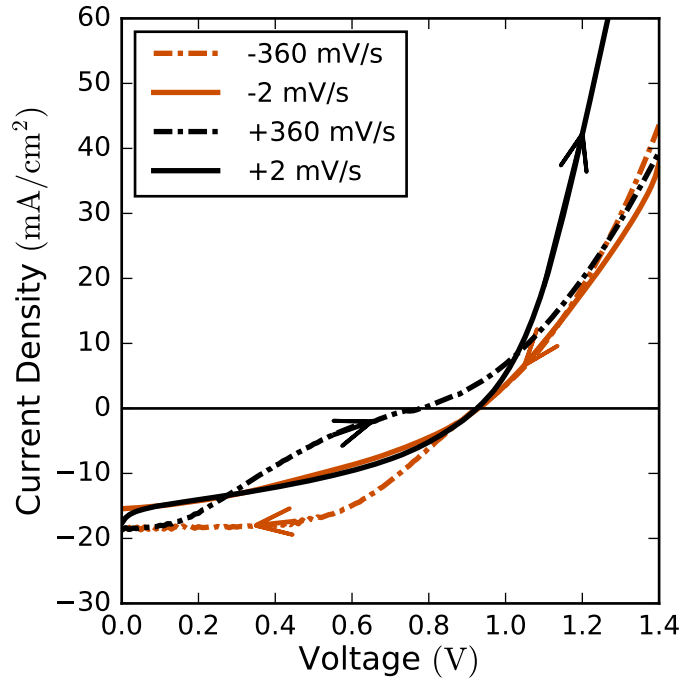


FIGURE 33. Forward and reverse J - V curves at different scan rates for Vapor 2.

B. Band-Gap Determination from EQE and TPC

The bandgap for each sample was determined using a slight adaptation to the method of Tauc [74]. Typically, for a direct and allowed transition, one would simply plot $(\alpha h\nu)^2$, where α is the absorbance and $h\nu$ is the photon energy, against energy in eV and extrapolate the linear region near the band edge to the intercept with the

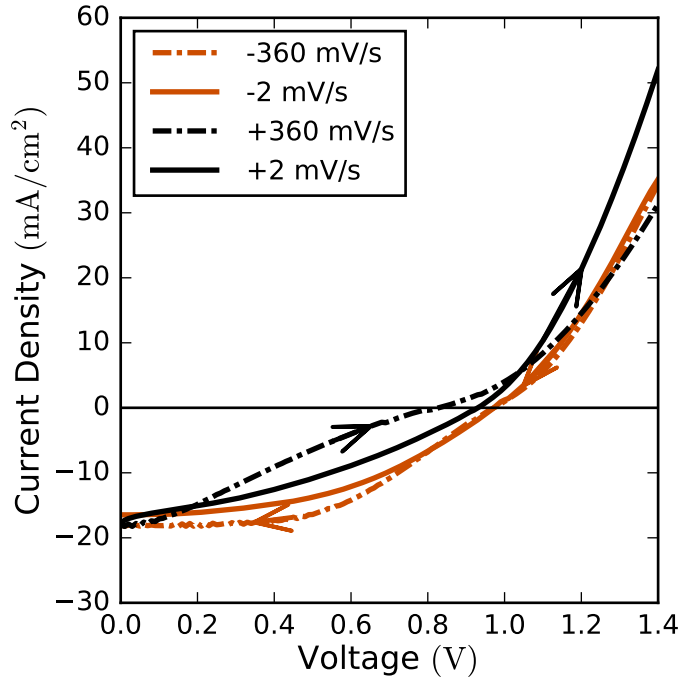


FIGURE 34. Forward and reverse J - V curves at different scan rates for Vapor 3.

abscissa where absorption is zero. In this case, we collected EQE or TPC rather than absorption data and use these in place of absorbance to make the plot. Because only a very small range (~ 0.05 eV) in energy is needed for the linear fit to the Tauc plot, variations in carrier collection efficiency and reflectance have very little impact. A region that is linear on the Tauc plot still appears, and using TPC or EQE in place of absorption only changes the scale factor of the fit, not the intercept with the abscissa.

For the samples presented in Chapter IV, all the bandgaps were found in the range 1.57–1.60 eV.

C. Fitting Defect Spectra

Fits to the EQE spectra that generated the “Defect EQE” values used in Figure 18 are shown in Figures 46 to 50. Fits the the data are shown as a solid black line with the underlying Gaussian density of of states for the defect bands shown

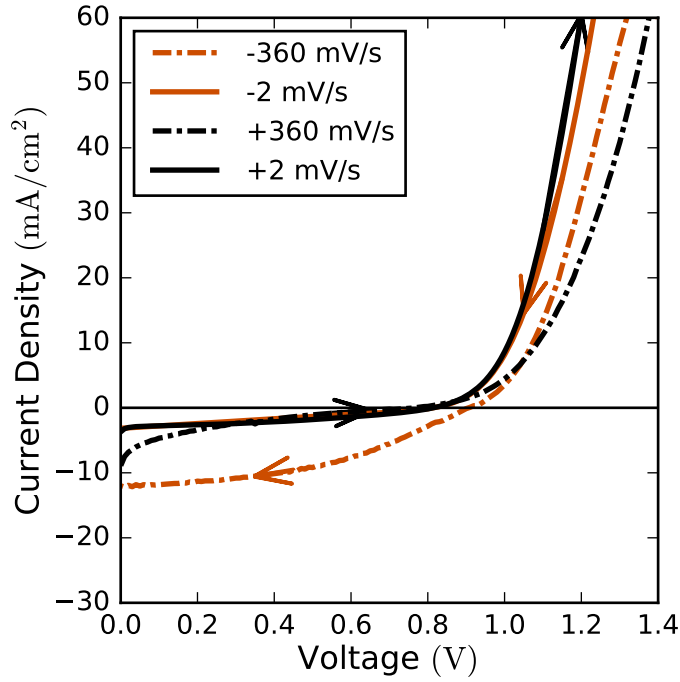


FIGURE 35. Forward and reverse J - V curves at different scan rates for Dip 1.

as dash-dotted lines. Fits were optimized by performing a non-linear, least-squares minimization of the sum of residual R_d , given by:

$$R_d(E) = [|\log_{10}(EQE(E)) - \log_{10}(EQE_{d_1}(E) + EQE_{d_2}(E))|^2]^{1/2}. \quad (7.1)$$

Where EQE_{d_i} refers to the i^{th} defects contribution to the EQE signal at energy E given by equation 5.1. The fits shown here were a result of fitting with a pair of defects whose energies were constrained to 1.34 eV and 0.76 eV while allowing density of the defect to be freely adjusted. The motivation for fixing the defect energies is described in Chapter IV.

D. Minority Carrier Collection in $\text{CHNH}_3\text{PbI}_3$

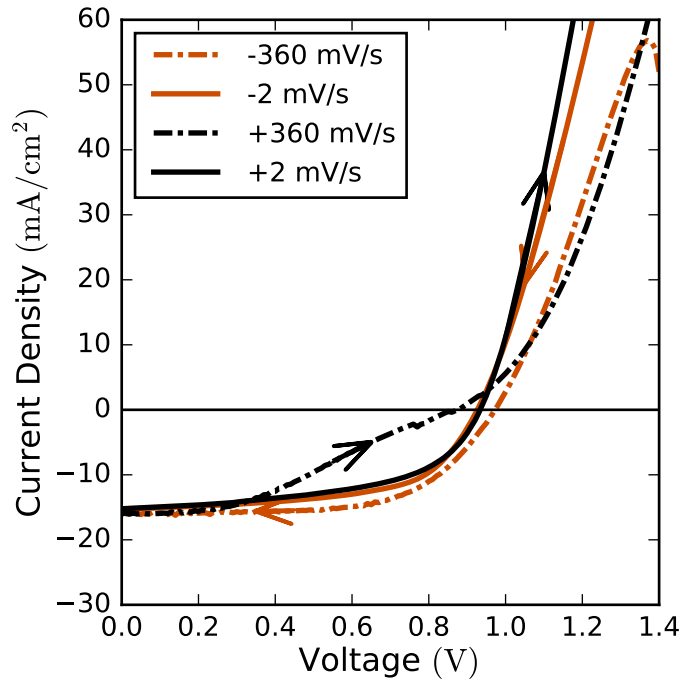


FIGURE 36. Forward and reverse J - V curves at different scan rates for Dip 2.

As discussed in Chapter III, the minority carrier collection efficiency *from the depletion region* can be extracted by aligning the spectra near mid-gap. As shown in Figures 51 and 52, Dip 1 and Vapor 1 yielded spectra suitable for this analysis. Though the noise is significant near mid-gap both sets of spectra imply a collection efficiency between 20–40%.

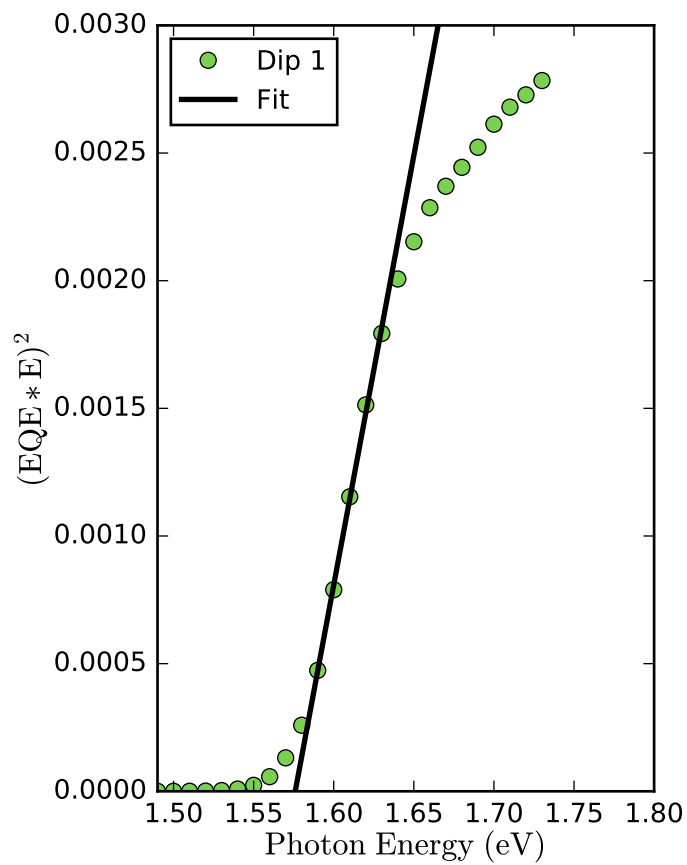


FIGURE 37. Tauc plot used to determine the bandgap from the EQE spectrum for the sample Dip 1 described in Chapter IV.

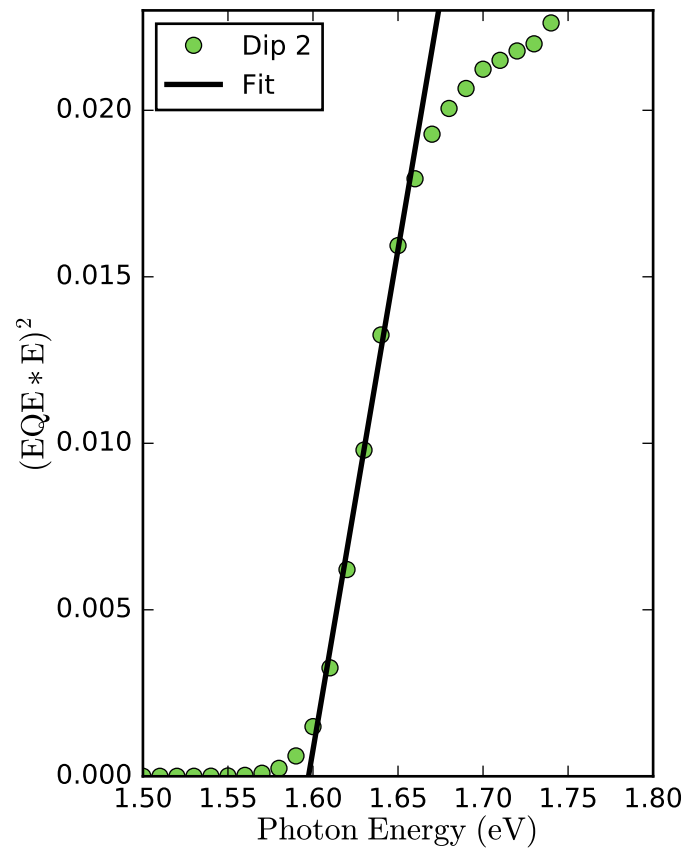


FIGURE 38. Tauc plot used to determine the bandgap from the EQE spectrum for the sample Dip 2 described in Chapter IV.

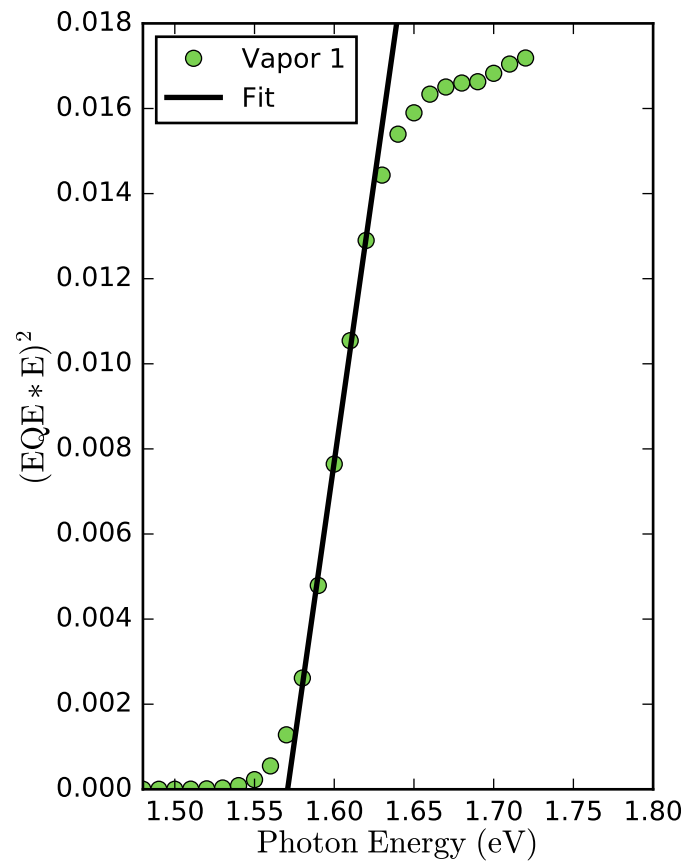


FIGURE 39. Tauc plot used to determine the bandgap from the EQE spectrum for the sample Vapor 1 described in Chapter IV.

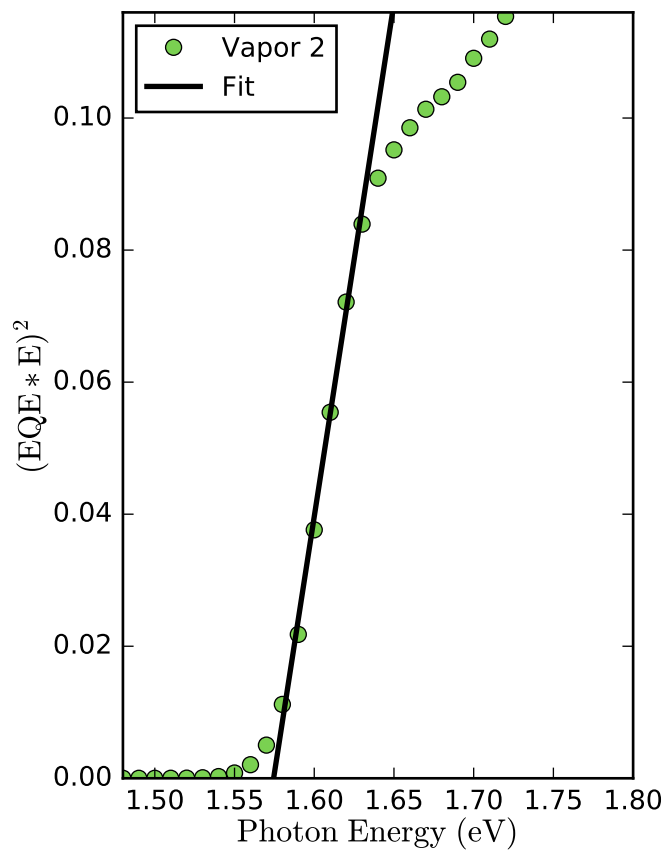


FIGURE 40. Tauc plot used to determine the bandgap from the EQE spectrum for the sample Vapor 2 described in Chapter IV.

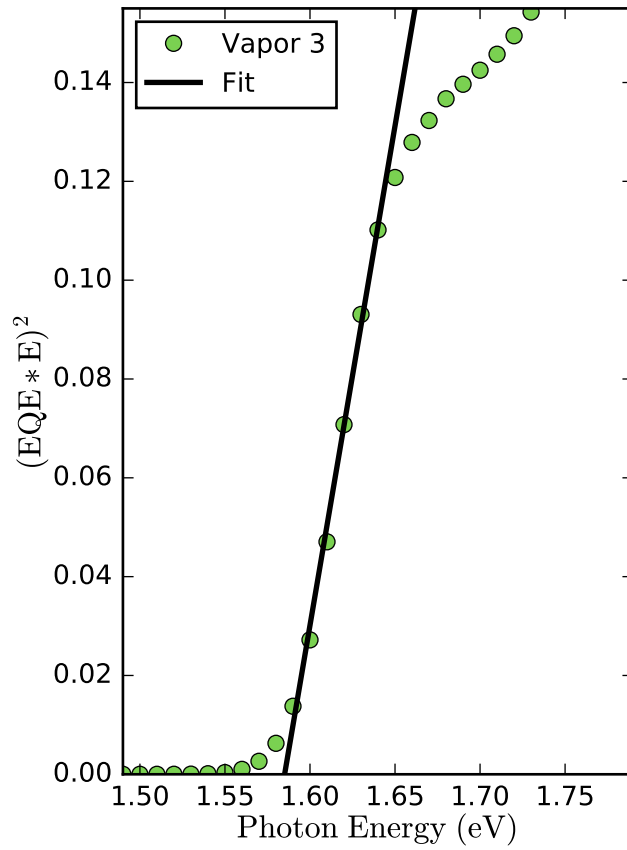


FIGURE 41. Tauc plot used to determine the bandgap from the EQE spectrum for the sample Vapor 3 described in Chapter IV.

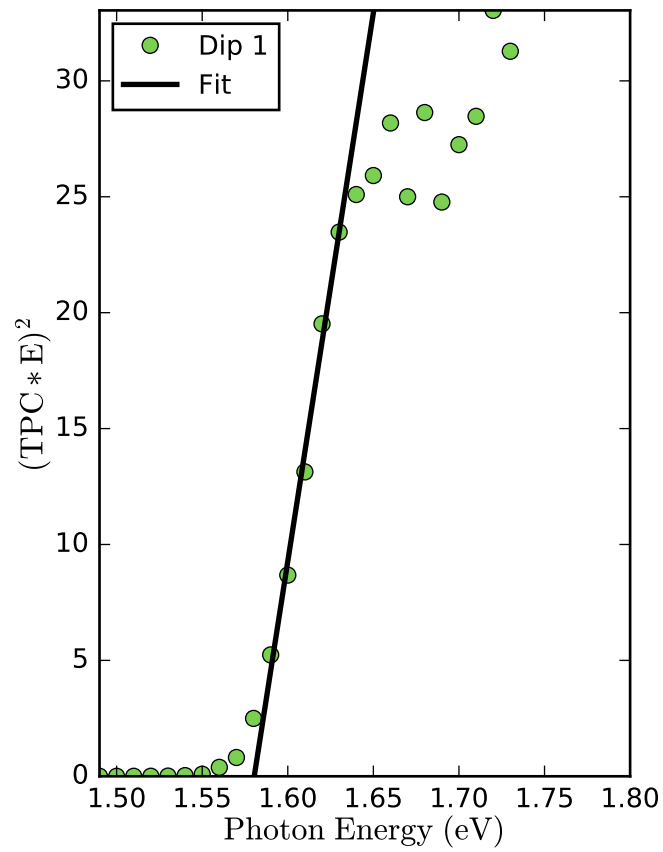


FIGURE 42. Tauc plot used to determine the bandgap from the TPC spectrum for the sample Dip 1 described in Chapter IV.

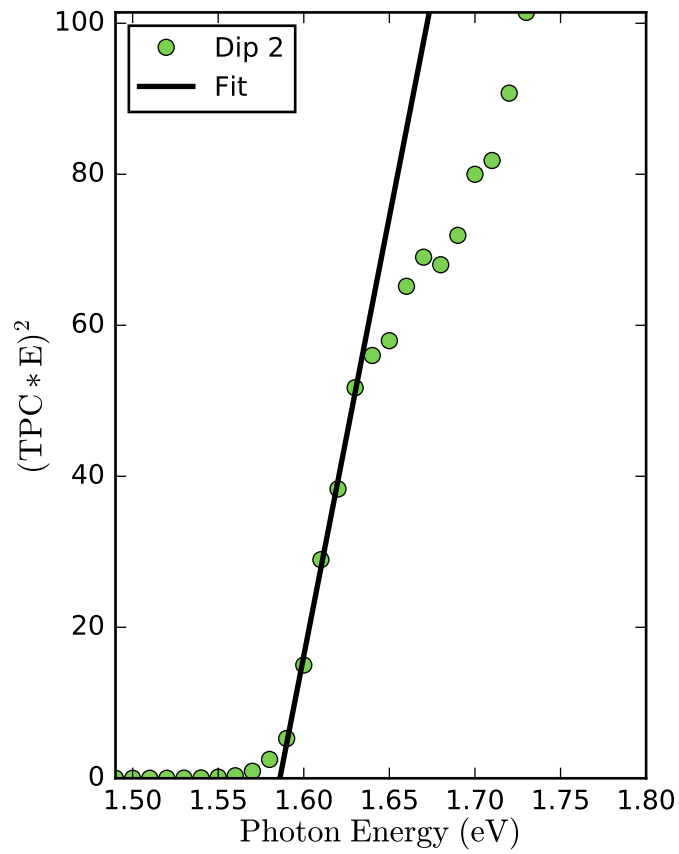


FIGURE 43. Tauc plot used to determine the bandgap from the TPC spectrum for the sample Dip 2 described in Chapter IV.

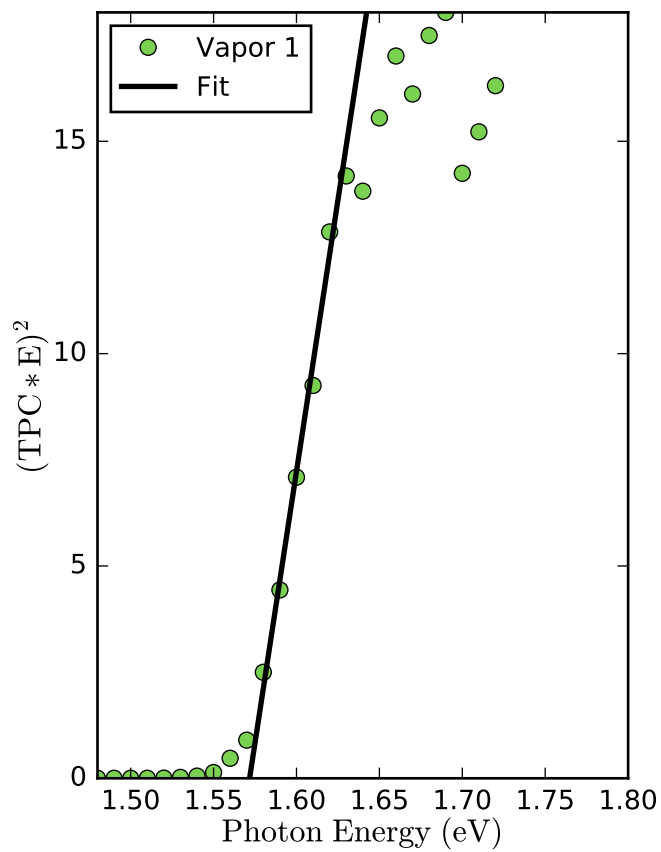


FIGURE 44. Tauc plot used to determine the bandgap from the TPC spectrum for the sample Vapor 1 described in Chapter IV.

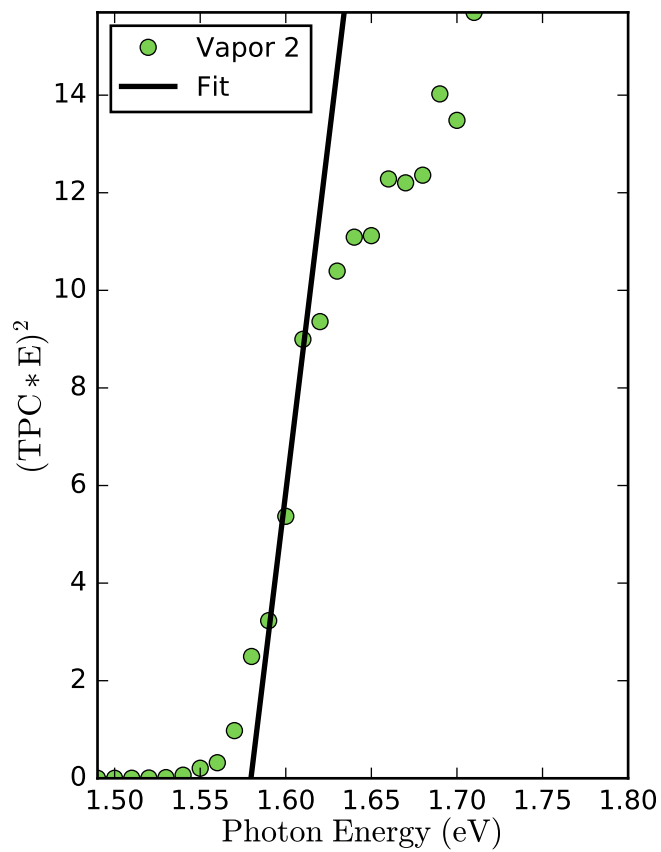


FIGURE 45. Tauc plot used to determine the bandgap from the TPC spectrum for the sample Vapor 2 described in Chapter IV.

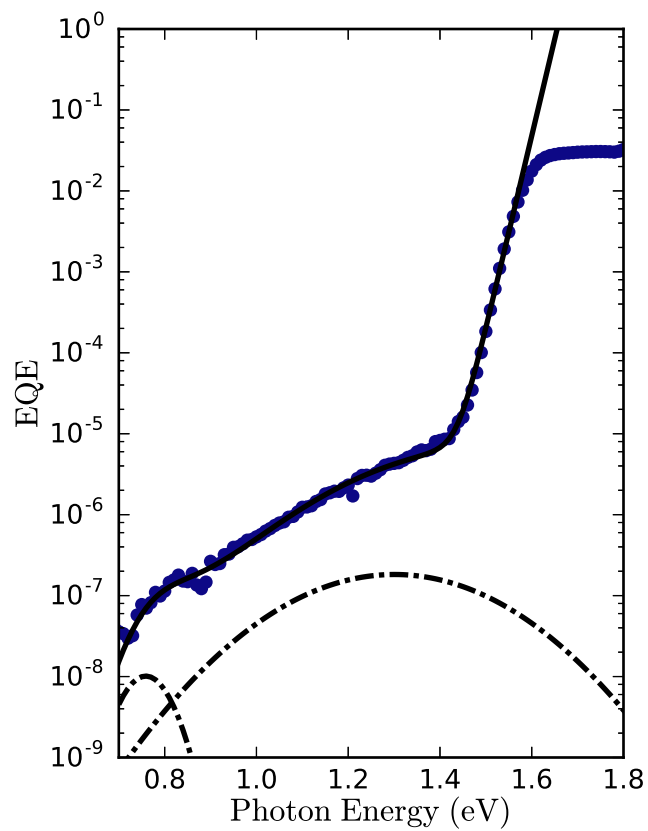


FIGURE 46. The EQE spectrum for Dip 1. This cell had the highest defect EQE showing significant contributions from the 1.34 eV and 0.76 eV defects and the lowest steady state efficiency.

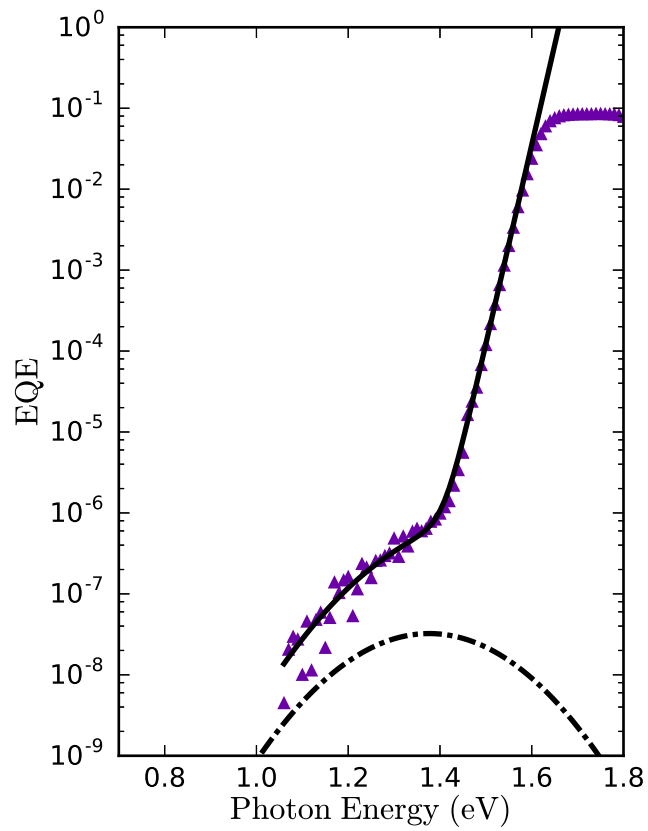


FIGURE 47. The EQE spectrum for Dip 2. With the highest steady-state efficiency of any cell in this series, it shows no apparent contribution from the 0.76 eV defect.

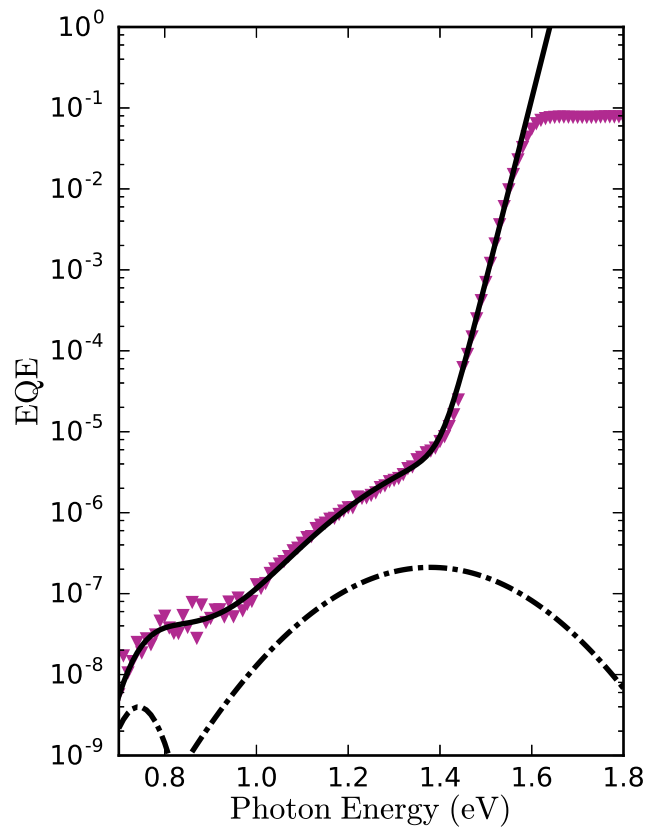


FIGURE 48. The EQE spectrum for Vapor 1. This low performing cell had significant contributions from the 1.34 eV and 0.76 eV defects and most clearly shows that a single defect fit would be inadequate.

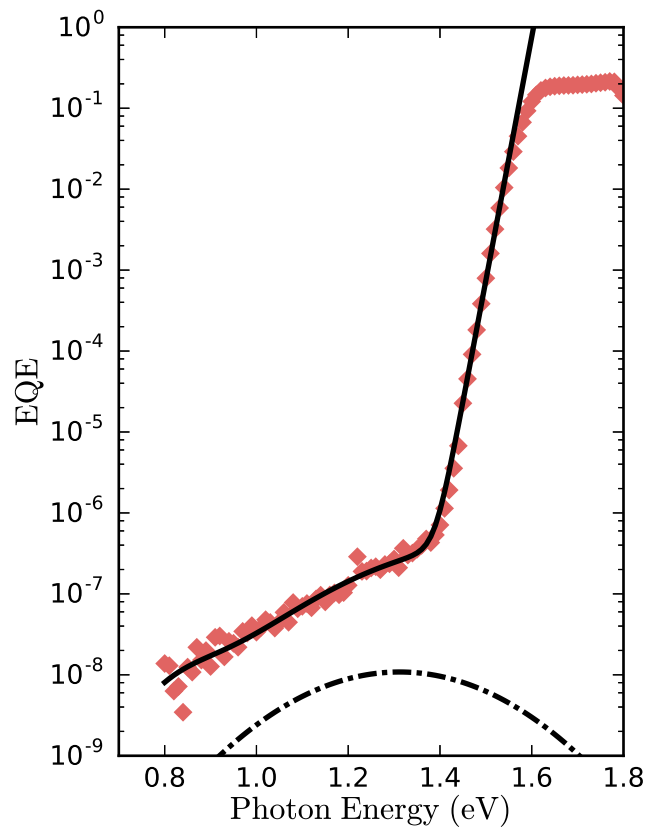


FIGURE 49. The EQE spectrum for Vapor 2 shows relatively low contributions from the 1.34 eV and 0.76 eV defects.

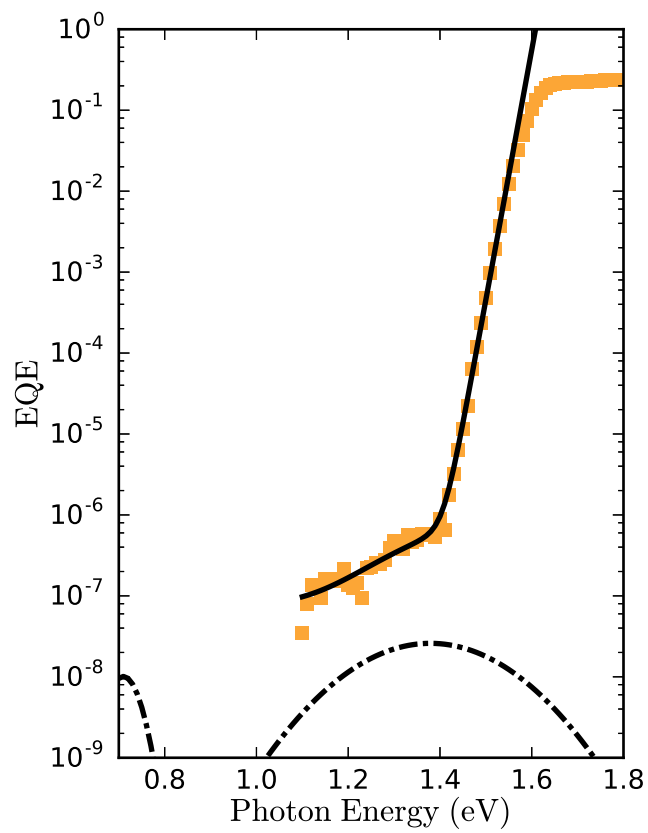


FIGURE 50. The EQE spectrum for Vapor 3 reveals a relatively low contribution to the EQE from defects.

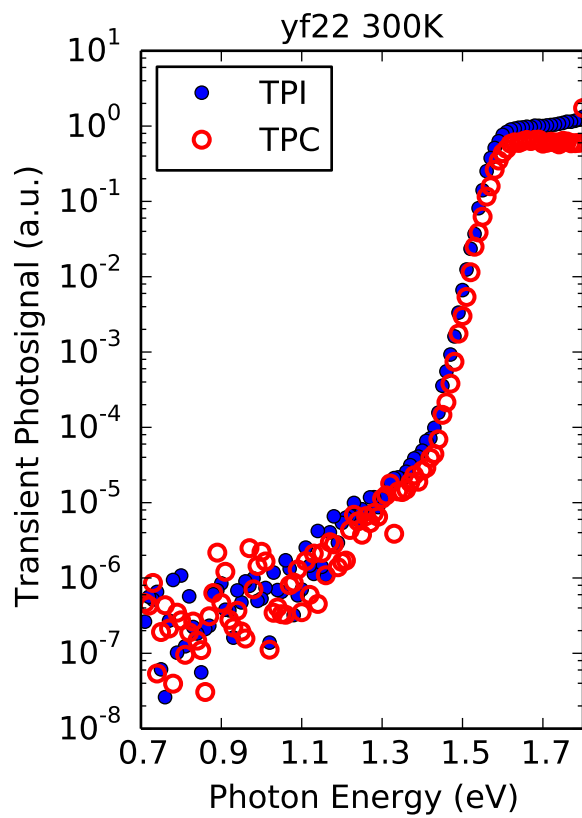


FIGURE 51. TPC and TPI spectra for Vapor 1 aligned in the defect band. The large above-gap response in TPC relative to the defect band is indicative of poor minority carrier collection from the depletion region.

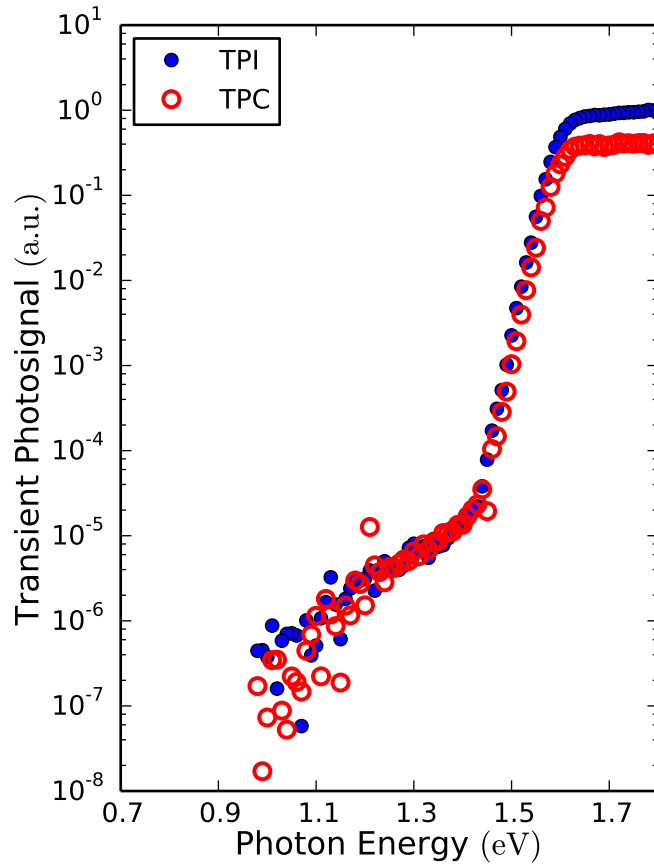


FIGURE 52. TPC and TPI spectra for Dip 1 aligned in the defect band. The large above-gap response in TPC relative to the defect band is indicative of poor minority carrier collection from the depletion region.

REFERENCES CITED

- [1] T. Stocker, D. Qin, G.-K. Plattner, L. Alexander, S. Allen, N. Bindoff, F.-M. Breon, J. Church, U. Cubasch, S. Emori, P. Forster, P. Friedlingstein, N. Gillett, J. Gregory, D. Hartmann, E. Jansen, B. Kirtman, R. Knutti, K. KrishnaKumar, P. Lemke, J. Marotzke, V. Masson-Delmotte, G. Meehl, I. Mokhov, S. Piao, V. Ramaswamy, D. Randall, M. Rhein, M. Rojas, C. Sabine, D. Shindell, L. Talley, D. Vaughan, and S.-P. Xie, *Climate Change 2013: The Physical Science Basis. Contribution of Working Group I to the Fifth Assessment Report of the Intergovernmental Panel on Climate Change*, pp. 33–115. Cambridge, United Kingdom and New York, NY, USA: Cambridge University Press, 2013.
- [2] G. Masson, “Trends in photovoltaic applications,” tech. rep., International Energy Agency Photovoltaic Power Systems Programme, St. Ursen, Switzerland, 2016.
- [3] B. Obama, “The irreversible momentum of clean energy,” *Science*, vol. 355, pp. 126–129, Jan. 2017.
- [4] D. B. Needleman, J. R. Poindexter, R. C. Kurchin, I. M. Peters, G. Wilson, and T. Buonassisi, “Economically Sustainable Scaling of Photovoltaics to Meet Climate Targets,” *Energy & Environmental Science*, vol. 9, pp. 2122–2129, 2016.
- [5] T. Tiedje, E. Yablonovitch, G. D. Cody, and B. G. Brooks, “Limiting efficiency of silicon solar cells,” *IEEE Transactions on Electron Devices*, vol. 31, pp. 711–716, May 1984.
- [6] “Best Research Cell Efficiencies,” 2017. Retrieved from <https://www.nrel.gov/pv/assets/images/efficiency-chart.png>.
- [7] “N330 Photovoltaic Module HIT,” 2016. Retrieved from <ftp://ftp.panasonic.com/solar/specsheet/n325330-spec-sheet.pdf>.
- [8] “Sunpower x-series,” 2016. Retrieved from <https://us.sunpower.com/sites/sunpower/files/media-library/data-sheets/ds-x21-series-335-345-residential-solar-panels.pdf>.
- [9] M. Woodhouse and A. Goodrich, “A manufacturing cost analysis relevant to single- and dual-junction photovoltaic cells fabricated with III-Vs and III-Vs grown on Czochralski silicon,” tech. rep., NREL, 2013.
- [10] “Flex-02w series,” 2016. Retrieved from http://miasole.com/wp-content/uploads/2015/08/FLEX-02W_Datasheet_2.pdf.

- [11] “Catalina power plant,” 2015. Retrieved from <http://www.solar-frontier.com/eng/casestudies/caselist/C046970.html>.
- [12] “First solar series 4 pv module,” 2016. Retrieved from [http://www.firstsolar.com/-/media/First-Solar/Technical-Documents/Series-4-Datasheets/Series-4-Module-Datasheet---V3-103116-\(1\).ashx](http://www.firstsolar.com/-/media/First-Solar/Technical-Documents/Series-4-Datasheets/Series-4-Module-Datasheet---V3-103116-(1).ashx).
- [13] E. Wesoff, “Desert Sunlight, Another 550MW Solar Farm From First Solar, Now Fully Operational,” 2015. Retrieved from <https://www.greentechmedia.com/articles/read/desert-sunlight-yet-another-550-mw-solar-farm-from-first-solar-now-fully-op>.
- [14] “Solar is no longer a compromise [press release],” 2016. Retrieved from <http://www.firstsolar.com/About%20Us/Press%20Center/2016/January/Solar%20Is%20No%20Longer%20a%20Compromise>.
- [15] V. Fthenakis, “Sustainability of photovoltaics: The case for thin-film solar cells,” *Renewable and Sustainable Energy Reviews*, vol. 13, no. 9, pp. 2746 – 2750, 2009.
- [16] P. C. K. Vesborg and T. F. Jaramillo, “Addressing the terawatt challenge: scalability in the supply of chemical elements for renewable energy,” *RSC Adv.*, vol. 2, pp. 7933–7947, 2012.
- [17] A. Kojima, K. Teshima, Y. Shirai, and T. Miyasaka, “Organometal halide perovskites as visible-light sensitizers for photovoltaic cells,” *Journal of the American Chemical Society*, vol. 131, no. 17, pp. 6050–6051, 2009.
- [18] M. A. Green, “The path to 25% silicon solar cell efficiency: History of silicon cell evolution,” *Progress in Photovoltaics: Research and Applications*, vol. 17, no. 3, pp. 183–189, 2009.
- [19] J.-H. Im, C.-R. Lee, J.-W. Lee, S.-W. Park, and N.-G. Park, “6.5% efficient perovskite quantum-dot-sensitized solar cell,” *Nanoscale*, vol. 3, pp. 4088–4093, 2011.
- [20] H.-S. Kim, C.-R. Lee, J.-H. Im, K.-B. Lee, T. Moehl, A. Marchioro, S.-J. Moon, R. Humphry-Baker, J.-H. Yum, J. E. Moser, M. Grätzel, and N.-G. Park, “Lead Iodide Perovskite Sensitized All-Solid-State Submicron Thin Film Mesoscopic Solar Cell with Efficiency Exceeding 9%,” *Sci. Rep.*, vol. 2, p. 591, Aug. 2012.
- [21] M. M. Lee, J. Teuscher, T. Miyasaka, T. N. Murakami, and H. J. Snaith, “Efficient hybrid solar cells based on meso-superstructured organometal halide perovskites,” *Science*, vol. 338, no. 6107, pp. 643–647, 2012.
- [22] M. Grätzel, “The light and shade of perovskite solar cells,” *Nat. Mater.*, vol. 13, no. 9, pp. 838–842, 2014.

- [23] L. Etgar, P. Gao, Z. Xue, Q. Peng, A. K. Chandiran, B. Liu, M. K. Nazeeruddin, and M. Grätzel, “Mesoscopic $\text{CH}_3\text{NH}_3\text{PbI}_3/\text{TiO}_2$ heterojunction solar cells,” *Journal of the American Chemical Society*, vol. 134, no. 42, pp. 17396–17399, 2012.
- [24] N. J. Jeon, J. H. Noh, Y. C. Kim, W. S. Yang, S. Ryu, and S. I. Seok, “Solvent engineering for high-performance inorganic-organic hybrid perovskite solar cells,” *Nat Mater*, vol. 13, no. 9, pp. 897–903, 2014.
- [25] S. Lany and A. Zunger, “Light- and bias-induced metastabilities in $\text{Cu}(\text{In,Ga})\text{Se}_2$ based solar cells caused by the $(V_{\text{Se}}-V_{\text{Cu}})$ vacancy complex,” *J. Appl. Phys.*, vol. 100, no. 11, p. 113725, 2006.
- [26] W. Shockley and W. T. Read, “Statistics of the Recombination of Holes and Electrons,” *Phys. Rev.*, vol. 87, no. 46, pp. 835–842, 1952.
- [27] R. N. Hall, “Electron-hole recombination in germanium,” *Phys. Rev.*, vol. 87, pp. 387–387, July 1952.
- [28] D. P. Würfel, *Physics of Solar Cells: From Basic Principles to Advanced Concepts*. Weinheim: Wiley-VCH Verlag GmbH & Co. KgaA, 2009.
- [29] Y. Zhou and G. Long, “Low Density of Conduction and Valence Band States Contribute to the High Open-Circuit Voltage in Perovskite Solar Cells,” *J. Phys. Chem. C*, vol. 121, pp. 1455–1462, Jan. 2017.
- [30] D. Shi, V. Adinolfi, R. Comin, M. Yuan, E. Alarousu, A. Buin, Y. Chen, S. Hoogland, A. Rothenberger, K. Katsiev, Y. Losovyj, X. Zhang, P. A. Dowben, O. F. Mohammed, E. H. Sargent, and O. M. Bakr, “Low trap-state density and long carrier diffusion in organolead trihalide perovskite single crystals,” *Science (80-.)*, vol. 347, no. 6221, 2015.
- [31] Y. Shao, Z. Xiao, C. Bi, Y. Yuan, and J. Huang, “Origin and elimination of photocurrent hysteresis by fullerene passivation in $\text{CH}_3\text{NH}_3\text{PbI}_3$ planar heterojunction solar cells,” *Nat. Commun.*, vol. 5, p. 5784, Dec. 2014.
- [32] J. Xu, A. Buin, A. H. Ip, W. Li, O. Voznyy, R. Comin, M. Yuan, S. Jeon, Z. Ning, J. J. McDowell, P. Kanjanaboos, J.-P. Sun, X. Lan, L. N. Quan, D. H. Kim, I. G. Hill, P. Maksymovych, and E. H. Sargent, “Perovskite-fullerene hybrid materials suppress hysteresis in planar diodes,” *Nat. Commun.*, vol. 6, p. 7081, May 2015.
- [33] E. L. Unger, E. T. Hoke, C. D. Bailie, W. H. Nguyen, A. R. Bowring, T. Heumüller, M. G. Christoforo, and M. D. McGehee, “Hysteresis and transient behavior in current-voltage measurements of hybrid-perovskite absorber solar cells,” *Energy Environ. Sci.*, vol. 7, pp. 3690–3698, 2014.

- [34] W. Tress, N. Marinova, T. Moehl, S. M. Zakeeruddin, N. Mohammad K., M. K. Nazeeruddin, and M. Gratzel, “Understanding the rate-dependent J-V hysteresis, slow time component, and aging in $\text{CH}_3\text{NH}_3\text{PbI}_3$ perovskite solar cells: the role of a compensated electric field,” *Energy Environ. Sci.*, vol. 8, no. 3, pp. 995–1004, 2015.
- [35] S. van Reenen, M. Kemerink, and H. J. Snaith, “Modeling Anomalous Hysteresis in Perovskite Solar Cells,” *J. Phys. Chem. Lett.*, vol. 6, pp. 3808–3814, Sep. 2015.
- [36] J. Wei, Y. Zhao, H. Li, G. Li, J. Pan, D. Xu, Q. Zhao, and D. Yu, “Hysteresis Analysis Based on the Ferroelectric Effect in Hybrid Perovskite Solar Cells,” *J. Phys. Chem. Lett.*, vol. 5, pp. 3937–3945, Nov. 2014.
- [37] J. M. Frost, K. T. Butler, and A. Walsh, “Molecular ferroelectric contributions to anomalous hysteresis in hybrid perovskite solar cells,” *APL Mater.*, vol. 2, p. 081506, Aug. 2014.
- [38] G. E. Eperon, G. M. Paternò, R. J. Sutton, A. Zampetti, A. A. Haghighirad, F. Cacialli, H. J. Snaith, J. Verbeeck, J. Manca, E. Mosconi, F. de Angelis, H. Boyen, M. D. Biegalski, M. S. Ryzhowski, X. Q. Pan, D. G. Schlom, L. Q. Chen, R. Ramesh, and C. B. Eom, “Inorganic caesium lead iodide perovskite solar cells,” *J. Mater. Chem. A*, vol. 3, no. 39, pp. 19688–19695, 2015.
- [39] G. Cody, “Urbach edge of crystalline and amorphous silicon: a personal review,” *Journal of Non-Crystalline Solids*, vol. 141, pp. 3 – 15, 1992.
- [40] S. R. Johnson and T. Tiedje, “Temperature dependence of the urbach edge in GaAs,” *Journal of Applied Physics*, vol. 78, no. 9, pp. 5609–5613, 1995.
- [41] S. M. Wasim, C. Rincón, G. Marín, P. Bocaranda, E. Hernández, I. Bonalde, and E. Medina, “Effect of structural disorder on the urbach energy in Cu ternaries,” *Phys. Rev. B*, vol. 64, p. 195101, Oct. 2001.
- [42] D. W. Miller, C. W. Warren, O. Gunawan, T. Gokmen, D. B. Mitzi, and J. D. Cohen, “Electronically active defects in the $\text{Cu}_2\text{ZnSn}(\text{Se},\text{S})_4$ alloys as revealed by transient photocapacitance spectroscopy,” *Appl. Phys. Lett.*, vol. 101, no. 14, p. 142106, 2012.
- [43] T. Gokmen, O. Gunawan, T. K. Todorov, and D. B. Mitzi, “Band tailing and efficiency limitation in kesterite solar cells,” *Applied Physics Letters*, vol. 103, no. 10, p. 103506, 2013.
- [44] T. Gershon, O. Gunawan, T. Gokmen, K. W. Brew, S. Singh, M. Hopstaken, J. R. Poindexter, E. S. Barnard, T. Buonassisi, and R. Haight, “Analysis of loss mechanisms in $\text{Ag}_2\text{ZnSnSe}_4$ Schottky barrier photovoltaics,” *J. Appl. Phys.*, vol. 121, no. 17, p. 174501, 2017.

- [45] A. V. Gelatos, J. D. Cohen, and J. P. Harbison, "Assessment of lattice relaxation effects in transitions from mobility gap states in hydrogenated amorphous silicon using transient photocapacitance techniques," *Applied Physics Letters*, vol. 49, no. 12, p. 722, 1986.
- [46] A. V. Gelatos, K. K. Mahavadi, J. D. Cohen, and J. P. Harbison, "Transient photocapacitance and photocurrent studies of undoped hydrogenated amorphous silicon," *Applied Physics Letters*, vol. 53, no. 5, p. 403, 1988.
- [47] J. T. Heath, J. D. Cohen, W. N. Shafarman, D. X. Liao, and A. A. Rockett, "Effect of Ga content on defect states in CIGS photovoltaic devices," *Appl. Phys. Lett.*, vol. 80, no. 24, p. 4540, 2002.
- [48] P. T. Erslev, J. W. Lee, W. N. Shafarman, and J. D. Cohen, "The influence of Na on metastable defect kinetics in CIGS materials," *Thin Solid Films*, vol. 517, no. 7, pp. 2277–2281, 2009.
- [49] T. Sakurai, H. Uehigashi, M. Islam, T. Miyazaki, S. Ishizuka, K. Sakurai, a. Yamada, K. Matsubara, S. Niki, and K. Akimoto, "Temperature dependence of photocapacitance spectrum of CIGS thin-film solar cell," *Thin Solid Films*, vol. 517, pp. 2403–2406, Feb. 2009.
- [50] P. T. Erslev, J. Lee, G. M. Hanket, W. N. Shafarman, and J. D. Cohen, "The electronic structure of CIGS alloyed with silver," *Thin Solid Films*, vol. 519, pp. 7296–7299, Aug. 2011.
- [51] J. Boucher, D. Miller, C. Warren, J. Cohen, B. McCandless, J. Heath, M. Lonergan, and S. Boettcher, "Optical response of deep defects as revealed by transient photocapacitance and photocurrent spectroscopy in cdte/cds solar cells," *Solar Energy Materials and Solar Cells*, vol. 129, pp. 57 – 63, 2014.
- [52] C. W. Warren, J. Li, C. A. Wolden, D. M. Meysing, T. M. Barnes, D. W. Miller, J. T. Heath, and M. C. Lonergan, "The effect of copper on the sub-bandgap density of states of CdTe solar cells," *Applied Physics Letters*, vol. 106, no. 20, p. 203903, 2015.
- [53] M. M. Islam, M. A. Halim, T. Sakurai, N. Sakai, T. Kato, H. Sugimoto, H. Tampo, H. Shibata, S. Niki, and K. Akimoto, "Determination of deep-level defects in $\text{Cu}_2\text{ZnSn}(\text{S}, \text{Se})_4$ thin-films using photocapacitance method," *Appl. Phys. Lett.*, vol. 106, no. 24, p. 243905, 2015.
- [54] H.-P. Wang, C. M. Sutter-Fella, P. Lobaccaro, M. Hettick, M. Zheng, D.-H. Lien, D. W. Miller, C. W. Warren, E. T. Roe, M. C. Lonergan, H. L. Guthrey, N. M. Haegel, J. W. Ager, C. Carraro, R. Maboudian, J.-H. He, and A. Javey, "Increased optoelectronic quality and uniformity of hydrogenated p-InP thin films," *Chemistry of Materials*, vol. 28, no. 13, pp. 4602–4607, 2016.

- [55] J. T. Heath, *Electronic transitions in the bandgap of copper indium gallium diselenide polycrystalline thin films*. PhD dissertation, University of Oregon, 2002.
- [56] A. F. Halverson, *The role of sulfur alloying in defects and transitions in copper indium gallium diselenide disulfide thin-films*. PhD dissertation, University of Oregon, 2007.
- [57] P. Erslev, *The electronic structure within the mobility gap of transparent amorphous oxide semiconductors*. PhD dissertation, University of Oregon, 2010.
- [58] P. G. Hugger, *Structural and Electronic Properties of Hydrogenated Nanocrystalline Silicon Employed in Thin Film Photovoltaics*. PhD dissertation, University of Oregon, 2011.
- [59] C. W. Warren, *The effect of copper on the defect structure of cadmium telluride thin-film solar cells*. PhD dissertation, University of Oregon, 2015.
- [60] J. W. Boucher, *Studies of GaAs Solar Cells Grown by Close-Spaced Vapor Transport*. PhD dissertation, University of Oregon, 2016.
- [61] M. A. Green, K. Emery, Y. Hishikawa, W. Warta, and E. D. Dunlop, “Solar cell efficiency tables (version 44),” *Progress in Photovoltaics*, vol. 22, pp. 701–710, 2014.
- [62] S. De Wolf, J. Holovsky, S. J. Moon, P. Löper, B. Niesen, M. Ledinsky, F. J. Haug, J. H. Yum, and C. Ballif, “Organometallic halide perovskites: Sharp optical absorption edge and its relation to photovoltaic performance,” *J. Phys. Chem. Lett.*, vol. 5, no. 6, pp. 1035–1039, 2014.
- [63] M. Samiee, S. Konduri, B. Ganapathy, R. Kottokkaran, H. A. Abbas, A. Kitahara, P. Joshi, L. Zhang, M. Noack, and V. Dalal, “Defect density and dielectric constant in perovskite solar cells,” *Appl. Phys. Lett.*, vol. 105, p. 153502, Oct. 2014.
- [64] A. Sadhanala, F. Deschler, T. H. Thomas, S. E. Dutton, K. C. Goedel, F. C. Hanusch, M. L. Lai, U. Steiner, T. Bein, P. Docampo, D. Cahen, and R. H. Friend, “Preparation of single-phase films of $\text{CH}_3\text{NH}_3\text{Pb}(\text{I}_{1-x}\text{Br}_x)_3$ with sharp optical band edges,” *The Journal of Physical Chemistry Letters*, vol. 5, no. 15, pp. 2501–2505, 2014.
- [65] H.-S. Duan, H. Zhou, Q. Chen, P. Sun, S. Luo, T.-B. Song, B. Bob, and Y. Yang, “The identification and characterization of defect states in hybrid organic inorganic perovskite photovoltaics,” *Phys. Chem. Chem. Phys.*, vol. 17, no. 1, pp. 112–116, 2015.

- [66] A. Baumann, S. V ath, P. Rieder, M. C. Heiber, K. Tvingstedt, and V. Dyakonov, "Identification of trap states in perovskite solar cells," *The Journal of Physical Chemistry Letters*, vol. 6, no. 12, pp. 2350–2354, 2015.
- [67] X. Wu, J. Zhou, A. Duda, Y. Yan, G. Teeter, S. Asher, W. K. Metzger, S. Demtsu, S.-h. Wei, and R. Noufi, "Phase control of Cu_xTe film and its effects on CdS / CdTe solar cell," *Thin Solid Films*, vol. 515, pp. 5798–5803, 2007.
- [68] T. Gessert, W. Metzger, P. Dippo, S. Asher, R. Dhere, and M. Young, "Dependence of carrier lifetime on Cu-contacting temperature and ZnTe:Cu thickness in CdS/CdTe thin film solar cells," *Thin Solid Films*, vol. 517, pp. 2370–2373, Feb. 2009.
- [69] E. L. Warren, A. E. Kibbler, R. M. France, A. G. Norman, P. Stradins, and W. E. McMahon, "Growth of antiphase-domain-free GaP on Si substrates by metalorganic chemical vapor deposition using an in situ AsH_3 surface preparation," *Applied Physics Letters*, vol. 107, no. 8, p. 082109, 2015.
- [70] H. J. Snaith, A. Abate, J. M. Ball, G. E. Eperon, T. Leijtens, N. K. Noel, S. D. Stranks, J. T.-W. Wang, K. Wojciechowski, and W. Zhang, "Anomalous hysteresis in perovskite solar cells," *The Journal of Physical Chemistry Letters*, vol. 5, no. 9, pp. 1511–1515, 2014.
- [71] M. M. Lee, J. Teuscher, T. Miyasaka, T. N. Murakami, and H. J. Snaith, "Efficient hybrid solar cells based on meso-superstructured organometal halide perovskites," *Science*, vol. 338, pp. 643–7, Nov. 2012.
- [72] A. Abate, T. Leijtens, S. Pathak, J. Teuscher, R. Avolio, M. E. Errico, J. Kirkpatrick, J. M. Ball, P. Docampo, I. McPherson, and H. J. Snaith, "Lithium salts as 'redox active' p-type dopants for organic semiconductors and their impact in solid-state dye-sensitized solar cells," *Phys. Chem. Chem. Phys.*, vol. 15, pp. 2572–2579, 2013.
- [73] G.-J. A. H. Wetzelaer, M. Scheepers, A. M. Sempere, C. Momblona, J.  vila, and H. J. Bolink, "Trap-assisted non-radiative recombination in organic-inorganic perovskite solar cells.," *Adv. Mater.*, vol. 27, pp. 1837–41, Mar. 2015.
- [74] J. Tauc, "Optical properties and electronic structure of amorphous Ge and Si," *Materials Research Bulletin*, vol. 3, no. 1, pp. 37 – 46, 1968.
- [75] A. V. Gelatos, J. D. Cohen, and J. P. Harbison, "Correlation of optical and thermal emission processes for bound-to-free transitions from mobility gap states in doped hydrogenated amorphous silicon," *AIP Conf. Proc.*, vol. 120, no. May 2013, pp. 16–23, 1984.

- [76] W.-J. Yin, T. Shi, and Y. Yan, “Unusual defect physics in $\text{CH}_3\text{NH}_3\text{PbI}_3$ perovskite solar cell absorber.,” *Appl. Phys. Lett.*, vol. 104, no. 6, pp. 0639031–0639034, 2014.
- [77] J. M. Azpiroz, E. Mosconi, J. Bisquert, and F. De Angelis, “Defect migration in methylammonium lead iodide and its role in perovskite solar cell operation,” *Energy Environ. Sci.*, vol. 8, no. 7, pp. 2118–2127, 2015.
- [78] M.-H. Du, “Density Functional Calculations of Native Defects in $\text{CH}_3\text{NH}_3\text{PbI}_3$: Effects of Spin-Orbit Coupling and Self-Interaction Error,” *J. Phys. Chem. Lett.*, vol. 6, no. 8, pp. 1461–1466, 2015.
- [79] S. D. Stranks, V. M. Burlakov, T. Leijtens, J. M. Ball, A. Goriely, and H. J. Snaith, “Recombination Kinetics in Organic-Inorganic Perovskites: Excitons, Free Charge, and Subgap States,” *Phys. Rev. Appl.*, vol. 2, p. 034007, Sep. 2014.
- [80] M. Saliba, T. Matsui, J.-Y. Seo, K. Domanski, J.-P. Correa-Baena, M. K. Nazeeruddin, S. M. Zakeeruddin, W. Tress, A. Abate, A. Hagfeldt, and M. Gratzel, “Cesium-containing triple cation perovskite solar cells: improved stability, reproducibility and high efficiency,” *Energy Environ. Sci.*, vol. 9, pp. 1989–1997, 2016.
- [81] G. E. Eperon, T. Leijtens, K. A. Bush, R. Prasanna, T. Green, J. T.-W. Wang, D. P. McMeekin, G. Volonakis, R. L. Milot, R. May, A. Palmstrom, D. J. Slotcavage, R. A. Belisle, J. B. Patel, E. S. Parrott, R. J. Sutton, W. Ma, F. Moghadam, B. Conings, A. Babayigit, H.-G. Boyen, S. Bent, F. Giustino, L. M. Herz, M. B. Johnston, M. D. McGehee, and H. J. Snaith, “Perovskite-perovskite tandem photovoltaics with optimized band gaps,” *Science*, vol. 354, no. 6314, pp. 861–865, 2016.
- [82] J. H. Noh, S. H. Im, J. H. Heo, T. N. Mandal, and S. I. Seok, “Chemical management for colorful, efficient, and stable inorganic-organic hybrid nanostructured solar cells,” *Nano Letters*, vol. 13, no. 4, pp. 1764–1769, 2013.
- [83] J. M. Ball and A. Petrozza, “Defects in perovskite-halides and their effects in solar cells,” *Nat. Energy*, vol. 1, p. 16149, Oct. 2016.
- [84] D. W. Miller, G. E. Eperon, E. T. Roe, C. W. Warren, H. J. Snaith, and M. C. Lonergan, “Defect states in perovskite solar cells associated with hysteresis and performance,” *Applied Physics Letters*, vol. 109, no. 15, p. 153902, 2016.
- [85] F. Urbach, “The long-wavelength edge of photographic sensitivity and of the electronic absorption of solids,” *Phys. Rev.*, vol. 92, p. 1324, Dec. 1953.

- [86] E. T. Hoke, D. J. Slotcavage, E. R. Dohner, A. R. Bowring, H. I. Karunadasa, and M. D. McGehee, “Reversible photo-induced trap formation in mixed-halide hybrid perovskites for photovoltaics,” *Chem. Sci.*, vol. 6, pp. 613–617, 2015.
- [87] Y. Li, J. K. Cooper, R. Buonsanti, C. Giannini, Y. Liu, F. M. Toma, and I. D. Sharp, “Fabrication of planar heterojunction perovskite solar cells by controlled low-pressure vapor annealing,” *The Journal of Physical Chemistry Letters*, vol. 6, no. 3, pp. 493–499, 2015.
- [88] C. M. Sutter-Fella, Y. Li, M. Amani, J. W. Ager, F. M. Toma, E. Yablonovitch, I. D. Sharp, and A. Javey, “High photoluminescence quantum yield in band gap tunable bromide containing mixed halide perovskites,” *Nano Letters*, vol. 16, no. 1, pp. 800–806, 2016.
- [89] Q. Chen, H. Zhou, Z. Hong, S. Luo, H.-S. Duan, H.-H. Wang, Y. Liu, G. Li, and Y. Yang, “Planar heterojunction perovskite solar cells via vapor-assisted solution process,” *Journal of the American Chemical Society*, vol. 136, no. 2, pp. 622–625, 2014.
- [90] C. M. Sutter-Fella, D. W. Miller, Q. P. Ngo, E. T. Roe, F. M. Toma, I. D. Sharp, M. C. Lonergan, and A. Javey, “Band tailing and deep defect states in $\text{CH}_3\text{NH}_3\text{Pb}(\text{I}_{1-x}\text{Br}_x)_3$ perovskites as revealed by sub-bandgap photocurrent,” *ACS Energy Letters*, vol. 2, no. 3, pp. 709–715, 2017.
- [91] C. G. Bischak, C. L. Hetherington, H. Wu, S. Aloni, D. F. Ogletree, D. T. Limmer, and N. S. Ginsberg, “Origin of reversible photoinduced phase separation in hybrid perovskites,” *Nano Letters*, vol. 17, no. 2, pp. 1028–1033, 2017.
- [92] W. van Roosbroeck and W. Shockley, “Photon-radiative recombination of electrons and holes in germanium,” *Phys. Rev.*, vol. 94, pp. 1558–1560, Jun. 1954.
- [93] J. D. Cohen, “Identifying the electronic properties relevant to improving the performance of high band-gap copper based I–III–VI₂ chalcopyrite thin film photovoltaic devices,” tech. rep., NREL, 2008.
- [94] A. D. Vos, “Detailed balance limit of the efficiency of tandem solar cells,” *Journal of Physics D: Applied Physics*, vol. 13, no. 5, p. 839, 1980.
- [95] C. D. Bailie, M. G. Christoforo, J. P. Mailoa, A. R. Bowring, E. L. Unger, W. H. Nguyen, J. Burschka, N. Pellet, J. Z. Lee, M. Gratzel, R. Noufi, T. Buonassisi, A. Salleo, and M. D. McGehee, “Semi-transparent perovskite solar cells for tandems with silicon and CIGS,” *Energy Environ. Sci.*, vol. 8, pp. 956–963, 2015.

- [96] L. F. Jiang, W. Z. Shen, and Q. X. Guo, “Temperature dependence of the optical properties of AlInN,” *Journal of Applied Physics*, vol. 106, no. 1, p. 013515, 2009.
- [97] S. Valdueza-Felip, E. Bellet-Amalric, A. Núñez-Cascajero, Y. Wang, M.-P. Chauvat, P. Ruterana, S. Pouget, K. Lorenz, E. Alves, and E. Monroy, “High In-content InGaN layers synthesized by plasma-assisted molecular-beam epitaxy: Growth conditions, strain relaxation, and In incorporation kinetics,” *Journal of Applied Physics*, vol. 116, no. 23, p. 233504, 2014.
- [98] K. Chen, R. Kapadia, A. Harker, S. Desai, J. Seuk Kang, S. Chuang, M. Tosun, C. M. Sutter-Fella, M. Tsang, Y. Zeng, D. Kiriya, J. Hazra, S. R. Madhupathy, M. Hettick, Y.-Z. Chen, J. Mastandrea, M. Amani, S. Cabrini, Y.-L. Chueh, J. W. Ager III, D. C. Chrzan, and A. Javey, “Direct growth of single-crystalline III-V semiconductors on amorphous substrates,” *Nat. Commun.*, vol. 7, p. 10502, Jan. 2016.
- [99] J. P. Conde, V. Chu, M. F. da Silva, A. Kling, Z. Dai, J. C. Soares, S. Arekat, A. Fedorov, M. N. Berberan-Santos, F. Giorgis, and C. F. Pirri, “Optoelectronic and structural properties of amorphous silicon-carbon alloys deposited by low-power electron-cyclotron resonance plasma-enhanced chemical-vapor deposition,” *Journal of Applied Physics*, vol. 85, no. 6, pp. 3327–3338, 1999.
- [100] U. B. Cappel, T. Daeneke, and U. Bach, “Oxygen-induced doping of Spiro-MeOTAD in solid-state dye-sensitized solar cells and its impact on device performance,” *Nano Letters*, vol. 12, no. 9, pp. 4925–4931, 2012.
- [101] W.-J. Yin, T. Shi, and Y. Yan, “Unique properties of halide perovskites as possible origins of the superior solar cell performance,” *Advanced Materials*, vol. 26, no. 27, pp. 4653–4658, 2014.
- [102] A. Buin, P. Pietsch, J. Xu, O. Voznyy, A. H. Ip, R. Comin, and E. H. Sargent, “Materials processing routes to trap-free halide perovskites,” *Nano Letters*, vol. 14, no. 11, pp. 6281–6286, 2014.
- [103] P. Schulz, E. Edri, S. Kirmayer, G. Hodes, D. Cahen, and A. Kahn, “Interface energetics in organo-metal halide perovskite-based photovoltaic cells,” *Energy Environ. Sci.*, vol. 7, pp. 1377–1381, 2014.
- [104] K. T. Butler, J. M. Frost, and A. Walsh, “Band alignment of the hybrid halide perovskites $\text{CH}_3\text{NH}_3\text{PbCl}_3$, $\text{CH}_3\text{NH}_3\text{PbBr}_3$ and $\text{CH}_3\text{NH}_3\text{PbI}_3$,” *Mater. Horiz.*, vol. 2, pp. 228–231, 2015.
- [105] S. D. Stranks, V. M. Burlakov, T. Leijtens, J. M. Ball, A. Goriely, and H. J. Snaith, “Recombination kinetics in organic-inorganic perovskites: Excitons, free charge, and subgap states,” *Phys. Rev. Applied*, vol. 2, p. 034007, Sep. 2014.

- [106] N. H. Tiep, Z. Ku, and H. J. Fan, “Recent advances in improving the stability of perovskite solar cells,” *Advanced Energy Materials*, vol. 6, no. 3, p. 1501420, 2016.
- [107] Q. Chen, H. Zhou, T.-B. Song, S. Luo, Z. Hong, H.-S. Duan, L. Dou, Y. Liu, and Y. Yang, “Controllable self-induced passivation of hybrid lead iodide perovskites toward high performance solar cells,” *Nano Letters*, vol. 14, no. 7, pp. 4158–4163, 2014.
- [108] F. Jiang, Y. Rong, H. Liu, T. Liu, L. Mao, W. Meng, F. Qin, Y. Jiang, B. Luo, S. Xiong, J. Tong, Y. Liu, Z. Li, H. Han, and Y. Zhou, “Synergistic effect of PbI_2 passivation and chlorine inclusion yielding high open-circuit voltage exceeding 1.15 v in both mesoscopic and inverted planar $\text{CH}_3\text{NH}_3\text{PbI}_3(\text{Cl})$ -based perovskite solar cells,” *Advanced Functional Materials*, vol. 26, no. 44, pp. 8119–8127, 2016.